

Modeling, Analysis, and Stabilization of a Single-Stage Utility-Scale Photovoltaic System  
with Reduced DC-Link Capacitance

by

Mohammad Adnan Kamal Magableh

A thesis submitted in partial fulfillment of the requirements for the degree of

Master of Science

in

Energy Systems

Department of Electrical and Computer Engineering  
University of Alberta

© Mohammad Adnan Kamal Magableh, 2020

## **Abstract**

A single-stage utility-scale photovoltaic (PV) system is usually interfaced with the host grid via a central voltage-source converter (VSC). Recently, due to their reliability, dc-link film capacitors are favored over electrolytic capacitors in grid-connected VSC applications. However, the capacitance per unit volume of film capacitors is significantly smaller than that of electrolytic capacitors. The overall system stability might be compromised by the reduction of the dc-link capacitance, particularly in PV systems, which have a dynamic resistance that varies with operating conditions. Using a detailed small-signal model of the grid-connected PV system, it is shown in this thesis that the reduction of the dc-link capacitance interferes with the dynamic resistance of the PV array leading to instabilities. The minimum dc-link capacitance that preserves the overall system stability is determined. To mitigate instabilities with a reduced dc-link capacitance, a simple yet effective active compensator is developed. Detailed time-domain simulations validate the analytical results and show the effectiveness of the proposed compensator in preserving the system stability.

## Preface

This thesis is an original work by Mohammad Adnan Kamal Magableh. As detailed in the following, the research work described in some chapters of this thesis has been submitted for publication as a scholarly article in which Prof. Yasser Abdel-Rady I. Mohamed and Dr. Amr Ahmad A. Radwan are the supervisory authors and have contributed to concepts formation and the manuscript composition.

Materials in Chapters 3 and 4 of this thesis have been submitted as Mohammad Adnan K. Magableh, Amr Ahmed A. Radwan, and Yasser A.-R. I. Mohamed, "Assessment and Mitigation of Dynamic Instabilities in a Single-Stage Grid-Connected Photovoltaic System with Reduced DC-Link Capacitance," submitted to *IEEE Transaction on Sustainable Energy*, Feb 2020.

## **Acknowledgments**

First and foremost, I would like to praise and thank Allah, the Almighty, for enlightening my path, guiding me, and giving me knowledge, patience, and strength to do my research.

I would like to express my sincere appreciation and deep gratitude to my supervisor, Prof. Yasser Mohamed, for his supervision and continuous guidance throughout my M.Sc. studies. It has been an honor and privilege to work under his supervision.

Also, I would like to extend a special thanks to my co-supervisor, Dr. Amr Radwan, for his motivation, and continuous encouragement. I appreciate all his contributions of time and invaluable discussions during my M.Sc. program. His support and guidance will never be forgotten.

I would like to express my thanks to the examiners, Dr. Venkata Dinavahi, Dr. Hao Liang, and Dr. Yasser Mohamed, for their valued time and interest in my thesis.

My sincere thanks go to all the members of my family, especially my loving parents Dr. Kamal Magableh and Intisar Aloqaily, to whom I owe all the success in my life. There are no words that can express my sincere gratitude, but I pray that God will bless them and reward them. Also, I would like to express my sincere gratitude to the love, prayers, and endless support from my sisters and brothers.

I gratefully acknowledge Jordan University of Science and Technology, Jordan, for the scholarship and the financial support provided for this research.

Last but not least, I would like to thank all my friends, colleagues, and professors for their endless support. Also, I am truly thankful to all the faculty and staff members in the Department of Electrical and Computer Engineering at the University of Alberta for supporting me and providing a pleasant working atmosphere during the past two years.

# Table of Contents

Abstract.....	ii
Preface.....	iii
Acknowledgments.....	iv
Table of Contents.....	v
List of Tables.....	viii
List of Figures.....	ix
List of Acronyms.....	xi
List of Symbols.....	xiii
Chapter 1 Introduction.....	1
1.1 Problem Statement and Research Motivations.....	2
1.2 Thesis Objectives.....	2
1.3 Thesis Methodology.....	3
1.4 Thesis Contributions.....	3
1.5 Thesis Outline.....	4
Chapter 2 Background and Literature Survey.....	5
2.1 Introduction.....	5
2.2 Power Electronic Converters in Grid-Connected PV Systems.....	5
2.3 PV Systems as a DC Power Source for Grid-Connected Converters.....	6
2.4 DC-Link Capacitors.....	8
2.5 Interaction Dynamics and Instabilities in Grid-Connected PV Systems.....	10
2.5.1 AC-Side Interactions.....	10
2.5.2 DC-Side Interactions.....	11
2.6 Eigenvalues- and Impedance-Based Stability Analysis.....	12
2.6.1 Nyquist Impedance Ratio Criterion.....	13
2.6.2 Participation Factor Analysis.....	14
Chapter 3 Modeling and Control of the Grid-Connected Voltage-Source Converter-Based Photovoltaic System.....	15
3.1 Introduction.....	15

3.2 Power Circuit Model of the Grid-Connected PV System .....	15
3.2.1 AC-Side Circuit Model.....	16
3.2.2 DC-Side Circuit Model.....	18
3.2.3 AC Power Circuit Dynamic Model in the Grid-Reference Frame .....	21
3.2.4 DC Power Circuit Dynamic Model .....	22
3.3 Conventional Vector Control of the Grid-Connected Voltage-Source Converter-Based Photovoltaic System.....	24
3.3.1 PLL Dynamics .....	25
3.3.2 Inner Current Control .....	27
3.3.3 DC-Link Voltage Control.....	28
3.3.4 PCC Utility-Grid Voltage Control.....	31
3.4 Small-Signal Modeling and Analysis.....	32
3.5 Evaluation Results.....	33
3.5.1 Large-Signal Non-Linear Models.....	33
3.5.2 Small-Signal Model Validation .....	35
3.5.3 Approximated and Accurate Models of the DC-Link Voltage Controller .....	37
3.5.4 Dominant Eigenvalues.....	39
3.6 Conclusion.....	40
Chapter 4 Assessment and Mitigation of Dynamic Interactions in Grid-Connected PV-VSC Systems .....	41
4.1 Introduction .....	41
4.2 Instabilities Due to PV and DC-link Interactions .....	41
4.3 Active Stabilization of Grid-Connected VSC-PV System.....	44
4.3.1 Proposed Active Compensator .....	44
4.3.2 Sensitivity Analysis .....	46
4.4 Evaluation Results.....	47
4.4.1 Influence of Reduced DC-Link Capacitance.....	47
4.4.2 Active Compensated Interaction .....	49
4.4.3 Influence of the DC-Link Cable .....	50
4.4.4 Operation Under Fault Conditions .....	51
4.4.5 Uncertainties in DC-Link Capacitance.....	53

4.4.6 Sensitivity Results .....	54
4.5 Conclusion.....	55
Chapter 5 Conclusions and Future Work.....	56
5.1 Conclusions .....	56
5.2 Future Work .....	57
Bibliography .....	58
APPENDICES .....	63
Appendix A.3 .....	63
Appendix A.4 .....	70

## List of Tables

Table 3.1: Participation Factor Analysis of the Damped and Lightly-Damped Systems. ....	39
Table 4.1: Participation-Factor analysis of the uncompensated system under unstable operating conditions. ....	43
Table A.3.1: Solar module parameters. ....	63

## List of Figures

Figure 2.1: Configuration of PV generators. (a) Centralized structure. (b) String structure. (c) Multi-string structure. (d) AC module structure. ....	8
Figure 2.2: Impedance representation of integrated voltage source-load system. ....	13
Figure 3.1: Vector-controlled three-phase single-stage grid-connected PV inverter. ....	15
Figure 3.2: Transformer equivalent circuit. (a) Exact model. (b) Equivalent circuit referred to the primary side. (c) Equivalent circuit referred to the secondary side. ....	17
Figure 3.3: The equivalent circuit of the grid-impedance and transformer referred to the secondary side. ....	18
Figure 3.4: Cells, modules, and strings of the single-diode PV array. ....	20
Figure 3.5: Equivalent circuit representation of the PV generator. a) PV module. b) PV string. c) PV array. ....	21
Figure 3.6: PV array at different solar irradiance levels. (a) $P_{pv} - V_{pv}$ and $I_{pv} - V_{pv}$ characteristics. (b) Dynamic and static PV impedances. ....	24
Figure 3.7: Vector control of the grid-connected VSC. ....	25
Figure 3.8: Bode plot of the open-loop PLL controller. ....	27
Figure 3.9: Bode plot of the open-loop current controller. ....	28
Figure 3.10: Bode plot of the open-loop accurate dc-link voltage controller. ....	30
Figure 3.11: Bode plot of the open-loop approximated dc-link voltage controller. ....	31
Figure 3.12: Bode plot of the open-loop PCC voltage controller. ....	32
Figure 3.13: The dc-link voltage of the large-signal model. ....	34
Figure 3.14: d-axis current of the large-signal model. ....	34
Figure 3.15: d-axis PCC voltage of the large-signal model. ....	35
Figure 3.16: DC-link voltage response of the verified small-signal model at two different conditions. ....	36
Figure 3.17: D-axis current response of the verified small-signal model at two different conditions. ....	36
Figure 3.18: D-axis PCC-voltage response of the verified small-signal model at two different conditions. ....	37

Figure 3.19: DC-Link voltage response of the approximated model at lightly-damped condition. ....	38
Figure 3.20: DC-Link voltage response of the accurate model at lightly-damped condition. ....	38
Figure 4.1: Eigenvalue analysis of the influence of the dc-link capacitance on the uncompensated system.....	42
Figure 4.2: Impedance analysis of the influence of the dc-link capacitance on the uncompensated system.....	43
Figure 4.3: Vector control schematic of the grid-connected VSC with compensated control loop. ....	44
Figure 4.4: Eigenvalue analysis of the influence of the dc-link capacitance on the compensated system. ....	45
Figure 4.5: Impedance analysis of the influence of the dc-link capacitance on the compensated system. ....	46
Figure 4.6: Transfer function of the closed-loop dc-link voltage controller at $c_{dc} = 1 p. u.$ for both compensated and uncompensated systems. ....	47
Figure 4.7: Uncompensated system response at different voltage levels and dc-link capacitance values. ....	48
Figure 4.8: Influence of added active compensation loop at $t = 1.3s.$ under CCR operation. ....	49
Figure 4.9: Uncompensated system response at different voltage levels and dc-link capacitance values. ....	50
Figure 4.10: Compensated and uncompensated dc-link voltage responses at $C_{dc} = 1 p. u.$ due to dc cable influence. ....	51
Figure 4.11: Compensated and uncompensated dc-link voltage response to a single-phase ground fault at $t=1.5s$ for 5 cycles. ....	52
Figure 4.12: Compensated dc-link voltage response to a single-phase ground fault at $t=4.5s$ for 5 cycles.....	53
Figure 4.13: Uncompensated system for $\pm 20\%$ dc-link capacitance values due to aging. ...	54
Figure 4.14: Compensated and uncompensated dc-link voltage responses at $C_{dc} = 1 p. u.$ ..	55

## List of Acronyms

1PG	Single-Phase-to-Ground
3PG	Three-Phase-to-Ground
AC	Alternating Current
AE-Cs	Aluminium Electrolytic Capacitors
BW	Bandwidth
CCR	Constant Current Region
CSC	Current Source Converter
CVR	Constant Voltage Region
DC	Direct-Current
DGs	Distributed Generations
d-	Direct-
d-q	Direct-Quadrature
ESR	Equivalent Series Resistance
HPF	High-Pass Filter
HVDC	High-Voltage Direct Current
IGBT	Insulated-Gate Bipolar Transistor
LC	Inductive-Capacitive
LCL	Inductive-Capacitive-Inductive
LHP	Left-Half-Plane
LPF	Low-Pass-Filter
LVRT	Low-Voltage Ride Through
MIMO	Multi-Input-Multi-Output
MLC-Cs	Multilayer Ceramic Capacitors
MPP	Maximum Power Point
MPPF-Cs	Metallized Polypropylene Film Capacitors
MPPT	Maximum Power Point Tracking
p.u.	Per-Unit
PCC	Point-of-common-coupling
PF	Power Factor

PI	Proportional-and-Integral
PLL	Phase-locked-loop
PTFE-Cs	Polytetrafluoroethylene Capacitors
PV	Photovoltaic
PWM	Pulse-Width-Modulation
q-	Quadrature-
RER	Renewable Energy Resources
RHP	Right-Half-Plane
RLC	Resistive-Inductive-Capacitive
RRF	Rotating Reference-Frame
SRF	Synchronous Reference-Frame
SSSA	Small Signal Stability Analysis
VSC	Voltage-Source Converter

## List of Symbols

### A. Superscripts

$*$	Reference value of the variable
$^{\circ}$	Steady-state value
$g$	Variable component in grid-frame
$c$	Variable component in converter-frame

### B. Subscripts

$d$	Variable component in d-axis
$q$	Variable component in q-axis

### C. Variables and Parameters

$i_g, v_g$	Grid current and voltage
$i_c, v_c$	Capacitor current and voltage
$I_{ext}, P_{ext}$	External current and power
$v_{pcc}$	Voltage at the point of common coupling
$I_{dc}$	Converter input current
$v, i$	VSC output voltage and current
$V_{pv}, I_{pv}, P_{pv}$	Photovoltaic output voltage, current, and Power
$\omega^{\circ}$	Grid angular frequency
$s$	Laplace operator
$\Delta$	Small-signal perturbation
$R_g, L_g$	Grid resistance and inductance
$R_{Tr}, L_{Tr}$	Equivalent resistance and inductance of the step-up transformer referred to the secondary side
$N$	Step-up transformer primary to secondary turns ratio
$f_{sw}$	Converter switching frequency
$r_{on}$	VSC diodes state-on resistance
$R_f, L_f, C_f$	Resistance, inductance, and capacitance of the ac filter
$V_{dc}, C_{dc}$	DC-Link voltage and capacitance

$R_{dc}, L_{dc}$	Resistance and inductance of the dc cable
$r_d, r_s$	Photovoltaic dynamic and static resistance
$P_{dc}, P_{inv}$	VSC input and output power
$P_{pcc}, Q_{pcc}$	Injected active and reactive power to the ac grid
$PM_{pll}, \omega_{pll}, K_p^{pll}, K_i^{pll}$	Phase margin, cut-off frequency, proportional and integral gains of the PLL controller
$PM_i, \omega_i, K_p^i, K_i^i$	Phase margin, cut-off frequency, proportional and integral gains of the current controller
$PM_{vac}, \omega_{vac}, K_p^{vac}, K_i^{vac}$	Phase margin, cut-off frequency, proportional and integral gains of the ac voltage controller
$PM_{vdc}, \omega_{vdc}, K_p^{vdc}, K_i^{vdc}$	Phase margin, cut-off frequency, proportional and integral gains of the dc-link voltage controller

# Chapter 1

## Introduction

Driven by global climate change concerns and the continuous growth of energy demand, renewable energy resources are becoming increasingly popular all over the world. According to the International Energy Agency (IEA), the world's total installed photovoltaic capacity reached 486 GW out of 2351 GW of the global total renewable energy capacity at the end of 2018. By 2050, PV global cumulative capacity would contribute 11% of the worldwide electricity generation to avoid 2.3 gigatons of carbon dioxide emissions per year [1], [2].

In the grid-connected PV systems, the generated electrical power quality is degraded due to the intermittent nature of PV energy. Therefore, centralized voltage-source converters (VSCs) with dc-link capacitors are usually used to regulate the generated PV power and interface PV power plants to the host grid [3], [4]. Generally, three types of dc-link capacitors are available for power converters; namely, they are multi-layer ceramic capacitors (MLC-Cs), metalized polypropylene film capacitors (MPPF-Cs), and aluminum electrolytic capacitors (AE-Cs) [5]. Even though MPPF capacitors are the best choice for reliability, their utilization is still challenging due to the high cost and the limited capacitance per unit volume. Generally, a relatively large dc-link capacitance enhances the dc-link voltage profile and increases the stability margin. However, more research work has been conducted to preserve the dc-link stability under reduced capacitance to pave the way to adopt MPPF capacitors [2], [6], [7].

A single-stage VSC is used to interface a PV array to the utility grid. The VSC adopts the standard vector control strategy with cascaded outer and inner control loops [8]. However, it is reported in the literature that, with a reduced dc-link capacitance, the VSC dynamics could involve right-half plane (RHP) poles in many applications, such as motor drives, wind turbines, and PV systems [9]–[11].

The impact of the dynamic impedance of PV arrays on a grid-connected VSC with a reduced dc-link capacitance has been briefly and solely addressed in single specified research work in the literature [11]. However, the developed single-stage model in [11] is not comprehensive and only comprises three states. The dynamic model in [11] does not consider the influence of the step-

up transformer, dc-cables, the grid-stiffness, the phase-locked loop (PLL), and ac-voltage control dynamics. Moreover, the studied research work mainly focuses on the two-stage without considering single stage converters. More importantly, there is no proposed solution or mitigation technique to enhance the integration of PV generators with reduced dc-link capacitance.

## **1.1 Problem Statement and Research Motivations**

It is shown in this thesis that the integration of PV-VSC systems with reduced dc-link capacitance induces significant instabilities under certain conditions. The motivation of this work is to preserve the system stability under these challenging conditions to allow a wide adoption of the new dc-link capacitance technology, e.g., film capacitors. The following areas are the research motivation for this work:

- 1) The integration of PV-VSCs using reduced dc-link capacitors induces instabilities under certain conditions.
- 2) The operation of the PV arrays with the constant voltage and current regions has a significant impact on the system dynamics, particularly with the reduced dc-link capacitance.
- 3) The control of interfacing VSCs should be designed accurately in order to clearly show and study the interaction dynamics due to integrated devices interference.

## **1.2 Thesis Objectives**

The aim of this work is to mitigate the adverse impacts of utilizing a reduced dc-link capacitance in the grid-connected PV-VSCs systems. This thesis addresses the grid-connected PV-VSCs systems according to the following objectives:

- 1) Accurate design of the cascaded controllers of the grid-connected VSC in PV applications considering parameter uncertainties.
- 2) Determination of the minimum dc-link capacitance analytically to preserve the dynamic stability.
- 3) Assessment of the dynamic interactions of the grid-connected PV-VSCs systems with the reduced dc-link capacitance.

- 4) Mitigation of the adverse impacts or dynamic instabilities following the integration of PV-VSCs systems using a reduced dc-link capacitance.
- 5) Verification of the analytical results using nonlinear time-domain simulations within MATLAB/SIMULINK® environment.

### **1.3 Thesis Methodology**

Throughout this work, the following key tools and methods are utilized to address the problem under study:

- 1) Developing a dynamic small-signal model of the PV-VSC grid-connected system to investigate the system stability using eigenvalues and impedance analysis.
- 2) Using linear control tools and frequency-domain analysis to derive accurate formulas to determine the appropriate parameters of the PLL controller, current controller, PCC voltage controller, and DC-link voltage controller.
- 3) Conducting stability analysis based on the Nyquist admittance ratio criterion around the point of interconnections between PV generators and grid-connected VSC system.
- 4) Preserve the stability of the system by designing a linear compensator from the source-side to damp the system actively.
- 5) Linear analysis tools such as root-locus, participation factor, and Bode plots are utilized in the dynamic studies.

### **1.4 Thesis Contributions**

The contributions of this thesis to the research field are as follows:

- 1) Newly original equations are derived to design the controllers of the grid-connected VSC. This includes the PLL, current controller, ac-voltage controller, and accurate and approximated dc-link voltage controller. The method provided in this work helps to design the proportional and integral gains that preserve the system stability margins.
- 2) The development of a comprehensive and detailed small-signal and impedance models for the grid-connected PV-VSC system. This model is utilized to conduct dynamic analysis and assess the performance under different conditions.

- 3) Investigation of the dynamic instabilities due to the interference between the reduced dc-link capacitance and PV dynamic impedance at different operating points.
- 4) The development of a new compensator to enhance the integration of the single-stage PV systems with minimized dc-link capacitance. With the new compensation method, the system dynamic performance is robustly damped, and film capacitors with reduced capacitance per unit volume can be used to increase the system reliability. The operation is investigated under different operating conditions, including fault conditions.

## 1.5 Thesis Outline

The remainder of the thesis is organized as follows.

*Chapter 2* presents the background and literature survey for the grid-connected PV-VSC systems, including the recent challenges in PV integration.

*Chapter 3* presents comprehensive modeling and control of the grid-connected VSCs. An accurate design approach for the system controllers is analytically derived and presented. Also, the dynamic and static impedances of the PV generator are investigated. Moreover, a detailed small-signal model in the d-q reference-frame is developed to study the system stability. Furthermore, non-linear time-domain simulations are conducted and presented to validate the developed linearized model.

*Chapter 4* presents the dynamic interference between the PV dynamic impedance and dc-link capacitance under different operating regions. A new active compensation method is proposed to mitigate the associated dynamic instabilities. Small-signal and time-domain simulation models are developed to study the dynamic stability interactions and investigate the performance of the compensated system under different operating conditions. Furthermore, this chapter investigates the large-signal low-voltage ride-through (LVRT) performance for both the compensated and uncompensated systems.

*Chapter 5* presents the thesis conclusions and suggestions for future research work in this area.

# Chapter 2

## Background and Literature Survey

### 2.1 Introduction

Voltage-source converters (VSCs) have been increasingly used in various applications in modern power systems to integrate renewable energy resources (RER). The dynamic interactions on both ac- and dc-sides of VSCs interfacing RER and the system stability have become important topics in current research.

In this chapter, a background and a literature survey of the main topics in this thesis are introduced. It is shown that power electronic converters are the primary building element for different applications in the power system, especially when they are used to interface renewable energy sources, such as PV generators, into the utility-grid. Different topologies of PV systems are presented based on their applications and structures. Various classes of dc-link capacitor technologies and the corresponding critical challenges are also presented and compared. It is shown that interaction dynamics among VSC converter and other devices may adversely influence the overall system stability even if each stage is inherently functional and stable. Both eigenvalue- and impedance-based stability analysis for a VSC-based PV system are presented under the d-q transformation modeling approach.

### 2.2 Power Electronic Converters in Grid-Connected PV Systems

Renewable energy resources, PV systems, should be interfaced by power electronic converters to perform two main tasks; regulating the operating point of the PV generator to achieve the maximum power point tracking (MPPT) and inject the regulated generated power to the utility grid at the desired power factor (PF) [3], [12]. Two types of grid-connected PV systems are introduced in the literature based on the number and nature of power electronic converters used in the system [3], [4], [13]. The two systems are (a) Single-stage or centralized PV systems, which include one dc/ac converter to achieve the maximum power point (MPP) tracking and control the injected ac current into the utility grid. (b) Two-stage system which includes a PV-interfacing dc/dc converter to achieve the MPP tracking, and a grid-interfacing dc/ac converter to control the injected ac current into the ac-side.

In grid integration systems, two types of converters are widely adopted as an interfacing stage in many applications such as PV systems, wind farms, motor drives, and HVDC systems [14]–[16]. (1) Voltage-source converter (VSC), which operates as a buck inverter. The dc-side element of the VSC is a capacitor, and the controlled dc input is the dc-link voltage, whereas the dc input current depends on the system conditions. Also, the output voltage of the VSCs is independent of loading conditions, and the power loss in the dc-link capacitor is around 0.5%. (2) Current-source converter (CSC), which operates as a boost inverter. The dc-side element of the CSC is a choke, and the controlled dc input is the dc current while input voltage changes with load. Also, the output current of the CSCs is independent of load, and the power loss in the dc choke is usually 2% to 4%.

VSCs are more common and widely used in grid-interfacing systems due to the absence of a series reactor, which reduces the losses comparing to the high losses in CSCs. However, CSCs have advantages over VSCs in the PV systems with small power capacity where VSCs require another stage to boost the voltage, which increases the cost and complexity of the system [15]. For the previous reasons, the structure of the single-stage system using VSCs has gained a high significance in the utility-scale systems by reducing the power losses and cost. As a result, the single-stage system is considered in this thesis.

### **2.3 PV Systems as a DC Power Source for Grid-Connected Converters**

PV systems have gained a high growth rate among other renewable resources in the world today. By the end of 2018, the total installed capacity of the PV systems reached 486 GW out of 2351 GW of the total capacity of renewable resources [1], [2]. The capacity of renewable sources is expected to expand by 50% between 2019 and 2024 to add 1200 GW to the total installed power today, where PV systems participate in 60% among other renewable resources [17]. By 2050, PV cumulative capacity would contribute 11% of the global electricity generation.

PV generators are nonlinear devices that are used to convert sunlight into electricity. The basic device of the PV generator is the PV cell that typically produces an electrical power between 1 and 2 W [4]. Multiple PV cells are connected in series to form a PV module. To increase the terminal voltage of the PV generator, multiple PV modules are connected in series to form a PV

string. To increase the power rating of the PV generator, many PV strings are connected in parallel to form a PV array [18].

PV systems can be classified based on their generation capacities as follows [19], [20]. (1) Utility-scale three-phase (3PG) systems with generation capacity from 1-10 MW. This system requires many interconnection transformers and several dc/ac converters connected in parallel. (2) Medium-scale system for commercial applications (such as government sites, residential complexes, etc.) with ranges from 10-1000 kW. The interconnection configuration of this system depends on the system capacity. (3) Small scale single-phase (1PG) systems for residential and roof-top applications with capacities ranging up to 10 kW. The installation of this system is single-phase and can produce the required power at the customer's load without using interconnection transformers to reduce the system complexity. (4) Off-grid system, which is isolated from the utility-grid, is required for remote communities and telecommunication units with different ratings. It is important to investigate the integration of the utility-scale PV systems due to their large power generation capacity and their potential impacts on the system stability.

Regarding the interconnection of the PV structure and the used converters, PV generators are normally categorized into four types as shown in Figure 2.1 [3], [12], [13]. (1) The centralized structure which consists of a combination of parallel-connected PV strings interfaced by one centralized dc/ac converter. This structure is commonly used because of its low cost and high conversion efficiency. (2) The string structure where each PV string is interfaced to the utility-grid by its own dc/ac converter. This structure has better efficiency than the centralized structure because MPP tracking can be separately achieved in each string. However, the cost is higher due to the additional number of interfacing converters. (3) The multi-string where each string is interfaced by a dc/dc converter to boost the dc-link voltage and a common dc/ac converter is then used to interface all PV strings to the ac-side. (4) The ac module structure, which consists of multiple PV modules, and each module is interfaced by its own dc/ac converter. The reliability of this structure is very high because there is no single point of failure.

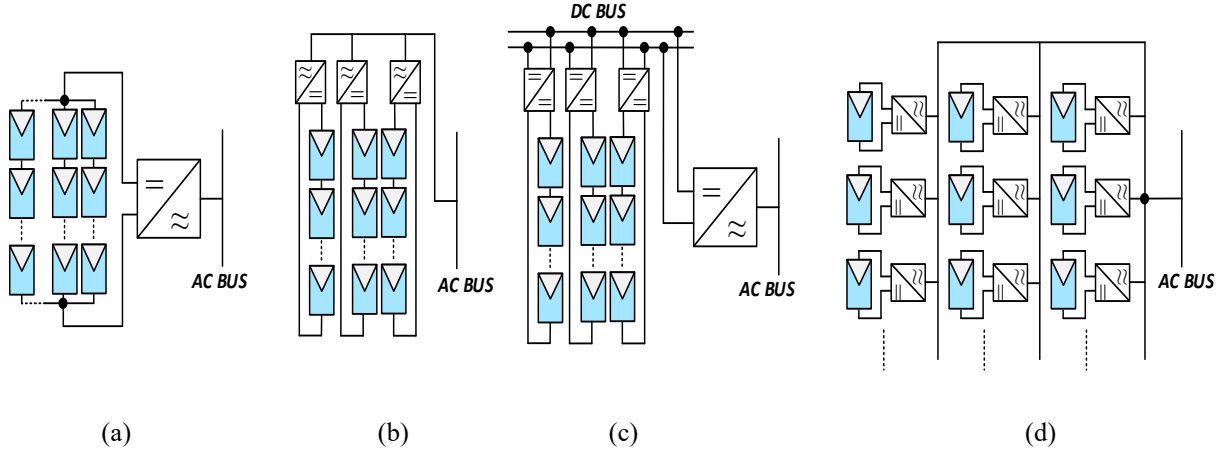


Figure 2.1: Configuration of PV generators. (a) Centralized structure. (b) String structure. (c) Multi-string structure. (d) AC module structure.

## 2.4 DC-Link Capacitors

A capacitor ( $C$ ) is a passive electronic component that stores electrical energy in the form of an electrostatic field as shown in (2.1a). It consists of two conducting plates separated by an insulating material called a dielectric, which limits the leakage current. The capacitance is directly proportional to the surface areas ( $A$ ) of the plates, and is inversely proportional to the separation ( $d$ ) between the plates. The capacitance also depends on the relative permittivity constant ( $\epsilon_r = \epsilon/\epsilon_o$ ) of the dielectric as shown in (2.1b).

$$C = \frac{Q}{V} \quad (2.1a)$$

$$C = \epsilon \frac{A}{d} \quad (2.1b)$$

where  $Q$  is the charge held by the conductor in Coulomb, and  $V$  is the electric potential in Volt.

Capacitors are categorized into several types based on the used materials and the fabrication process [5], [21]–[23]. (1) Electrolytic capacitors are commonly made of aluminum and tantalum. This type of capacitors is polarized and made from a high-surface-area metallic tube contacting with an electrolyte. They provide the largest capacitance among all high-voltage capacitors and have a wide tolerance so that they are used to filter the rectified current and the noise suppression in power supplies. (2) Ceramic capacitors are made of metal electrodes separated by ferroelectric dielectrics. This type of capacitors has a wide range of capacitance. A new type of

ceramic capacitors, multilayer ceramic capacitors (MLC-Cs), has been developed to extend the use of the ceramic capacitors in high capacitance applications. (3) Polymer film capacitors which have a polymer dielectric and are classified into four types based on the properties of their dielectric substance: Polycarbonate capacitors which have a good stability over time and a wide temperature range, polypropylene capacitors which have a stable capacitance with time and applied voltage, polystyrene capacitors which have a good insulation and low cost, and polytetrafluoroethylene capacitors (PTFE-Cs) which have a low loss and a wide temperature range. Sometimes two polymer dielectrics are merged to meet a specific application requirement. (4) Mica capacitors are classified into two types: clamped mica capacitors, which are considered obsolete due to their inferior characteristics, and silver mica capacitors where silver electrodes are plated on to mica dielectric substance. This type is not widely used because it is large in volume, but it is importantly used in high-frequency applications where a high accuracy and high-quality factor (i.e., low loss and great temperature stability) are needed. (5) Supercapacitors which consist of high surface area electrodes that are filled with electrolyte. They have an extremely high capacitance on the scale of hundreds of farads for a single capacitor. As a result, they received much attention to be the most common type of capacitors used in applications as an alternative power source because of their high-power density and long cycling stability.

DC-link capacitors are one type of reliability-critical important components in power electronic converters applications which contribute to cost, size, and failure rate on a considerable scale [5], [24]. Moreover, dc-link capacitance decreases, and equivalent series resistance (ESR) increases with aging, which leads to an increase in voltage ripple and damages the semiconductor switches due to overvoltage. Therefore, a large number of scientific researches on the different methods for condition monitoring of dc-link capacitors have been conducted in the last decades to monitor the health of capacitors, estimate their lifetimes, and enhance the reliability of the overall system in different applications, such as solar, wind turbines, electrical aircraft, and electric vehicles [25]–[29].

Aluminum Electrolytic Capacitors (AE-Cs), Metallized Polypropylene Film Capacitors (MPPF-Cs), and high capacitance Multi-Layer Ceramic Capacitors (MLC-Cs) are generally the most three types of capacitors available for dc-link applications [5]. The dc-link design requires the matching of available capacitor characteristics and parameters to the specific application needs under various conditions. The three types have advantages and shortcomings in their performance

and could be compared from different aspects. AE-Cs achieve the highest energy density, highest capacitance, lowest cost, and low ripple current ratings, however, with aging (evaporation of electrolyte) low capacity and high ESRs. MLC-Cs have a smaller size, wider frequency range, and higher operating temperatures up to 200°C. However, they suffer from higher cost and mechanical sensitivity. MPPF-Cs provide a well-balanced performance for high voltage applications in terms of cost and ESR, capacitance, ripple current, and reliability. Nevertheless, they have the shortcomings of large volume and moderate upper operating temperature.

DC-link capacitors are widely used in voltage-source converter applications to mainly balance the power difference, minimize the voltage ripple, and short-term energy storage. Aluminum electrolytic capacitors for such applications is assumed to be one of the lifetime bottlenecks and weakest links in power electronic systems. Various studies propose passive and active capacitive dc-link solutions to reduce the dc-link capacitance in different applications; therefore, bulky electrolytic capacitors can be replaced by reliable small film capacitors which have a well-balanced performance among all other types of the dc-link capacitors to improve the reliability of the overall system [30]–[34].

## **2.5 Interaction Dynamics and Instabilities in Grid-Connected PV Systems**

In the literature, several works addressing the stability analysis of grid-connected PV systems have been conducted to enhance the dynamic system performance. Some performance issues regarding the dynamic interactions between the converter and the PV system on the dc-side and between the utility-grid and the converter on the ac-side have been discussed. Different passive and active damping techniques are presented on both sides to mitigate the instabilities by damping the dynamic system performance.

### **2.5.1 AC-Side Interactions**

Dynamic interactions of the ac-side of VSC integrated into ac grid have been studied in the literature. The dynamic instability of VSC represented by the high current and voltage distortions caused by the interactions between converters and the passive components has been observed in the proposed systems in [35], [36]. In [37], [38], a sensitivity analysis has been conducted to investigate the influence of the system parameters on the dynamics performance of the three-phase grid-connected single-stage VSC-based PV system with a high order inductive-capacitive-

inductive (LCL) filter. A similar system is investigated in [39] where a proposed two degree of freedom active damping technique is presented to mitigate the ac LCL filter resonance. Moreover, the resonance frequency of the LCL filter and the negative impact of the grid impedance on the dynamics of VSC controllers are investigated under weak grid scenarios in [37], [40]–[43]. Further, it has been shown in [44] that a large dc-link power injection of VSC with insufficient reactive power compensation can cause power instability in the ac-side of VSC grid-connected system. Furthermore, the impacts of control loops coupling on the dynamic stability of grid-connected VSCs is revealed in [45].

The ac-side stability is considered for the grid-connected CSC-based PV systems in the literature. Active damping techniques for the ac filter resonance have been addressed for the CSC in some applications [46]–[48]. The control of a current-source converter (CSC) in the synchronous rotating reference frame is discussed in [46]. An active compensation technique is proposed to mitigate the undesirable resonant oscillations induced by the ac capacitor of the CSC with the utility-grid inductance. A similar active damping control method for the LC resonance in the CSC operating in low switching frequency is proposed in [47], where an active compensation feedback signal is fed from the ac capacitor voltage through a high-pass filter (HPF). In [48], multiple active damping methods for the ac-side LC filter resonance in CSCs are investigated where it is found that the derivative inductor current and the proportional capacitor voltage feedbacks can significantly damp the resonance by appropriately designing their gains.

### **2.5.2 DC-Side Interactions**

The dc-side operating conditions of the PV grid-connected system should be considered in the dynamic system stability analysis to firmly preserve the system's performance. The optimal placement for solar energy plants and the influence of the variable atmospheric conditions, especially solar irradiance and temperature on the dynamic performance of the utility-grid has been studied in [49], [50]. The negative impact of the non-linearity of the generated PV power and high penetration effect of PV generators on the dynamic performance of the grid-utility VSC- and CSC-based systems have been mitigated by canceling the inherent nonlinearities and decoupling the dynamic interaction of the dc and ac sides in [51] and [52], respectively. In [52], the dynamic performance of both CSC- and VSC-based PV systems is compared where CSC-based systems present better over-current protection performance than VSC-based systems due to the regulation

of the input dc current in CSC-based systems. A nonlinear dc-link voltage controller for the grid-connected VSC-based PV system is designed in [50], where the system nonlinearities are algebraically transferred by applying the state feedback linearization technique into autonomous nonlinear zero-dynamic stable system and reduced-order linear system controlled by a linear controller. The proposed technique is tested under variable solar irradiation levels. However, the complexity of implementing a nonlinear controller is not justified when the conventional proportional-and-integral (PI) controller can be implemented to improve the system performance.

Several research works have been conducted to minimize the dc-link capacitance value in the field of motor drive and wind turbine applications in order to replace the low-reliability electrolytic capacitors by the small capacitance high-reliability film capacitors [9], [10]. It has been shown in these systems that right-half-plane (RHP) poles appear in their control dynamics when the dc-link capacitance is minimized. However, the influence of the dynamic impedance of PV generators on a grid-connected single- and two-stage VSC-based PV systems with minimized dc-link capacitance has been solely addressed in [11]. It is shown in this study that the dynamic system is stable when the PV generator operates at constant voltage region (CVR) and maximum power point, whereas an RHP pole appears in the control dynamics of the PV systems when the PV generator operates at constant current region (CCR) which affect the system stability. This RHP pole is correlated to the bandwidth (BW) of the dc voltage controller, the dc-link capacitance, and the operating point of the PV generator (CCR, CVR, and MPP). As a result, an accurate selection of the dc-link capacitance and dc-side operating conditions are mandatory to preserve the system stability.

## **2.6 Eigenvalues- and Impedance-Based Stability Analysis**

This section introduces a background of the analytical methods used to study the challenging interaction dynamic problems and stability issues in this thesis. The eigenvalues and impedance analysis of the small-signal model of grid-connected VSC-based PV system in the d-q reference frame, including root-locus, Bode and Nyquist impedance ratio criterion, are addressed in [53]–[55]. A brief overview of existing approaches for defining a state variable participation factor in mode to analyze power system stability is provided in [56].

### 2.6.1 Nyquist Impedance Ratio Criterion

The grid-connected VSC-based PV system is highly nonlinear, a small-signal state-space model is developed, and then the required impedances can be obtained as a transfer functions that depend on the control and physical parameters of the associated system as shown throughout this thesis. The ratio between the source output impedance and the load input impedance around an interconnection point must satisfy the Nyquist stability criterion to ensure the overall system stability. At the interconnection point, the equivalent impedance representation of a voltage source is represented by a Thevenin equivalent circuit with a voltage source ( $V_s(s)$ ) and a source output impedance ( $Z_s(s)$ ) while the equivalent input impedance representation of the integrated load is defined as ( $Z_l(s)$ ). As a result, the equivalent circuit of the overall system is represented as shown in Figure 2.2.

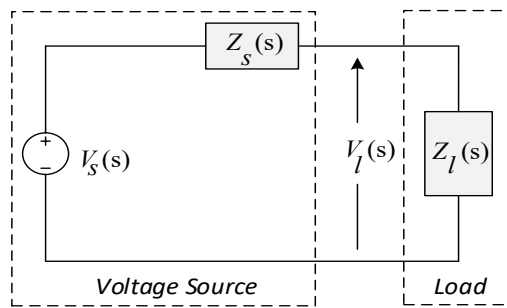


Figure 2.2: Impedance representation of integrated voltage source-load system.

The voltage response at the interconnection point could be given as in (2.2) where  $(1 + Z_s(s)/Z_l(s))^{-1}$  represents a closed-loop system with a unity forward gain and negative feedback of the ratio  $(Z_s(s)/Z_l(s))$ . It is clearly shown that the stability of the integrated systems is maintained if the ratio  $(Z_s(s)/Z_l(s))$  satisfies the Nyquist stability criterion. In other words,  $Z_s(s)$  should be less than  $Z_l(s)$  in the whole frequency domain range.

$$V_l(s) = \left(1 + \frac{Z_s(s)}{Z_l(s)}\right)^{-1} V_s(s) \quad (2.2)$$

A similar analysis has been applied to the current source integrated with a load system in [54]. It has been concluded that the stability requirements for VSC is opposite to that for CSC, where voltage source impedance is required to be low, and the source impedance of a current source is ideally infinity.

The unstable systems can be re-stabilized by reshaping the source- or load-side impedance to avoid undesirable dynamic interactions on the whole frequency domain range. The reshaping can be achieved by using passive elements or active compensators to modify the load- or source-side characteristics and satisfy load/source Nyquist stability criterion [57].

### 2.6.2 Participation Factor Analysis

Due to the complex and unpredictable nature of modern distribution power systems that consist of hundreds of generators connected with thousands of power lines, hundreds of load centers, and complex physical process problems due to parameter uncertainty, it is so difficult to simulate and analyze the stability of such power systems [56]. Selective Modal Analysis (SMA), which consists of eigenvalues and participation factors, is the most modern method recently used to study power system stability [58].

Participation factor ( $P_j^k$ ), as well-known today, is used to identify the relationships among the state variables and eigenmodes by measuring the participation of the state variables ( $k$ ) in the eigenmodes ( $j$ ), and vice versa [56]. Participation factor is developed to calculate the state variables participation in the system eigenmodes for the first time in [58], as given in (2.3), and is defined by the left-right eigenvectors multiplication. The concept of participation factor is then divided into two different definitions (state-in-mode and mode-in-states) [59]. In [59], the authors show that formula (2.3) is inappropriate and invalid for systems with real eigenvalue cases. As a result, a new formula for calculating state variables participation in the system eigenmodes is proposed for accurate calculations of real eigenvalues cases as given in (2.4). However, incorrectness and inaccuracy of formula (2.4) for complex eigenvalues cases have been proved in [56] where a new validated approach to state-in-mode participation factor for both real and complex eigenvalues cases is proposed and defined as given in (2.5).

$$P_j^k = L_j^k R_j^k \quad (2.3)$$

$$P_j^k = \frac{[Re(L_j^k)]^2}{Re(L_j) * (Re(L_j))^T} \quad (2.4)$$

$$P_j^k = \frac{|L_j^k|^2}{\sum_k (|L_j^k|^2)} \quad (2.5)$$

## Chapter 3

# Modeling and Control of the Grid-Connected Voltage-Source Converter-Based Photovoltaic System

### 3.1 Introduction

This chapter investigates the interconnection of VSCs to a utility-grid using the conventional vector control in the rotating reference frame (RRF). A comprehensive analysis of the modeling and control of grid-connected VSC converter is presented considering all control loops. The PV dynamic impedance is identified under different PV operation regions. A large-signal model is built to validate the analytical results of the developed small-signal model.

### 3.2 Power Circuit Model of the Grid-Connected PV System

Centralized voltage-source converters shown in Figure 3.1 are usually used to interface large PV power plants to the host grid [4]. In the following sections, the dynamic model of the ac- and dc-sides are provided.

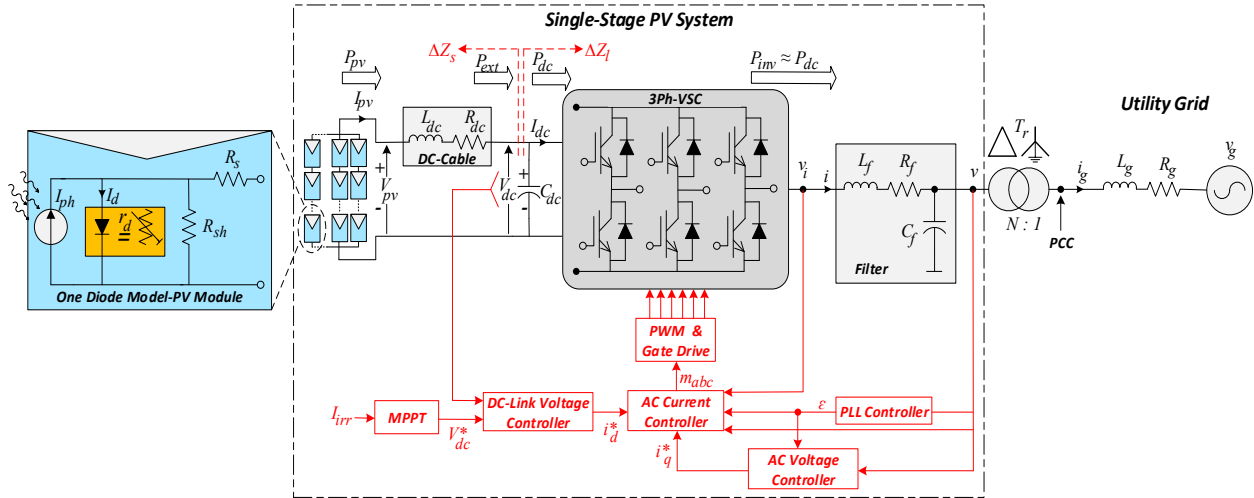


Figure 3.1: Vector-controlled three-phase single-stage grid-connected PV inverter.

As shown in Figure 3.1, the grid-connected PV array is interfaced by a three-phase two-level VSC consisting of six cells; each comprises an insulated-gate-bipolar transistor (IGBT) in parallel with a freewheeling diode. The transfer of energy from the PV generator to the utility-grid is achieved by the VSC. The dc-side of the VSC is interfaced by a capacitor to maintain the dc-

link voltage regulated. A filter is directly connected to the VSC terminals to filter out the switching harmonics in the ac current and voltage.

Vector control loops of the grid-connected PV-VSC system are briefly presented in Figure 3.1. MPPT is used to extract maximum power from PV generators. The phase-locked-loop is used to synchronize the VSC to the grid and generate the signals in the d-q converter frame. The outer dc-link and ac voltage control loops are used to generate the reference currents to be used by the inner current control loop. The VSC controllers are discussed in detail in Section 3.3.

### 3.2.1 AC-Side Circuit Model

The ac-side of grid-connected VSC is shown in Figure 3.1; the grid is modeled as a voltage source and an impedance. The grid impedance is defined by the short-circuit-ratio ( $SCR$ ) and the reactance to resistance ratio ( $X/R$ ). The low-pass filter (LPF) is used to attenuate the current and voltage harmonic components at the ac-side of the VSC. The step-up transformer is generally included in the grid-connected PV systems to match the terminal ac voltage of the LC-filter with the nominal grid voltage at the point of common coupling (PCC).

The dynamic equations of the LC-filter and the grid impedance integrated with the transformer are investigated in the following subsections in the phasor-domain.

#### a) Utility-Grid Interface

As shown in Figure 3.1, the grid is modeled as a voltage source and impedance to represent the grid stiffness. The grid-impedance comprises a large inductive part ( $L_g$ ) in series with the equivalent resistance of the line ( $R_g$ ) represented by the short-circuit-ratio ( $SCR = (VA)_{rated}/(VA)_{sc}$ ) and the reactance to resistance ratio ( $X/R$ ). The values of  $L_g$  and  $R_g$  are obtained according to (3.1) and (3.2).

$$L_g = \frac{v_g^2}{\omega^g (VA)_{sc}} \quad (3.1)$$

$$R_g = \frac{\omega^g L_g}{X/R} \quad (3.2)$$

The dynamic equation of the grid-impedance is:

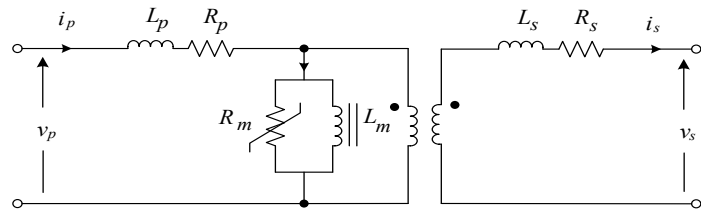
$$L_g \frac{di_g}{dt} + R_g i_g = v_s - v_g \quad (3.3)$$

where  $(VA)_{sc}$  and  $(VA)_{rated}$  are the short-circuit and rated capacity of the utility-grid in VA,

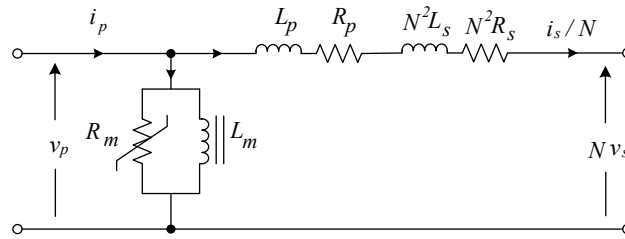
respectively;  $v_g$  and  $i_g$  are the grid voltage and current, respectively;  $v_s$  is the transformer secondary voltage, whereas  $\omega^g$  is the angular frequency of the utility-grid in rad/s.

### b) Step-Up Transformer

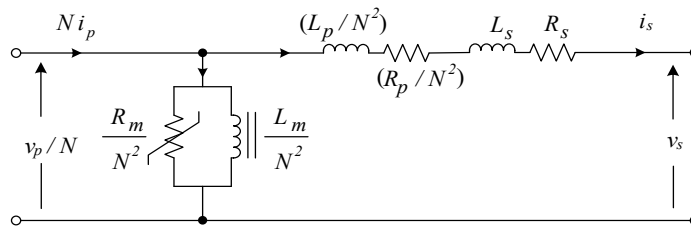
As shown in Figure 3.1, the step-up transformer is used to match the terminal ac voltage of the ac-filter with the nominal grid voltage at the point of common coupling. Figure 3.2a represents the equivalent circuit of the exact model of the step-up transformer. The transformer can be referred to the primary-side as in Figure 3.2b to integrate its dynamic with the ac-filter, or it can be referred to the secondary-side as in Figure 3.2c to integrate its dynamic with the utility-grid impedance which is the applied case in this research study as shown in Figure 3.3.



(a)



(b)



(c)

Figure 3.2: Transformer equivalent circuit. (a) Exact model. (b) Equivalent circuit referred to the primary side. (c)

Equivalent circuit referred to the secondary side.

$L_p$  and  $L_s$  are the primary and secondary inductances, respectively;  $R_p$  and  $R_s$  are the primary and secondary resistances, respectively.  $L_{TR} = \left(L_s + \frac{L_p}{N^2}\right)$  and  $R_{TR} = \left(R_s + \frac{R_p}{N^2}\right)$  are the equivalent inductance and resistance referred to the secondary-side, respectively;  $i_p$  and  $i_s$  are the primary and secondary currents; and  $v_p$  is the transformer primary voltage.

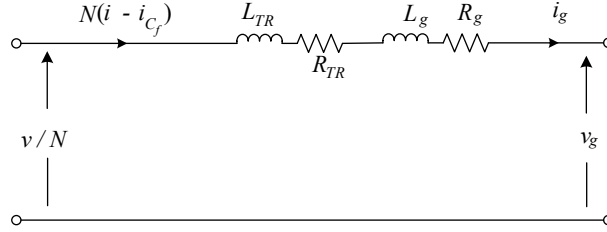


Figure 3.3: The equivalent circuit of the grid-impedance and transformer referred to the secondary side.

The dynamic equation of the transformer circuit integrated with the grid-impedance becomes:

$$L_T \frac{di_g}{dt} + R_T i_g = \frac{1}{N} v - v_g \quad (3.4)$$

where  $L_T = L_{TR} + L_g$  and  $R_T = R_{TR} + R_g$  are the total impedance of the step-up transformer and the utility-grid.

### c) AC-Filter

The three-phase low-pass filter is essential for the connection of the VSC to the utility-grid and is used to attenuate the current and voltage harmonic components at the ac-side of the VSC and is commonly selected as LC type for its simplicity and economy [4]. The dynamic equations of the filter inductance and capacitance are as follows:

$$L_f \frac{di}{dt} + R_f i = v_i - v \quad (3.5)$$

$$C_f \frac{dv}{dt} = i - \frac{1}{N} i_g \quad (3.6)$$

where  $v_i$  and  $i$  are the voltage and current of the ac terminal of VSC; and  $R_f$ ,  $L_f$ , and  $C_f$  are the resistance, inductance and capacitance of the ac-filter, respectively.

## 3.2.2 DC-Side Circuit Model

The dc-side of the grid-connected VSC-based PV system is shown in Figure 3.1. The dc-cable is

used to connect the PV farms to the grid-connected VSC system, whereas the PV plant is the main dc-source in the system, which generates the delivered power to the utility grid.

**a) DC-Link Capacitor**

Capacitors are widely used for dc links in the applications of the power electronic converters to balance the instantaneous power difference between the input source and output load [5]. The dc-link capacitance ( $C_{dc}$ ) is functioned as a filter to regulate the dc-link voltage ( $V_{dc}$ ) to the desired value in order to minimize voltage variation in the dc link and achieve the maximum generated power from the PV plant. The dynamic equation of the dc-link capacitor is given as follows:

$$\frac{d}{dt} \left( \frac{1}{2} C_{dc} V_{dc}^2 \right) = P_{ext} - P_{dc} \quad (3.7)$$

where  $P_{ext}$  is the incoming PV power;  $P_{dc}$  is the approximated injected power ( $P_{inv}$ ) to the ac-side assuming a lossless power converter;  $C_{dc}$  is the dc-link capacitor and its nominal value is designed at 5000  $\mu\text{F}$  [4].

**b) DC Transmission Cables**

The dc cables are used to transmit the generated PV power to the grid-connected VSC system. the dynamic model of the dc lines is modeled as follows:

$$L_{dc} \frac{dI_{pv}}{dt} + R_{dc} I_{pv} = V_{pv} - V_{dc} \quad (3.8)$$

where  $R_{dc}$  and  $L_{dc}$  are the resistance and inductance of the dc-cable, respectively; and their values are designed at [60].

**c) PV Generator**

The main building block of PV panels is the PV cell. Figure 3.4 shows the single-diode circuit representation of a PV generator in which multiple series-connected PV cells, denoted by the number  $n_s$ , are stacked together to form a PV module. To increase the terminal voltage ( $V_{pv}$ ) of the PV generators, several PV modules, denoted by the number  $N_s$ , are connected in series to form the PV string. To increase the power rating ( $P_{pv}$ ) of the PV generator, many PV strings, denoted by the number  $N_p$ , are connected in parallel to form a PV array [18]. At the level of one PV cell, the solar illumination ( $I_{irr}$ ) excites the electronics to typically generate 1.0 – 2.0 W of electrical

power [4]. The PV generated current ( $I_{ph}$ ) is dependent on the solar illumination level ( $I_{irr}$ ), and the PV temperature level ( $T$ ) as follows:

$$I_{ph} = (I_{irr}/I_{irr}^*)[I_{sc} + \alpha_i(T - T^*)] \quad (3.9)$$

where  $I_{irr}^*$  is the reference illumination level in  $W/m^2$ ;  $T^*$  is the reference temperature in Kelvin;  $I_{sc}$  is the short-circuit current of the PV cell in A; and  $\alpha_i$  is the temperature coefficient in A/Kelvin.

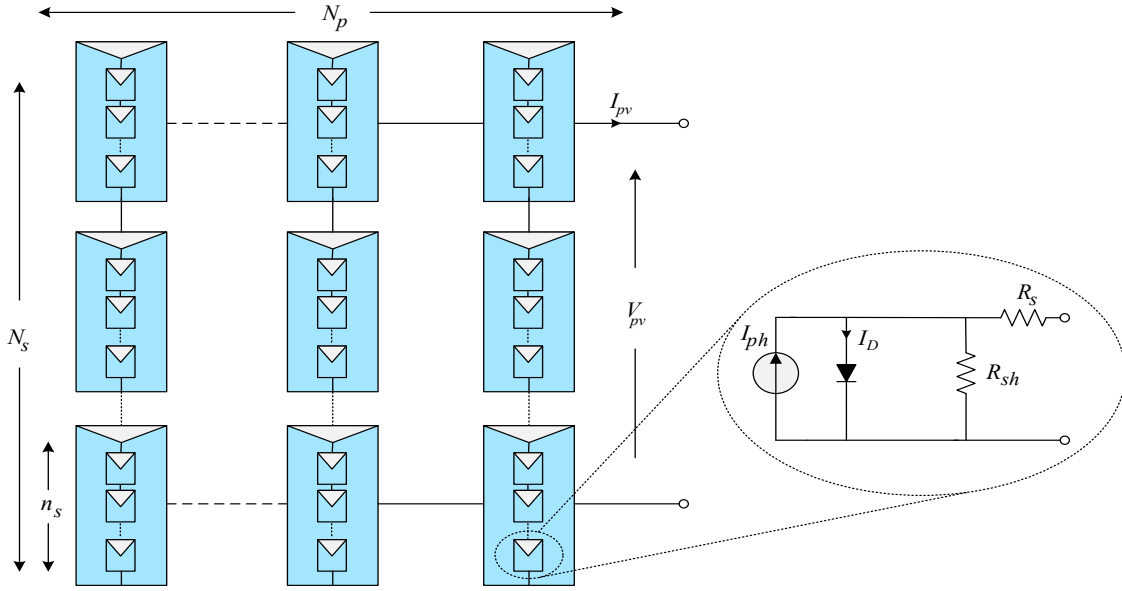


Figure 3.4: Cells, modules, and strings of the single-diode PV array.

As shown in Figure 3.5, the relation between the diode current ( $I_D$ ) and voltage ( $V_D$ ) is governed by the non-linear Shockley diode model where  $V_D$  is not directly measured and is represented in terms of  $V_{pv}$  and  $I_{pv}$  as follows:

$$V_D = V_{pv} + (N_s/N_p)R_s I_{pv} \quad (3.10)$$

$$I_{rs} = I_{rs}^* \left(\frac{T}{T^*}\right)^3 \exp\left\{\frac{q \cdot E_g}{A \cdot K} \left(\frac{1}{T^*} - \frac{1}{T}\right)\right\} \quad (3.11)$$

$$I_D = I_{rs} \left(\exp\left\{\frac{q \cdot V_D}{N_s \cdot n_s \cdot A \cdot k \cdot T}\right\} - 1\right) \quad (3.12)$$

where  $R_s$  is the equivalent series resistance of the PV module;  $I_{rs}$  and  $I_{rs}^*$  are the reverse saturation current at the operating and reference temperatures in A, respectively;  $q$  is the unit charge in Coulomb,  $K$  is the Boltzmann's constant in Joules/Kelvin;  $A$  is the ideality factor, and  $E_g$  is the band-gap energy of the PV cell which's 1.1eV for the silicon material.

As shown in Figure 3.5, the parasitic equivalent series resistance of the PV module ( $R_s$ ) is

considered in the PV model to represent the power losses, while the equivalent shunt resistance ( $R_{sh}$ ) is considered to represent the effect of the leakage current due to the fabrication process. The terminal equivalent PV current ( $I_{pv}$ ) can be represented as in (3.13), and the generated power of the PV system ( $P_{pv} = V_{pv}I_{pv}$ ) is controlled by the MPPT algorithms to deliver the maximum power to the utility-grid [4].

$$I_{pv} = N_p I_{ph} - N_p I_D - \frac{V_{pv} + (N_s/N_p)R_s I_{pv}}{(N_s/N_p)R_{sh}} \quad (3.13)$$

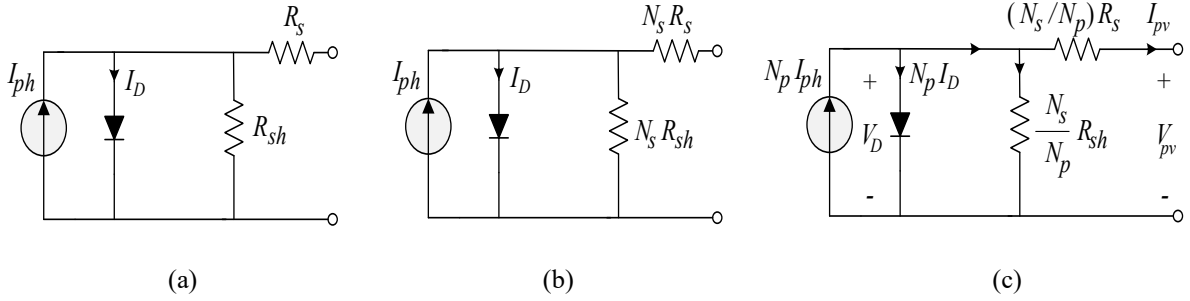


Figure 3.5: Equivalent circuit representation of the PV generator. a) PV module. b) PV string. c) PV array.

In this thesis, an array of the model “Mitsubishi Electric PV-UD190MF5” has been considered [61]. The nominal voltage and power for PV generator are designed at 1186 V and 1.5 MW, respectively. This matches the rating conditions of the recent centralized power electronic converters in PV applications [62].

### 3.2.3 AC Power Circuit Dynamic Model in the Grid-Reference Frame

As shown in section 3.3, the power circuit model of the grid-connected VSC should be represented in the  $(DQ)$ -grid rotating reference frame, denoted by the superscript “ $g$ ”, that rotating by the grid angular frequency ( $\omega^g$ ) to accurately study the dynamic stability of the system. The equations are represented in the grid-frame as follows:

$$L_f \frac{di_{dq}^g}{dt} + j\omega^g L_f i_{dq}^g + (R_f + r_{on})i_{dq}^g = v_{idq}^g - v_{dq}^g \quad (3.14)$$

$$L_T \frac{di_{gdq}^g}{dt} + j\omega^g L_T i_{gdq}^g + R_T i_{gdq}^g = \frac{1}{N} v_{dq}^g - v_{gdq}^g \quad (3.15)$$

$$C_f \frac{dv_{dq}^g}{dt} + j\omega^g C_f v_{dq}^g = i_{dq}^g - \frac{1}{N} i_{gdq}^g \quad (3.16)$$

### 3.2.4 DC Power Circuit Dynamic Model

The dynamic equations of the dc-link capacitance, dc-lines, and the PV generator model are investigated in the following subsections.

#### a) DC-Link Dynamic

The injected real power ( $P_{dc} \approx P_{inv}$ ) to the ac-side in (3.7) could be implemented as in (3.17) or it could be implemented as in (3.18) to be represented in terms of the PCC-real power control input ( $P_{pcc}$ ) and the dropped power in the ac-filter ( $P_{R_f}$ ) and ( $P_{L_f}$ ) as follows:

$$P_{inv} = Re \left\{ \frac{3}{2} \vec{v}_l(t) \vec{i}^*(t) \right\} = 1.5(v_{id}^g i_d^g + v_{iq}^g i_q^g) \quad (3.17)$$

$$P_{inv} = P_{R_f} + P_{L_f} + P_{pcc} \quad (3.18a)$$

$$P_{R_f} = Re \left\{ \frac{3}{2} R_f \vec{i}(t) \vec{i}^*(t) \right\} = \frac{3}{2} R_f \left( (i_d^g)^2 + (i_q^g)^2 \right) \quad (3.18b)$$

$$P_{L_f} = Re \left\{ \frac{3}{2} L_f \frac{d\vec{i}(t)}{dt} \vec{i}^*(t) \right\} = \frac{3}{2} L_f \left( i_d^g \frac{di_d^g}{dt} + i_q^g \frac{di_q^g}{dt} \right) \quad (3.18c)$$

$$P_{pcc} = Re \left\{ \frac{3}{2} \vec{v}_l(t) \vec{i}^*(t) \right\} = 1.5(v_d^g i_d^g + v_q^g i_q^g) \quad (3.18d)$$

The dynamic equation of the dc-link capacitor for the accurate system could be given as in (3.19a) or (3.19b), whereas the dynamic equation of the accurate system is given in (3.19c).

$$\frac{1}{2} C_{dc} \frac{d}{dt} V_{dc}^2 = V_{dc} I_{pv} - 1.5(v_{id}^g i_d^g + v_{iq}^g i_q^g) \quad (3.19a)$$

$$\frac{1}{2} C_{dc} \frac{d}{dt} V_{dc}^2 = V_{dc} I_{pv} - P_{R_f} - P_{L_f} - 1.5(v_d^g i_d^g + v_q^g i_q^g) \quad (3.19b)$$

$$\frac{1}{2} C_{dc} \frac{d}{dt} V_{dc}^2 = V_{dc} I_{pv} - 1.5(v_d^g i_d^g + v_q^g i_q^g) \quad (3.19c)$$

#### b) Dynamic Resistance of PV Array

As shown in Figure 3.6a, the characteristic of the PV array mainly reflects the non-linear characteristics of the p-n junction diode. Figure 3.6b shows the dc and ac PV impedances, where the dc resistance is the PV static resistance ( $r_s$ ) defined as ( $V_{pv}/I_{pv}$ ) and the ac resistance of the PV generator ( $r_d$ ) is the dynamic small-signal-resistance defined as the negative reciprocal of ( $dI_{pv}/dV_{pv}$ ) [63] and is given as follows:

$$r_d = -\left(\frac{dI_{pv}}{dV_{pv}}\right)^{-1} = \frac{1 + \frac{R_s}{R_{sh}} + \frac{I_{rs} \cdot q \cdot R_s}{n_s \cdot A \cdot k \cdot T^*} \exp\left(\frac{q \cdot \left(V_{pv} + \left(\frac{N_s}{N_p} R_s\right) I_{pv}\right)}{N_s \cdot n_s \cdot A \cdot k \cdot T^*}\right)}{\frac{1}{\left(\frac{N_s}{N_p} R_{sh}\right)} + \frac{N_p \cdot I_{rs} \cdot q}{N_s \cdot n_s \cdot A \cdot k \cdot T^*} \exp\left(\frac{q \cdot \left(V_{pv} + \left(\frac{N_s}{N_p} R_s\right) I_{pv}\right)}{N_s \cdot n_s \cdot A \cdot k \cdot T^*}\right)} \quad (3.20)$$

where the dynamic resistance at the MPP equals the static resistance at the same point as follows:

$$r_d|_{MPP} = -\left(\frac{dI_{pv}}{dV_{pv}}\right)^{-1} \Bigg|_{(V_{pv}^{max}, I_{pv}^{max})} = \left(\frac{V_{pv}}{I_{pv}}\right) \Bigg|_{(V_{pv}^{max}, I_{pv}^{max})} \quad (3.21)$$

The dynamic resistance of the PV generator can be defined in a deferent way as follows:

$$r_d = \left(r_d^D \parallel \frac{N_s}{N_p} R_{sh}\right) + \frac{N_s}{N_p} R_s \quad (3.22)$$

where  $r_d^D$  is the dynamic resistance of the p-n junction diode and is given as follows:

$$r_d^D = -\frac{N_s \cdot n_s \cdot A \cdot k \cdot T^*}{N_p I_{rs} q} \exp\left(\frac{-q \cdot \left(V_{pv} + \left(\frac{N_s}{N_p} R_s\right) I_{pv}\right)}{N_s \cdot n_s \cdot A \cdot k \cdot T^*}\right) \quad (3.23)$$

Due to the high nonlinearity of the PV characteristics and the continuous perturbation in the operating points with time, PV generator should be implemented in terms of its dynamic resistance to accurately study the dynamic performance at different certain operating conditions.

The dynamic model of the dc lines and PV generator are modeled as follows:

$$L_{dc} \frac{dI_{pv}}{dt} + R_{dc} I_{pv} = r_d I_{pv} - V_{dc} \quad (3.24)$$

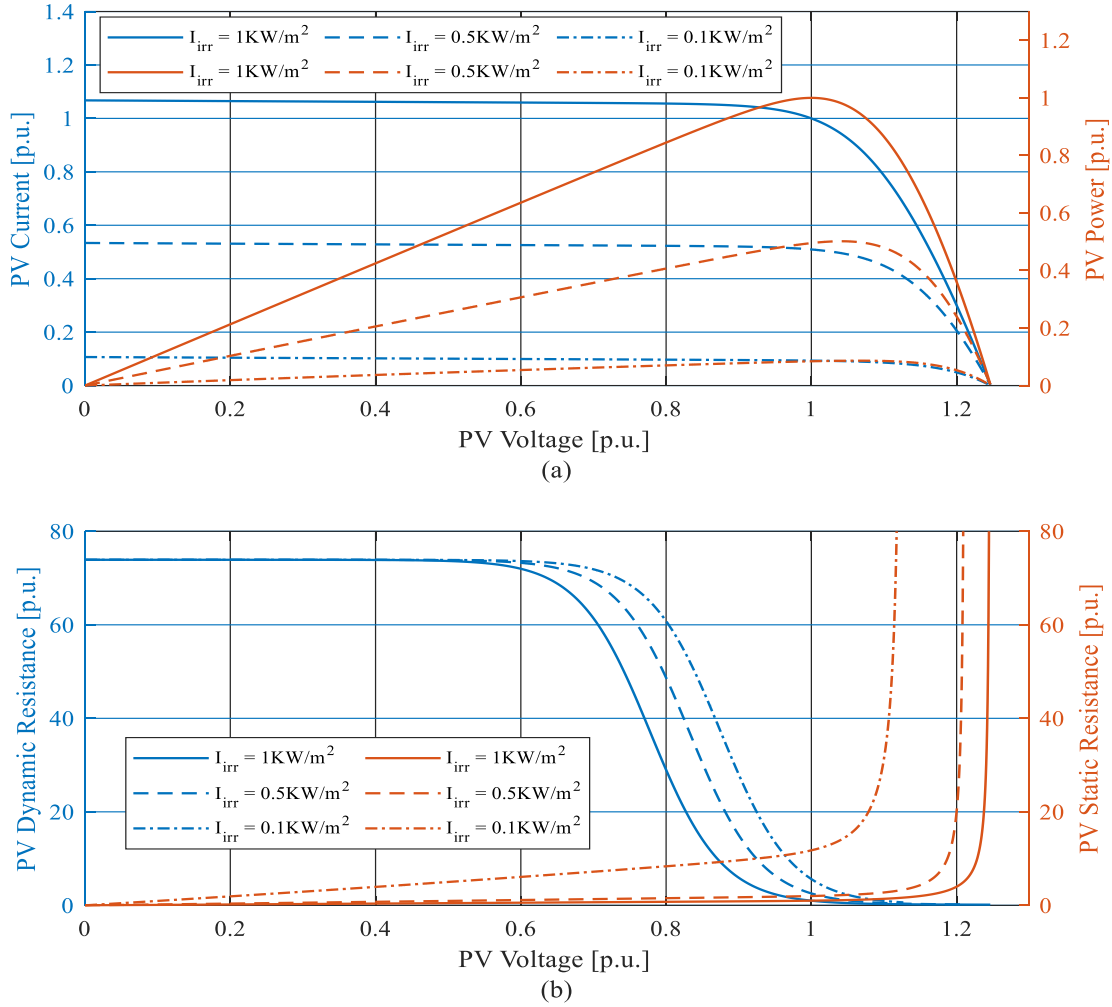


Figure 3.6: PV array at different solar irradiance levels. (a)  $P_{pv} - V_{pv}$  and  $I_{pv} - V_{pv}$  characteristics. (b) Dynamic and static PV impedances.

### 3.3 Conventional Vector Control of the Grid-Connected Voltage-Source Converter-Based Photovoltaic System

Figure 3.7 shows the control structure of the VSC in the synchronous rotating d-q reference frame. The phase-locked-loop generates the synchronization angle, which is used to transform signals between the grid-frame and the converter-frame. The squared value of the measured dc-link voltage ( $V_{dc}^2$ ) is compared to the reference value ( $V_{dc}^{*2}$ ) to process the error by a PI dc voltage controller ( $G_{vdc}(s)$ ), which determines the  $d$ -axis component of the reference value of the injected



$$\frac{d\varepsilon}{dt} = \omega \quad (3.26)$$

Referring to Figure 3.7, the measured quantities should be transformed and retransformed between the converter-frame and the grid-frame to accurately model the influence of the PLL on the system dynamics [64]. The frame transformation is mathematically modeled as  $f_{dq}^c = e^{-j\varepsilon} f_{dq}^g$  where the PCC voltage and the VSC output current and voltage are given as follows:

$$v_{dq}^c = [\cos(\varepsilon) - j \sin(\varepsilon)] v_{dq}^g \quad (3.27a)$$

$$i_{dq}^c = [\cos(\varepsilon) - j \sin(\varepsilon)] i_{dq}^g \quad (3.27b)$$

$$v_{idq}^g = [\cos(\varepsilon) + j \sin(\varepsilon)] v_{idq}^c \quad (3.27c)$$

Using (3.25) and (3.26), the open-loop transfer function of the PLL dynamics is  $\ell_{pll}(s) = \hat{V}_{pcc}(1/v_d^o)(G_\varepsilon/s)$ , where  $\hat{V}_{pcc} = v_d^o = v_{p-p}^{rms} \sqrt{2/3}$  is the peak value of the PCC voltage. The phase angle of  $\ell_{pll}(j\omega)$  at low and high frequencies is  $-180^\circ$  and  $-90^\circ$ , respectively. By selecting a proper phase margin ( $PM_{pll}$ ) and a bandwidth ( $\omega_{pll}$ ) to be about one-fifth of the bandwidth of current control loop and lower than the grid frequency, the controller gains can be calculated as follows:

$$k_i^{pll} = \frac{\omega_{pll}^2}{\sqrt{1 + (\tan(PM_{pll}))^2}} \quad (3.28)$$

$$k_p^{pll} = \frac{k_i^{pll} \tan(PM_{pll})}{\omega_{pll}} \quad (3.29)$$

As shown in Figure 3.8, the selected phase margin ( $PM_{pll}$ ) and cut-off frequency ( $\omega_{pll}$ ) of the PLL are  $84.4^\circ$  and 181 rad/s, respectively.

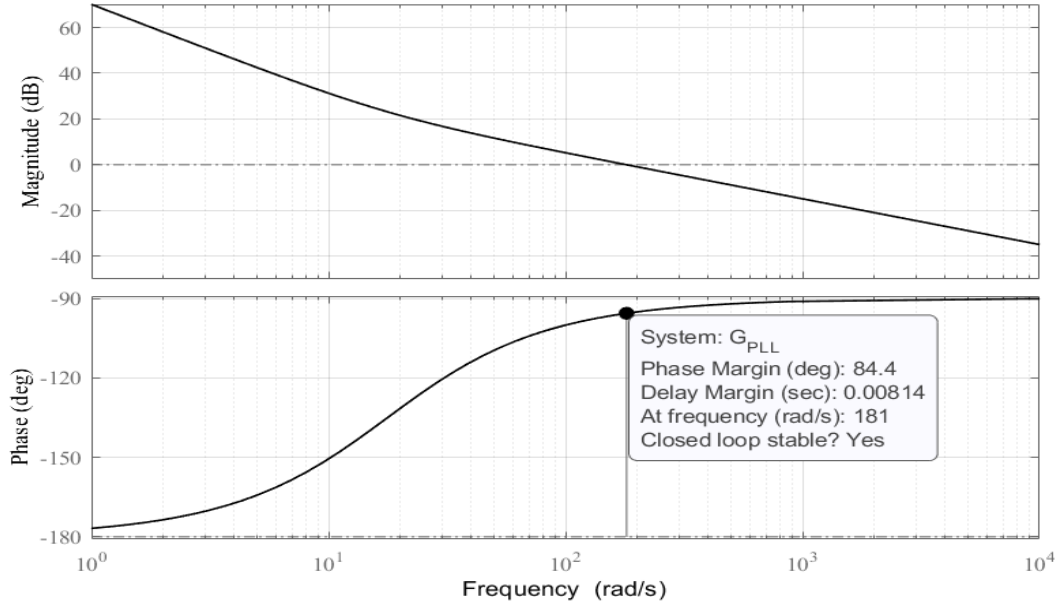


Figure 3.8: Bode plot of the open-loop PLL controller.

### 3.3.2 Inner Current Control

From the current control loop in Figure 3.7, the output voltage ( $v_{dq}^c$ ) in the converter-frame is obtained to generate the modulating signal for the VSC. A PI controller ( $G_i = k_p^i + k_i^i/s$ ) is implemented in the current control loop to regulate the injected active and reactive power to the utility. The dynamic equation describing the d-q current controller is implemented as follows:

$$v_{dq}^c = v_{dq}^c + j\omega^c L_f i_{dq}^c + G_i (i_{dq}^* - i_{dq}^c) \quad (3.30)$$

where  $j\omega^c L_f i_{dq}^c$  and  $v_{dq}^c$  are the decoupling and feedforward terms, respectively.

Using (3.14), (3.30) and applying the frame transformation, the open-loop gain of the current control loop is  $\ell_{cc}(s) = G_i / (L_f s + (R_f + r_{on}))$ . By setting the phase margin ( $PM_i$ ) at  $90^\circ$ , the controller gains can be calculated as follows:

$$k_i^i = \frac{R_f + r_{on}}{\tau_i} \quad (3.31)$$

$$k_p^i = \frac{L_f}{\tau_i} \quad (3.32)$$

where  $\tau_i$  is the time constant of the closed current loop. For fast current control response, the bandwidth of the closed control loop ( $\omega_i = 1/\tau_i$ ) is designed to be ten times smaller than the

switching frequency ( $\omega_{sw} = 2\pi f_{sw}$ ) of the VSC [8].

As shown in Figure 3.9, the designed phase margin and bandwidth ( $1/\tau_i$ ) of the closed-loop current control are  $90^\circ$  and 1922.7 rad/s, respectively.

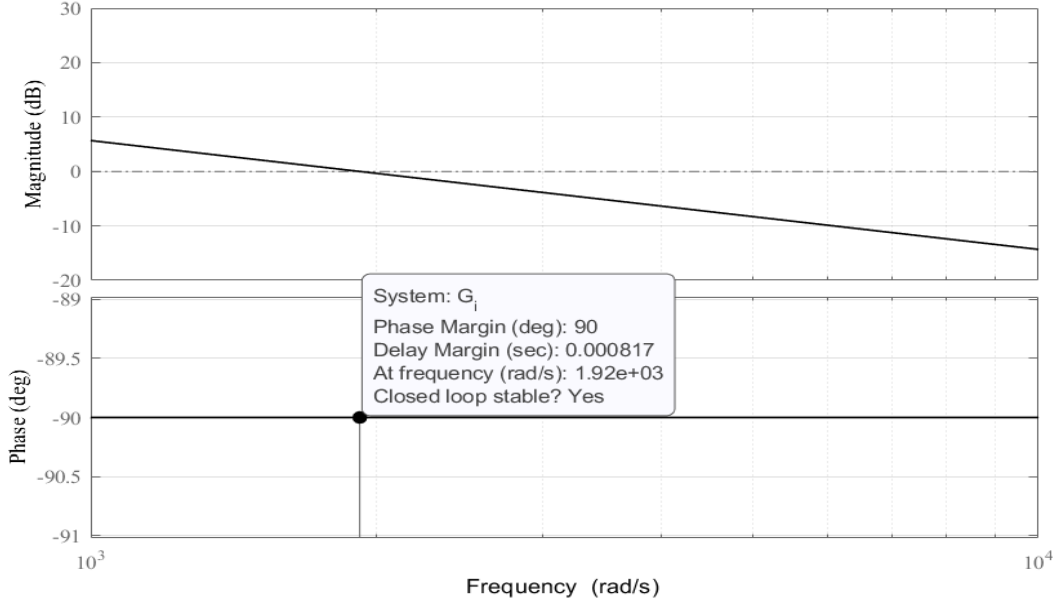


Figure 3.9: Bode plot of the open-loop current controller.

### 3.3.3 DC-Link Voltage Control

One of the main advantages of implementing the PLL in the vector control of VSC is the decoupled active and reactive power control [8]. As  $v_q = 0$ , the active power injection ( $P_{inv}$ ) is solely dependent on the active current component ( $i_d$ ). The dc-link voltage control bandwidth is designed with 10 – 20% of the bandwidth of the inner current controller. Therefore, the output of the dc-link voltage controller is  $i_d^* = i_d$ .

Referring to (3.19), the power difference between the delivered PV power  $P_{ext} = V_{dc}I_{pv}$  and the injected power  $P_{dc} \approx Real\{1.5v_{idq}i_{dq}^{conjugate}\}$  to the utility-grid is balanced by controlling the rate of change of the energy in the dc-link capacitance.

As shown in Figure 3.7, a PI controller ( $G_{vdc} = k_p^{vdc} + k_i^{vdc}/s$ ) is implemented in the dc-link voltage control loop to regulate the squared value of the dc-link voltage ( $V_{dc}^2$ ) to the squared reference value ( $V_{dc}^{2*}$ ) which is generated by the MPPT algorithm. In the literature, many different

MPPT methods have been introduced where the most widely used techniques are the perturb and observe (P&O), and incremental conductance (IC) [4]. More importantly, the dc-link voltage must satisfy the criteria  $V_{dc} \geq 2v_d^o$  when the conventional pulse-width-modulation (PWM) is employed and the criteria  $V_{dc} \geq 1.74v_d^o$  when PWM with third-harmonic injection is employed [8]. The dynamic equation describing the dc-link voltage controller is

$$i_d^* = \frac{\eta P_{ext} - G_{vdc}(V_{dc}^{2*} - V_{dc}^2)}{1.5v_d^o} \quad (3.33)$$

where  $\eta$  is a constant used to enable the feed-forward power compensation to reduce the nonlinearity effect of the PV generator.

Considering a unity PCC voltage, a real power control response  $\left(P_{pcc} = \frac{P_{pcc}^*}{\tau_i s + 1}\right)$ , an instantaneous power of VSC interface reactors and using (3.19b) and (3.33), the accurate open-loop gain of the dc-link voltage control loop is  $\ell_{vdc}(s) = \left(2G_{vdc}(\tau_p s + 1)\right) / (C_{dc}s(\tau_i s + 1))$ , where  $\tau_p = 2L_{dc}P_{pv}^o / 3v_d^{o2}$  is a positive time-constant given in terms of the operating points [8]. Note that  $\ell_{vdc}(s)$  has three poles; two at zero and one at  $(1/\tau_i)$ . The phase angle of  $\ell_{vdc}(j\omega)$  at low and high frequencies is  $-180^\circ$  and  $-90^\circ$ , respectively. By selecting a proper phase margin ( $PM_{vdc}$ ) and a crossover frequency ( $\omega_{vdc}$ ) to be about one-fifth of the bandwidth of current control loop [8], The dc-link voltage controller gains can be calculated as follows:

$$k_i^{vdc} = \frac{C_{dc}\omega_{vdc}^2 \sqrt{1 + (\omega_{vdc}\tau_i)^2}}{2\sqrt{1 + (\tan(\theta_{vdc}))^2} \sqrt{1 + (\omega_{vdc}\tau_p)^2}} \quad (3.34)$$

$$k_p^{vdc} = \frac{k_i^{vdc} \tan(\theta_{vdc})}{\omega_{vdc}} \quad (3.35)$$

where  $\theta_{vdc}$  is given by  $\theta_{vdc} = PM_{vdc} + \tan^{-1}(\omega_{vdc}\tau_i) - \tan^{-1}(\omega_{vdc}\tau_p)$ .

Ignoring the instantaneous power of the VSC interface reactors, the simplified open-loop gain becomes  $\ell_{vdc}(s) = (2G_{vdc}) / (C_{dc}s(\tau_i s + 1))$ . The phase angle of  $\ell_{vdc}(j\omega)$  at both low and high frequencies is  $-180^\circ$ , The phase margin of the simplified open-loop increases to the maximum value at a certain frequency  $\left(\omega_{vdc}^{max} = \sqrt{k_i^{vdc} / (\tau_i k_p^{vdc})}\right)$ . As a result, the controller gains can be calculated at  $(\omega_{vdc}^{max})$  as

$$k_i^{vdc} = \sqrt{\frac{C_{dc}^2 (\omega_{vdc}^{max})^4 (1 + (\tau_i \omega_{vdc}^{max})^2)}{4(1 + (1/(\tau_i \omega_{vdc}^{max}))^2)}} \quad (3.36)$$

$$k_p^{vdc} = \frac{k_i^{vdc}}{\tau_i (\omega_{vdc}^{max})^2} \quad (3.37)$$

VSC operates in the inverting mode where the real-power flow is between zero and maximum power delivered by the PV plant. In this study,  $\tau_p$  is very small and insignificant. As a result, the proportional and integral gains have approximately the same values for both accurate and approximated dc-link voltage controllers at the same phase margin and cut-off frequency.

To achieve the same proportional and integral gains given in Appendix A.3.1, the phase margin ( $PM_{vdc}$ ) and cut-off frequency ( $\omega_{vdc}$ ) for both the accurate and approximated models in (3.34)-(3.35) and (3.36)-(3.37) should be designed at  $85.8^\circ, 193.8 \text{ rad/s}$  and  $78.6^\circ, 192.3 \text{ rad/s}$ , respectively, as shown in Figure 3.10, and Figure 3.11.

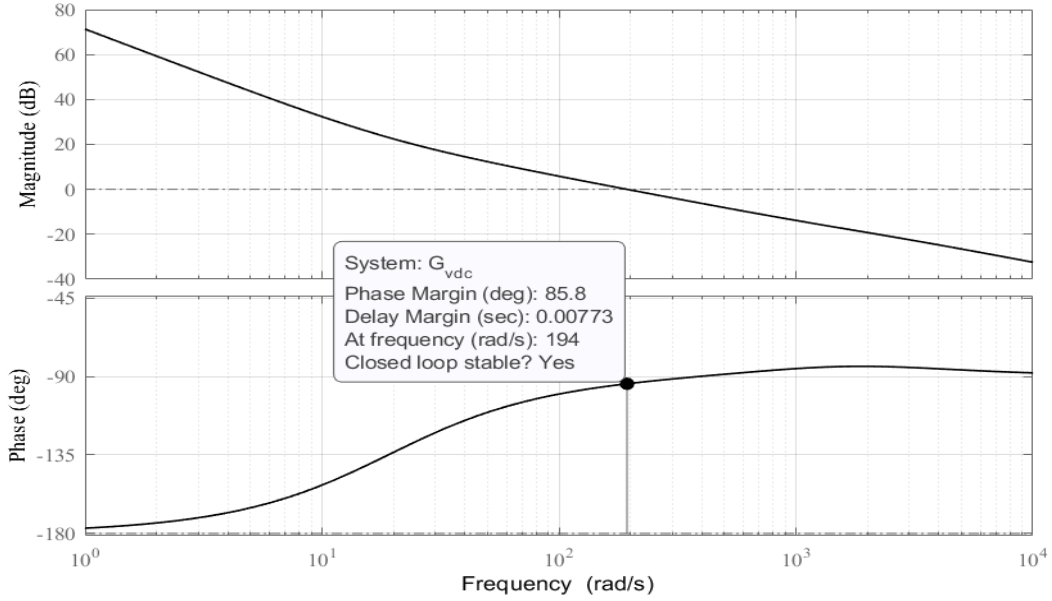


Figure 3.10: Bode plot of the open-loop accurate dc-link voltage controller.

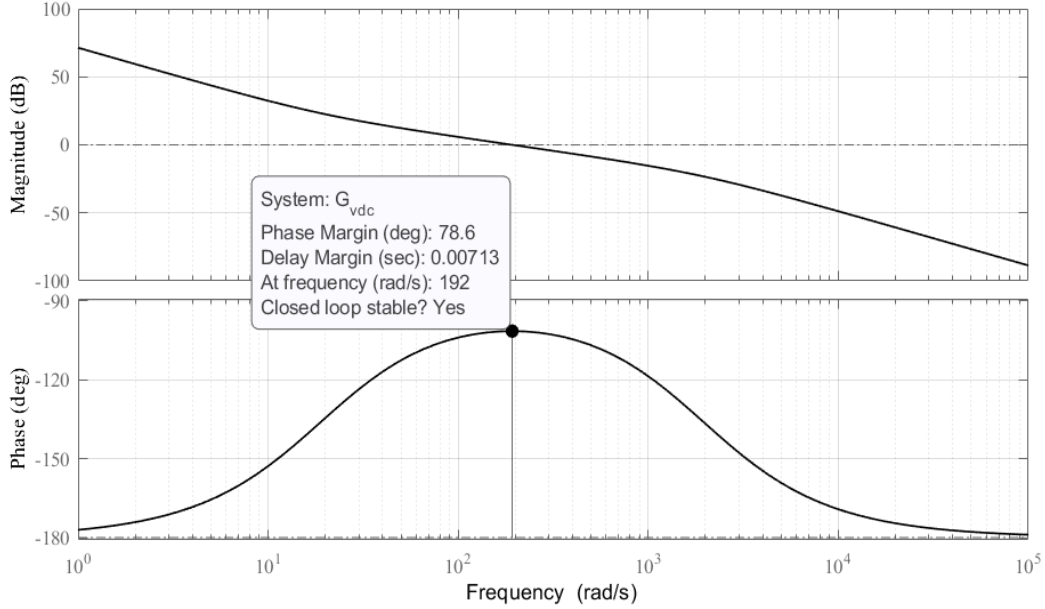


Figure 3.11: Bode plot of the open-loop approximated dc-link voltage controller.

### 3.3.4 PCC Utility-Grid Voltage Control

Similarly, as in the dc-link voltage control, the reactive power injection ( $Q_{inv}$ ) is determined by the reactive current component ( $i_q$ ) due to the implementation of the PLL. The ac-voltage controller bandwidth is designed with 10 – 20% of the bandwidth of the inner current controller. Therefore, the output of the ac-voltage controller is  $i_q^* = i_q$  [8].

As shown in Figure 3.7, A PI controller ( $G_{vac} = k_p^{vac} + k_i^{vac}/s$ ) is implemented in the ac voltage control loop to regulate the PCC voltage to unity by generating a reference  $q$ -component of the injected current ( $i_q^*$ ) to maintain the reactive power. The dynamic equation of the ac voltage controller is given as follows:

$$i_q^* = \frac{-G_{vac}(v_d^* - v_d)}{1.5v_d^o} \quad (3.38)$$

The ac voltage controller is designed in a similar way as the design of the dc-link voltage controller. Considering the current control response and using (3.15) and (3.38), the open-loop transfer function of the ac voltage control loop becomes  $\ell_{vac}(s) = (2\omega^g N^2 L_T / 3v_d^o)(G_{vac}/(\tau_i s + 1))$ , the phase angle of  $\ell_{vac}(j\omega)$  at low and high frequencies is

$-90^\circ$ . By selecting a proper phase margin ( $PM_{vac}$ ) and a crossover frequency ( $\omega_{vac}$ ) to be about one-fifth of the bandwidth of current control loop, the ac-voltage controller gains can be calculated as follows:

$$k_i^{vac} = \frac{3v_d^o \omega_{vac} \sqrt{1 + (\omega_{vac} \tau_i)^2}}{2\omega^o N^2 L_T \sqrt{1 + (\tan(\theta_{vac}))^2}} \quad (3.39)$$

$$k_p^{vac} = \frac{k_i^{vac} \tan(\theta_{vac})}{\omega_{vac}} \quad (3.40)$$

where  $\theta_{vac}$  is given by  $\theta_{vac} = PM_{vac} - 90 + \tan^{-1}(\omega_{vac} \tau_i)$ .

As shown in Figure 3.12, the designed phase margin ( $PM_{vac}$ ) and cut-off frequency ( $\omega_{vac}$ ) of the ac voltage control open-loop are  $86.4^\circ$  and 130 rad/s, respectively.

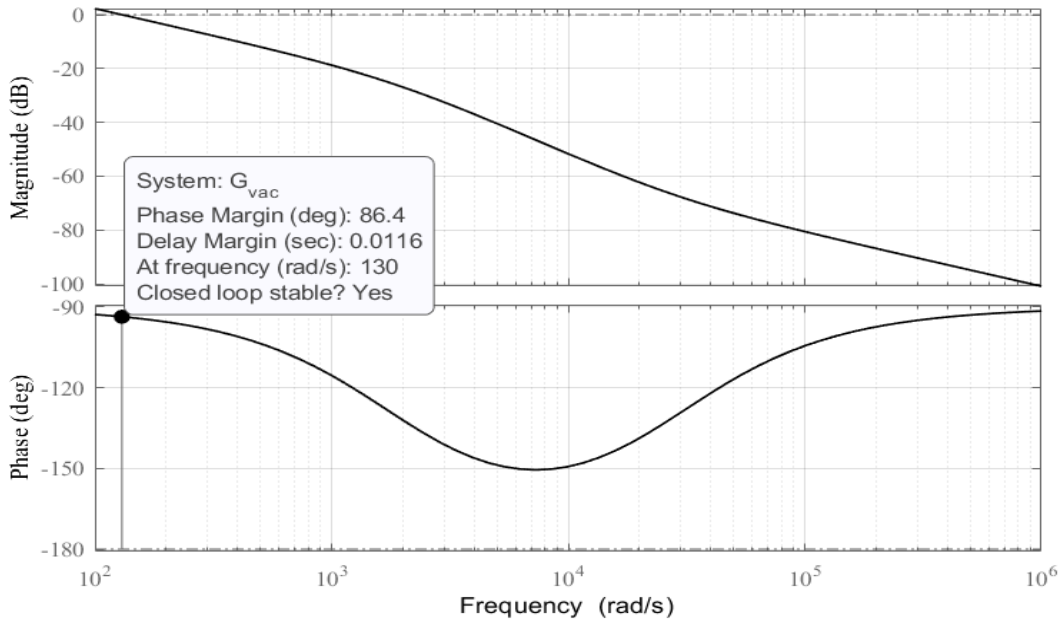


Figure 3.12: Bode plot of the open-loop PCC voltage controller.

### 3.4 Small-Signal Modeling and Analysis

To study the dynamic stability of the grid-connected PV system, a detailed small-signal model has been developed by linearizing the nonlinear equations  $\dot{x} = F(x(t), u(t))$  in Sections 3.2 and 3.3. The linearized state-space model of the overall system is defined in Appendix A.3.3 and is given as follows:

$$\begin{aligned}\dot{\Delta x} &= A\Delta x + B\Delta u \\ \Delta y &= C\Delta x + D\Delta u\end{aligned}\quad (3.41)$$

where  $A = (\partial F(x, u)/\partial x)|_{(x,u)=(x^o,u^o)}$  is the system matrix;  $B = (\partial F(x, u)/\partial u)|_{(x,u)=(x^o,u^o)}$  is the control matrix;  $C$  is the output matrix;  $D$  is the feed-forward matrix; and the perturbation variables  $\Delta x$ ,  $\Delta u$ , and  $\Delta y$  are the state, input, and output vectors, respectively.

The resultant multiple-input multiple-output (MIMO) model in (3.41) consists of 14 state variables and five inputs where  $\Delta x = [\Delta i_d^g \ \Delta i_q^g \ \Delta i_{gd}^g \ \Delta i_{gq}^g \ \Delta v_d^g \ \Delta v_q^g \ \Delta \varphi_d^i \ \Delta \varphi_q^i \ \Delta \varepsilon \ \Delta \varphi_\varepsilon^{pll} \ \varphi_v^{ac} \ \Delta V_{dc}^2 \ \Delta \varphi_v^{dc} \ \Delta I_{pv}]^T$  and  $\Delta u = [\Delta V_{dc}^{2*} \ \Delta P_{pv} \ \Delta v_d^* \ \Delta v_{gd}^g \ \Delta v_{gq}^g]^T$ .

### 3.5 Evaluation Results

A detailed nonlinear time-domain simulation model for the VSC-based PV system is developed within Matlab/Simulink® environment to evaluate the preceding theoretical analysis and validate the accuracy of the small-signal model. The complete model entities are built using both SimPowerSystem® and Simulink toolboxes. The VSC is simulated using the average-model-based blocks. The simulation type is discrete with a sample time of 50  $\mu$ s, and the complete system parameters are shown in Appendix A.3.1.

#### 3.5.1 Large-Signal Non-Linear Models

Two types of the non-linear time-domain simulation models are introduced to validate the analytical results. The first type is the Simulink large-signal model where the complete model is built using the SimPowerSystem® toolbox, the VSC is simulated using the average-model-based blocks or the switching-model-based blocks, and the simulation type could be continuous or discrete with a certain sampling time. The second type is the mathematical large-signal model, where the complete model is built by aggregating the nonlinear system equations using the Simulink toolbox.

As shown in Figures 3.13, 3.14, and 3.15, the proportional gain of the dc-link voltage controller is decreased to produce an oscillatory and lightly damped response, and, therefore, the two non-linear models can be verified in order to use them to evaluate the theoretical analysis and validate the accuracy of the small-signal model.

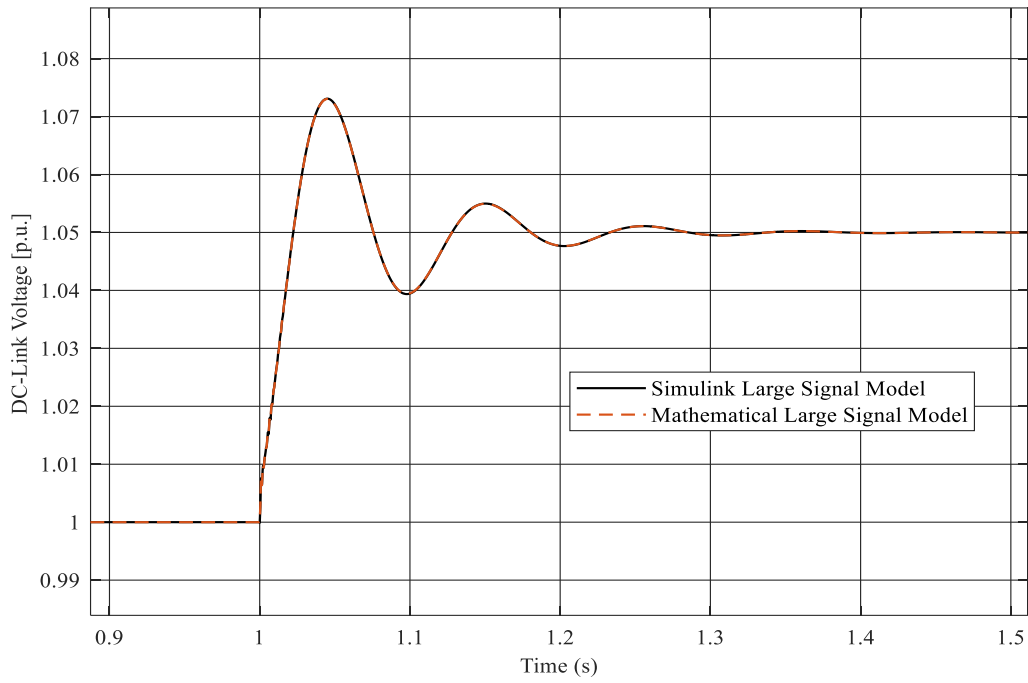


Figure 3.13: The dc-link voltage of the large-signal model.

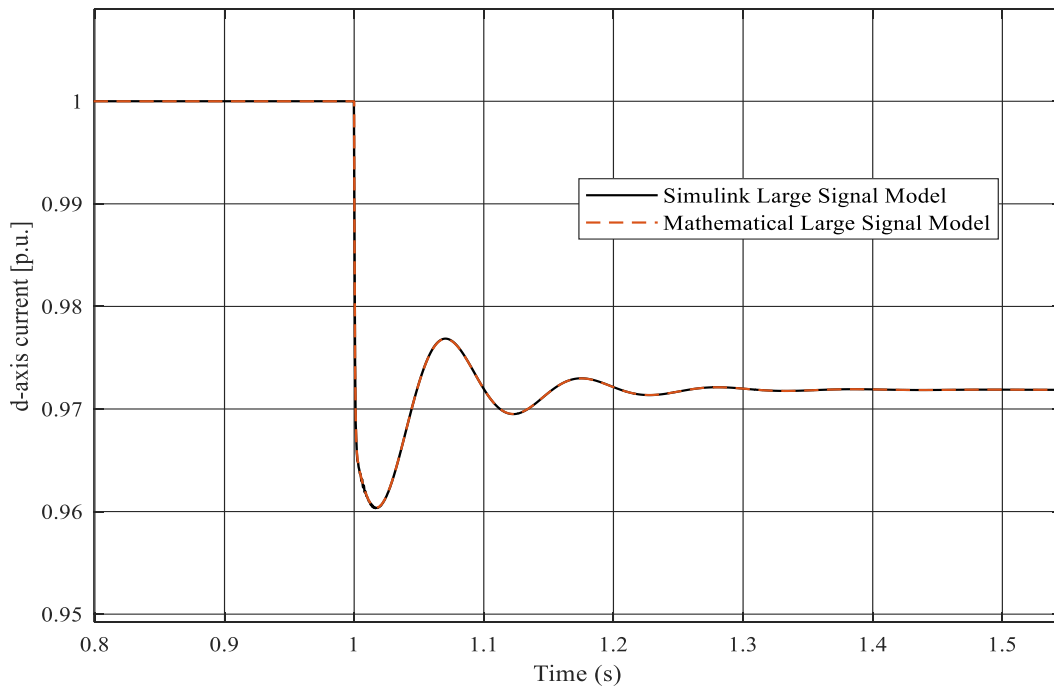


Figure 3.14: d-axis current of the large-signal model.

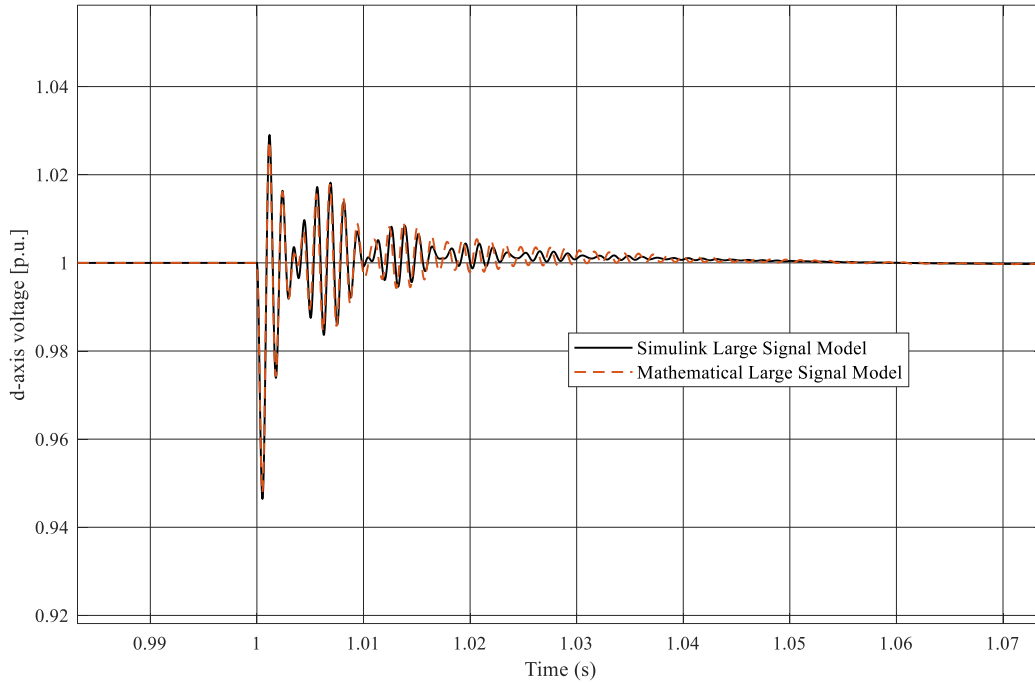


Figure 3.15: d-axis PCC voltage of the large-signal model.

### 3.5.2 Small-Signal Model Validation

To evaluate the accuracy of the small-signal state-space model in (3.41), a perturbation with a 5% step increase in  $V_{dc}$  is applied under the steady-state condition at  $t = 1$ s. To compare the linearized model with the actual model and validate the accuracy, the proportional gain of the dc-link voltage controller is decreased to increase the bandwidth of the dc-link voltage control loop, which in turn produce an oscillatory and lightly damped response, and, therefore, the model can be verified even in the presence of lightly damped oscillations.

As shown in Figures 3.16, 3.17, and 3.18, The model accuracy is validated at two different conditions, where the dominant damped and lightly-damped eigenvalues of the small-signal model are  $\lambda \approx -20$  and  $\lambda \approx -14 \pm j57$ , respectively.

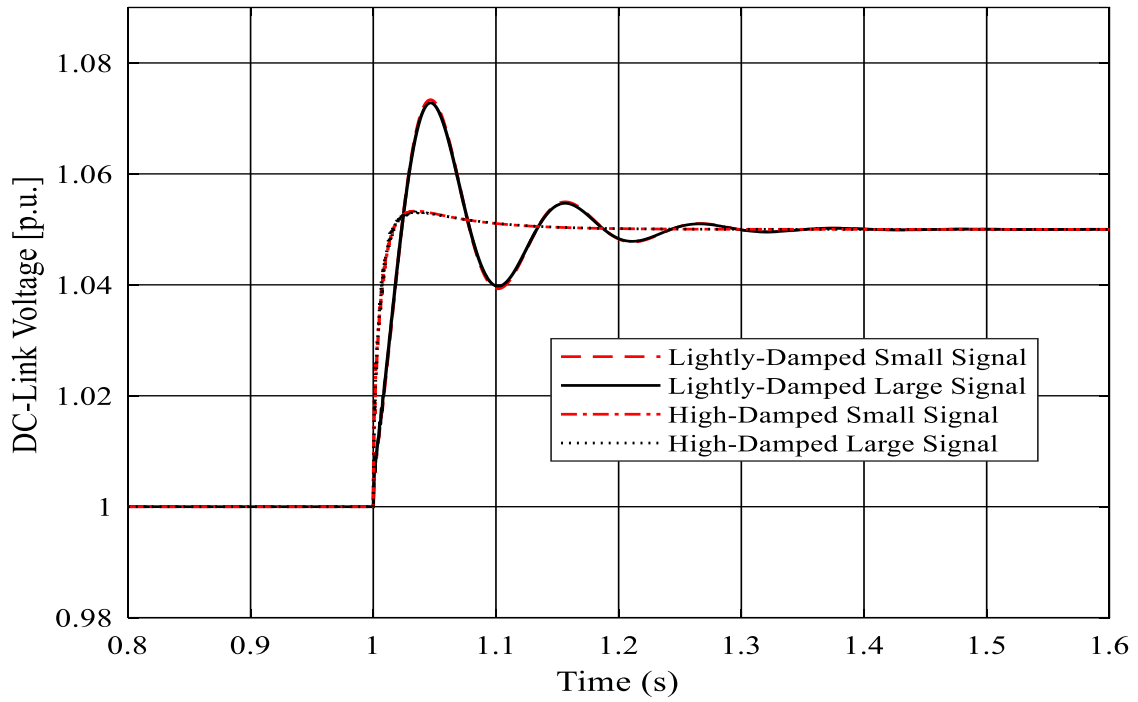


Figure 3.16: DC-link voltage response of the verified small-signal model at two different conditions.

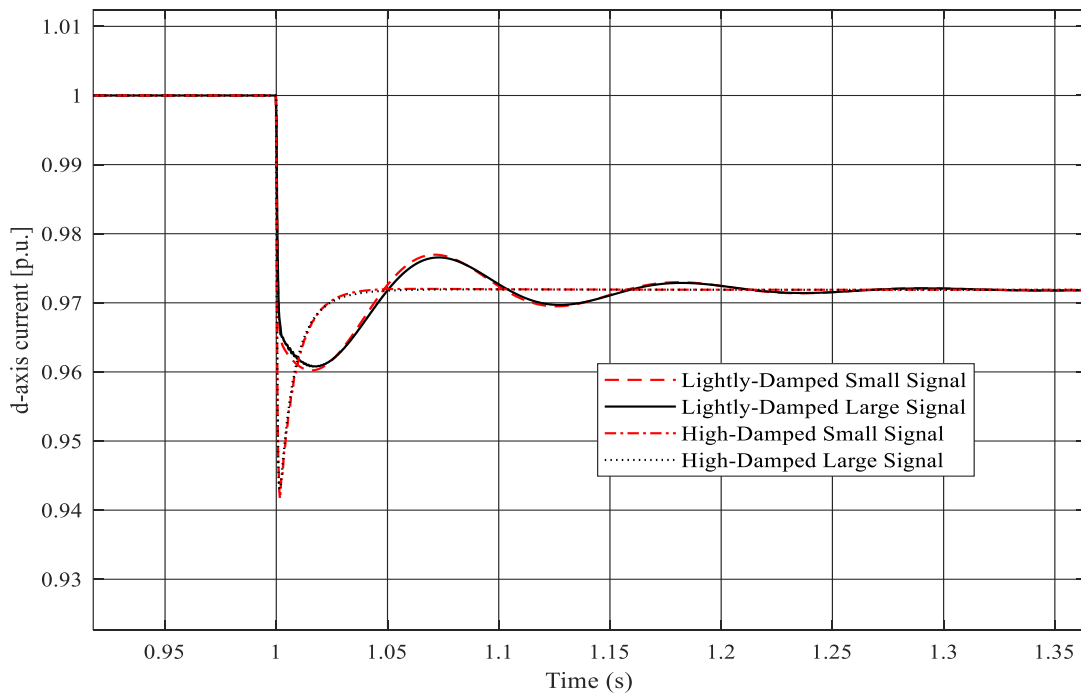


Figure 3.17: D-axis current response of the verified small-signal model at two different conditions.

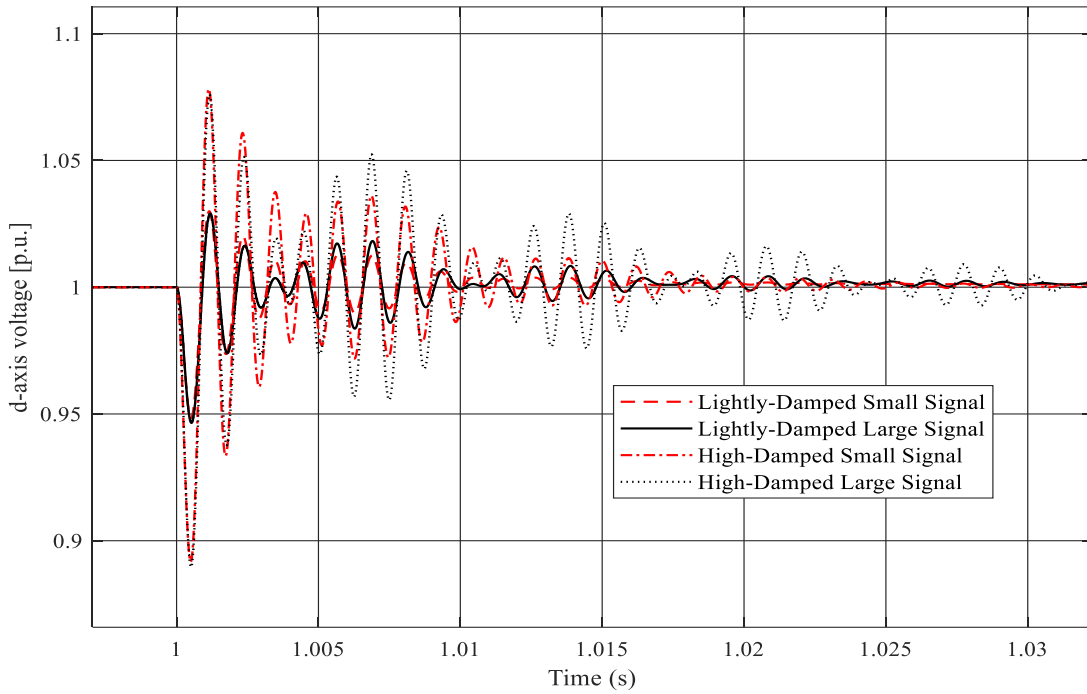


Figure 3.18: D-axis PCC-voltage response of the verified small-signal model at two different conditions.

### 3.5.3 Approximated and Accurate Models of the DC-Link Voltage Controller

As discussed in section 3.3, the small-signal model can be modeled accurately or approximately based on the applied dc-link voltage controller and considering the instantaneous power of the ac-filter in the linearized model.

As shown in Figures 3.19, and 3.20, the accurate model is selected in this study to accurately validate the analytical results.

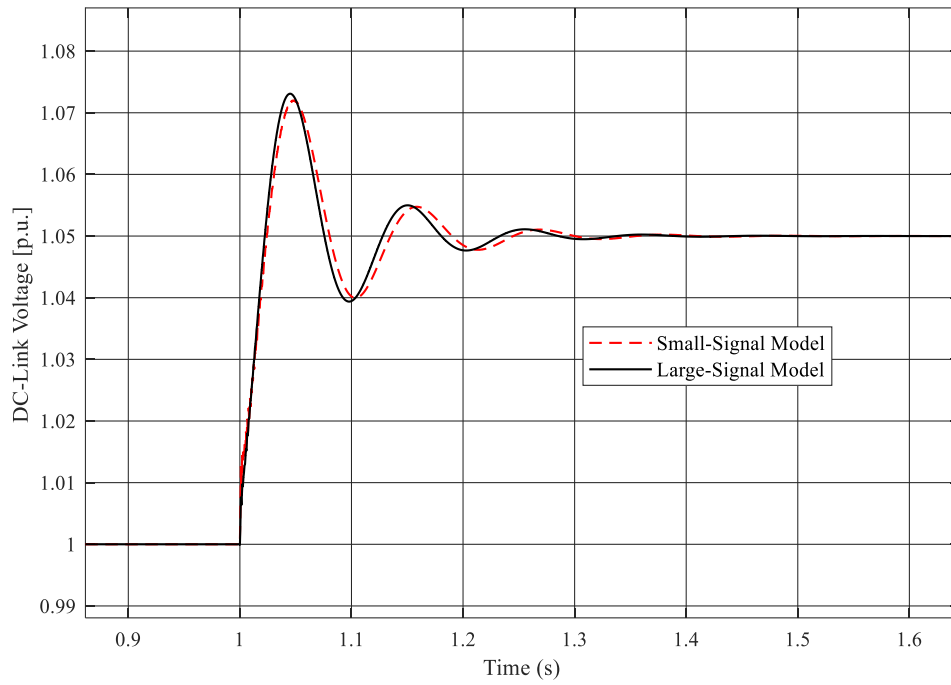


Figure 3.19: DC-Link voltage response of the approximated model at lightly-damped condition.

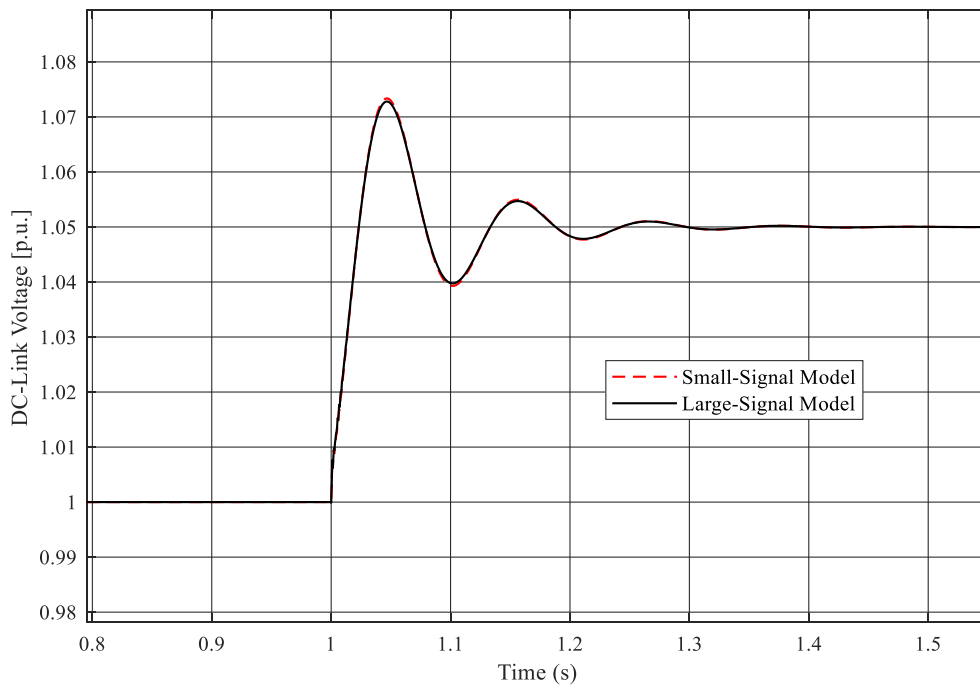


Figure 3.20: DC-Link voltage response of the accurate model at lightly-damped condition.

### 3.5.4 Dominant Eigenvalues

As discussed in Chapter 2, the selective model analysis is used to study the power system dynamic stability using both eigenvalues and participation factor analysis. Eigenvalues of the linearized model are used to study the system stability, whereas the participation factor, which is defined by left-right eigenvectors multiplication is used to study the relationship between states and modes. The participation factor of k-states in j-modes is given in Section 2.6.2.

As shown in Figures 3.16 and Table 3.1, the most dominant eigenmodes of damped and lightly- damped systems are influenced by the dc-link voltage state.

Table 3.1: Participation Factor Analysis of the Damped and Lightly-Damped Systems.

Eigenmodes of the Lightly-Damped System	Influencing State(s)/ Controllers	Eigenmodes of the Damped System	Influencing State(s)/ Controllers
$\lambda_1 = -2.7585E6$	$\Delta I_{pv}$ DC-Cable	$\lambda_1 = -2.7585E8$	$\Delta I_{pv}$ DC-Cable
$\lambda_{2,3} = -80.3 \pm 5415.9i$	$\Delta i_{gd}, \Delta v_d$	$\lambda_{2,3} = -16.83 \pm 5490i$	$\Delta i_{gd}, \Delta v_d$
$\lambda_{4,5} = -131 \pm 4534.6i$	$\Delta i_{gq}, \Delta v_q$	$\lambda_{4,5} = -107.1 \pm 4562.4i$	$\Delta i_{gq}, \Delta v_q$
$\lambda_6 = -1956.3$	$\Delta i_d$	$\lambda_6 = -2185.2$	$\Delta i_d$
$\lambda_7 = -1636.1$	$\Delta i_q$	$\lambda_7 = -1641.2$	$\Delta i_q$
$\lambda_8 = -216.9$	$\Delta \varepsilon$ PLL-Controller	$\lambda_8 = -252.6$	$\Delta \varepsilon$ PLL-Controller
$\lambda_{9,10} = -14.06 \pm 57.3i$	$\Delta \varphi_v^{dc}, \Delta V_{dc}$ DC-Controller	$\lambda_9 = -110.71$	$\Delta \varphi_v^{dc}$ DC-Controller
$\lambda_{11} = -35.87$	$\Delta \varphi_v^{ac}$ AC-Controller	$\lambda_{10} = -40.21$	$\Delta \varphi_v^{ac}$ AC-Controller
$\lambda_{12} = -20$	$\Delta \varphi_d^i$ / Current-Controller	$\lambda_{11,12} = -20.46 \pm 0.20i$	$\Delta \varphi_\varepsilon^{pll}, \Delta V_{dc}$ / PLL & DC-Controller

$\lambda_{13,14} = -19.8 \pm 0.147i$	$\Delta\varphi_{\varepsilon}^{pll}, \Delta\varphi_q^i$ / PLL & Current- Controller	$\lambda_{13} = -20$	$\Delta\varphi_d^i$ / Current- Controller
-	-	$\lambda_{14} = -19.87$	$\Delta\varphi_{\varepsilon}^{pll}, \Delta\varphi_q^i$ / PLL & Current- Controller

### 3.6 Conclusion

Comprehensive modeling and control of the grid-connected VSC system have been investigated. Moreover, the development of analytical expressions for systematic and accurate calculations of all VSC controllers' gains have been introduced to easily determine the gains of the proportional and integral terms of each controller. Further, PV dynamic and static impedances are identified under all PV operation regions. In order to study the system stability and performance, a detailed small-signal model, mathematical and Simulink large-signal models are developed. Also, the simulation results of the three models have been compared and validated.

# Chapter 4

## Assessment and Mitigation of Dynamic Interactions in Grid-Connected PV-VSC Systems

### 4.1 Introduction

As discussed in Chapter 2, it is reported in the literature that, with a reduced dc-link capacitance, the VSC dynamics involve right-half plane poles in many applications. In the PV applications, the impact of the dynamic impedance of PV arrays on a grid-connected VSC with a reduced dc-link capacitance was solely addressed in [11].

In [11], The dynamic impedance of the PV generator is analyzed. Instabilities due to the RHP poles in the dc-link voltage control loop are investigated. The unstable behavior is expected in both single- and two-stage systems especially, with a reduced dc-link capacitance. An approximate expression for the minimum dc-link capacitance required to guarantee the stability is developed. This study reported that the dynamic stability of the dc-link voltage control could be affected when the PV generator operates in the constant current region. However, this effect is alleviated when the PV generator operates at the maximum power point or constant voltage region. The developed model in [11] does not consider the influence of the step-up transformer, dc-cables, the grid-stiffness, the phase-locked loop, and ac-voltage control dynamics. More importantly, there is no proposed solution or mitigation technique to enhance system stability and facilitate the integration of PV generators with reduced dc-link capacitance.

Motivated by the preceding challenges, a comprehensive model is developed in this chapter. Moreover, a new, yet simple, and efficient compensator is introduced to overcome the dynamic instabilities due to the variable operating conditions, especially under minimized dc-link capacitance.

### 4.2 Instabilities Due to PV and DC-link Interactions

The unstable dynamic interaction between the PV generator and the dc-side of the VSC at different operating conditions is demonstrated using eigenvalues and impedance analysis. The PV system stability is preserved at the MPP and CVR of the  $V_{pv} - P_{pv}$  curve of PV array. On the contrary, the stability is violated in the CCR only when  $C_{dc}$  is reduced to values below the stability margin value

of the dc-link capacitance. The state-space model of the comprehensive system is developed in Appendix A.4.1.

Figure 4.1 shows the eigenvalue analysis at the CCR with different values of the dc-link capacitance. The high-frequency eigenmode is migrated to the right-half-plane in the  $s$ -domain despite the robustness of the dc-link voltage controller [proportional and integral gains of the dc-link voltage controller are changed accordingly to fix both of phase margin and bandwidth at the required values for stable operation].

The unstable performance in Figure 4.1 is reflected on the incremental impedance ( $\Delta Z_l(s)$ ) of the grid-connected VSC system. The source dynamic impedance ( $\Delta Z_s(s)$ ) can be found using (3.21) and (3.24). The location of the source and load impedances are shown in Figure 3.1.

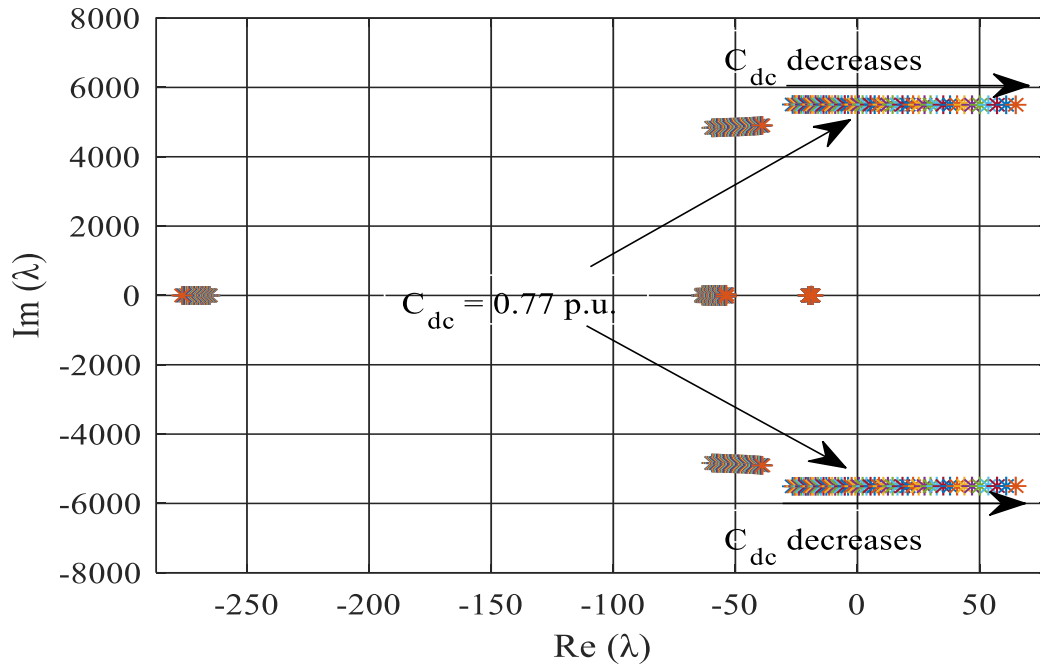


Figure 4.1: Eigenvalue analysis of the influence of the dc-link capacitance on the uncompensated system.

$\Delta V_{dc}$  and  $\Delta V_{dc}^2$  are linearized as in (4.1a) and (4.1b), respectively. The identity ( $\Delta V_{dc}^2 \approx 2V_{dc}^o \Delta V_{dc}$ ) can be obtained by substituting (4.1a) in (4.1b). As a result, the load impedance ( $\Delta Z_l(s) = \Delta V_{dc} / \Delta I_{dc}$ ) can be found as shown in Appendix A.4.1.

$$V_{dc} \triangleq V_{dc}^o + \Delta V_{dc} \quad (4.1a)$$

$$V_{dc}^2 \triangleq (V_{dc}^o)^2 + \Delta V_{dc}^2 \quad (4.1b)$$

As shown in Figure 4.2, the uncompensated model is consistent with the results of the eigenvalue analysis in Figure 4.1, where the system stability is violated at a dc-link capacitance of 0.77 p.u. under CCR operation.

As shown in Table 4.1, the violation of the Nyquist criterion occurs at 5498.6 rad/s, which is clearly influenced by voltage controller states.

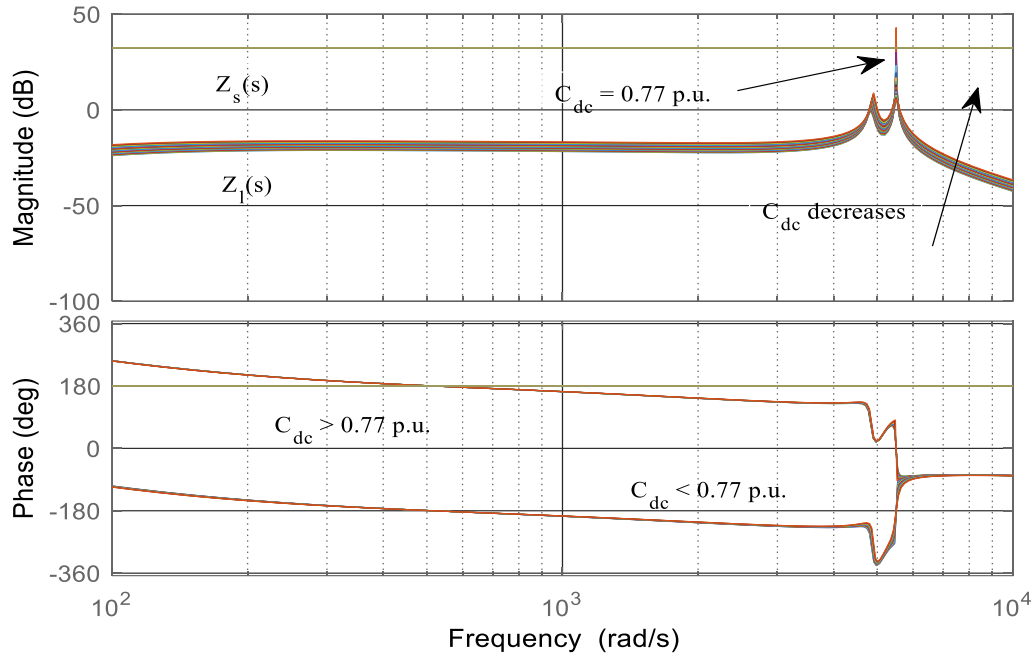


Figure 4.2: Impedance analysis of the influence of the dc-link capacitance on the uncompensated system.

The analysis showed that the unstable oscillation is not due to the resonance of LC on the dc-side, and the dc-line does not affect the system stability under any conditions. As shown in Table 4.1, the dc-line influences only the farthest eigenvalue in the left-half-plane (LHP) and has no significant effect on the unstable eigenmode.

Table 4.1: Participation-Factor analysis of the uncompensated system under unstable operating conditions.

Eigenmodes	Influencing State(s)/Controllers
$\lambda_1 = -1.2189E8$	$\Delta I_{pv}$ / DC-Cable
$\lambda_{2,3} = 64.8 \pm 5498.6i$	$\Delta V_{dc}$ / DC-Controller
$\lambda_{4,5} = -38.9 \pm 4904.2i$	$\Delta i_{gd}, \Delta i_{gq}, \Delta v_d, \Delta v_q$



$$i_d^*|_{total} = \frac{\eta P_{ext} - G_{vdc}(V_{dc}^{2*} - V_{dc}^2)}{1.5v_d^0} + I_{dmp} \quad (4.3)$$

$$I_{dmp} = \alpha \underbrace{\frac{C_{dc}R_{C_{dc}}s}{C_{dc}R_{C_{dc}}s + 1}}_{H(s)} \underbrace{\frac{1}{\tau s + 1}}_{I_{C_{dc}}}(sC_{dc}V_{dc}) \quad (4.4)$$

where  $I_{dmp}$  is the added damping current;  $\alpha$  is a gain used to enhance the high-frequency attenuation;  $H(s)$  is a high-pass filter with a time-constant equals  $C_{dc}R_{C_{dc}}$ ; and  $I_{C_{dc}}$  is the dc-link capacitor current which is constructed practically by filtering the derivative of dc-link voltage using a low-pass filter with a time constant ( $\tau$ ). As a result, the damping current can be obtained by applying the dc-link voltage to a double high-pass filter with a suitable cut-off frequency.

Two more states are added to the model to stabilize the system. The influence of the proposed compensator on the dynamic response of the system is shown in Figures 4.4 and 4.5. As compared to the uncompensated case, the stability margin is increased by moving the eigenvalues to the left-half-plane, and the system is robustly damped with a dominant damping ratio  $\lambda \approx -20$  as in the normal operation when the dc-link capacitance is 1 p. u.

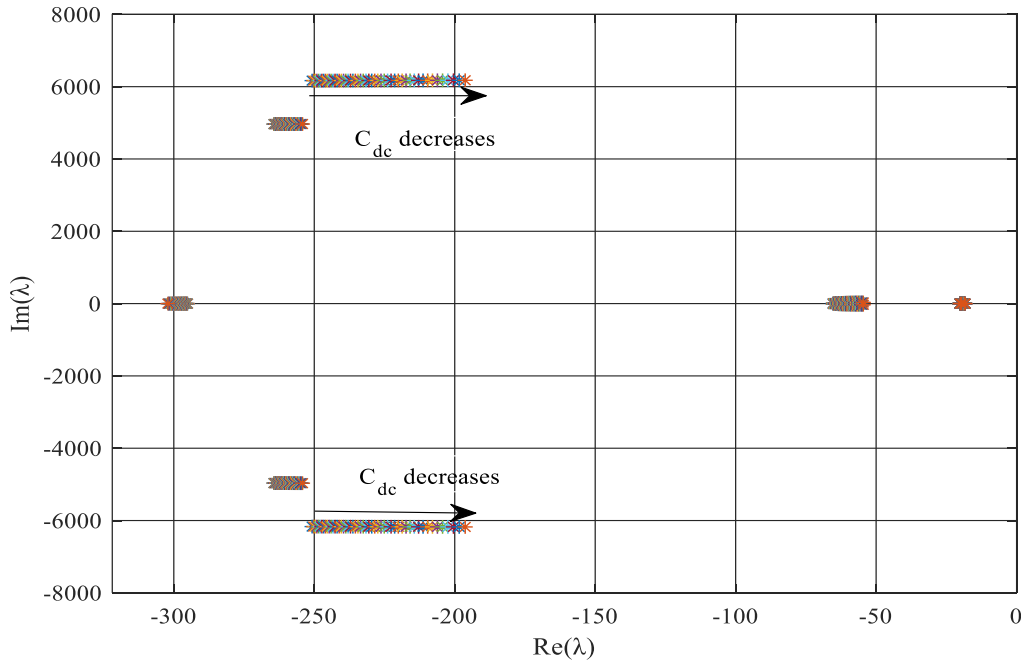


Figure 4.4: Eigenvalue analysis of the influence of the dc-link capacitance on the compensated system.

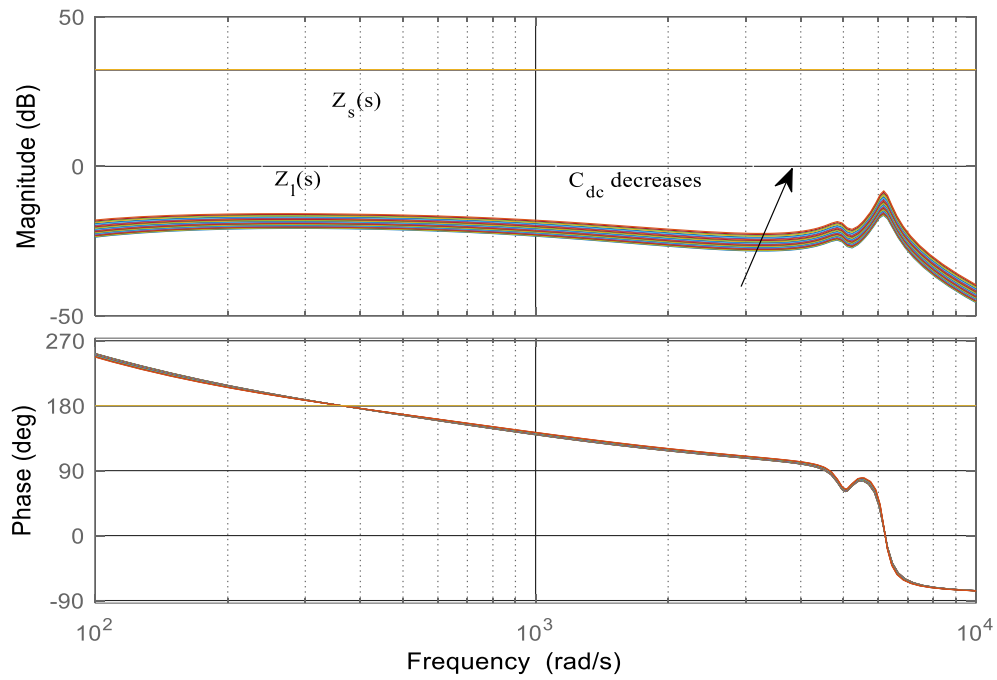


Figure 4.5: Impedance analysis of the influence of the dc-link capacitance on the compensated system.

### 4.3.2 Sensitivity Analysis

As shown in Figure 4.6, the active compensator does not influence the dc-link voltage controller and the steady-state performance of the grid-connected VSC. Moreover, the proposed compensator enhances the transient response by mitigating the resonance frequency at  $\omega \approx 4860$  rad/s, which is induced by the ac-filter.

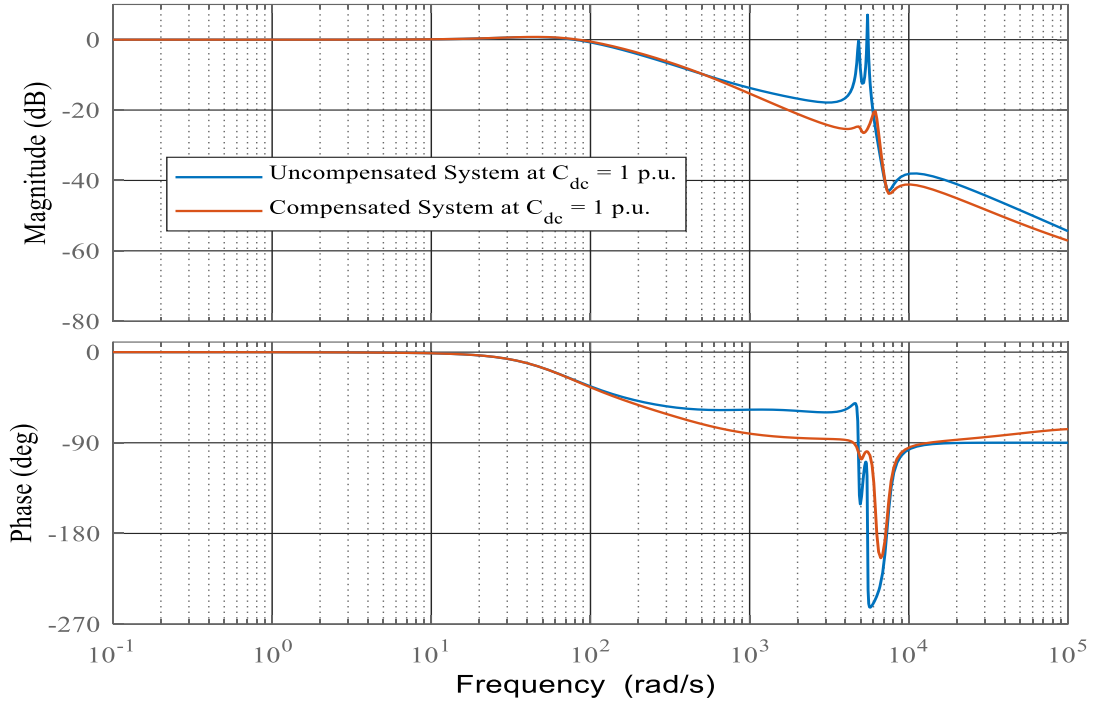


Figure 4.6: Transfer function of the closed-loop dc-link voltage controller at  $c_{dc} = 1$  p.u. for both compensated and uncompensated systems.

## 4.4 Evaluation Results

A large-signal time-domain simulation model of the system under study in Figure is implemented under the Matlab/Simulink environment to evaluate the analytical results and validate the performance of the proposed active compensator.

The complete model entities are built using the SimPowerSystem® toolbox. The VSC is simulated using average-model-based blocks. The simulation type is discrete with a sample time of  $50 \mu\text{s}$ , and the complete system parameters are shown in Appendix A.4.2.

### 4.4.1 Influence of Reduced DC-Link Capacitance

Figure 4.7 shows the uncompensated response at different dc-link voltage levels under all PV operation regions and different dc-link capacitance values. The system operates in the CVR, MPP, and CCR at  $t = 0 - 3$  s,  $t = 3 - 4$  s, and  $t = 4 - 7$  s, respectively.

The dc-link voltage has significant high-frequency oscillations that affect the system dynamic stability when the system operates at the CCR and reduced dc-link capacitance values lower than 0.77 p.u.

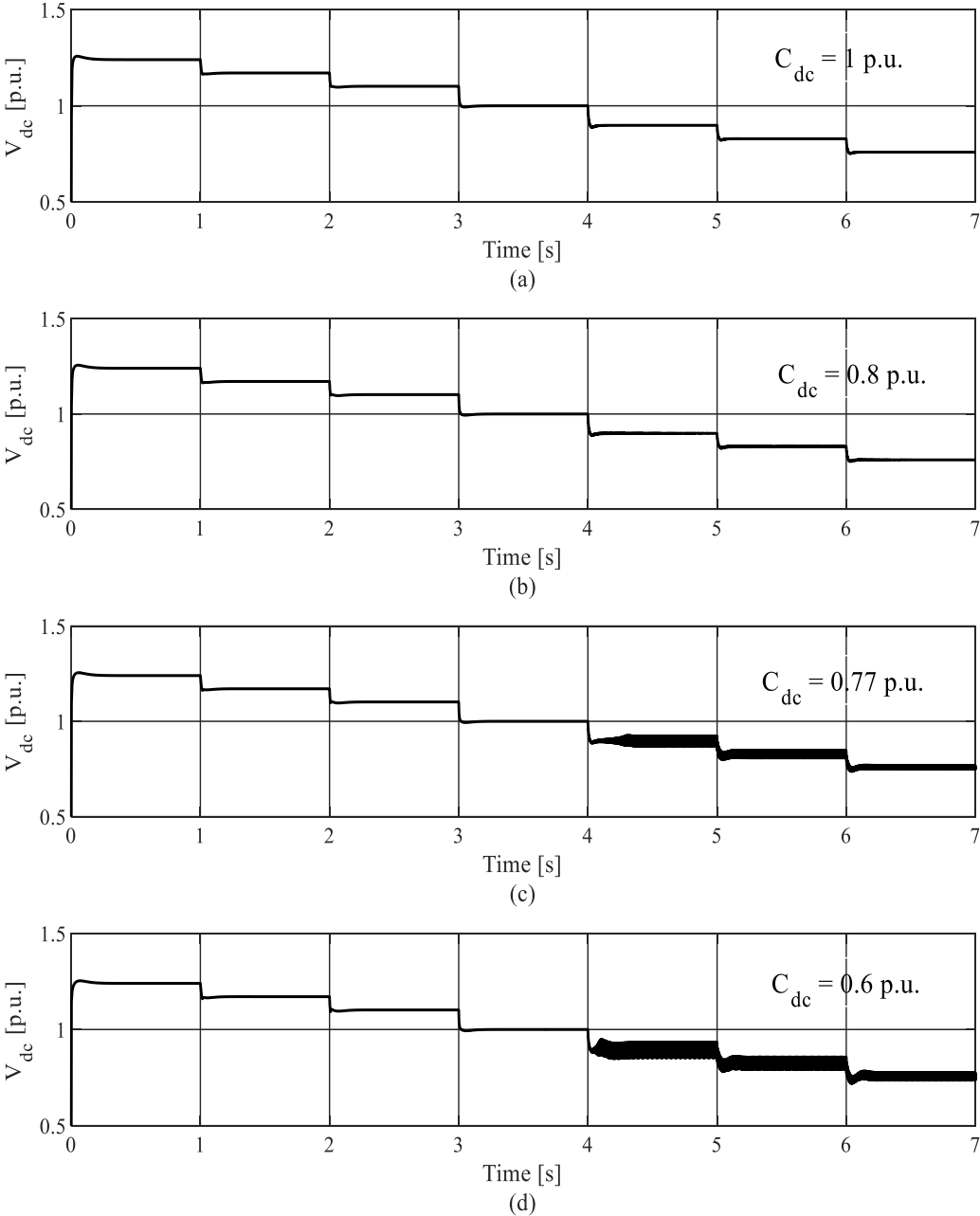


Figure 4.7: Uncompensated system response at different voltage levels and dc-link capacitance values.

#### 4.4.2 Active Compensated Interaction

The active compensated response using the outer loop compensator is shown in Figure 4.8. The dc-link voltage is highly damped with no overshoots at ( $t = 1.3$  s) under CCR operation and lower dc-link capacitance values.

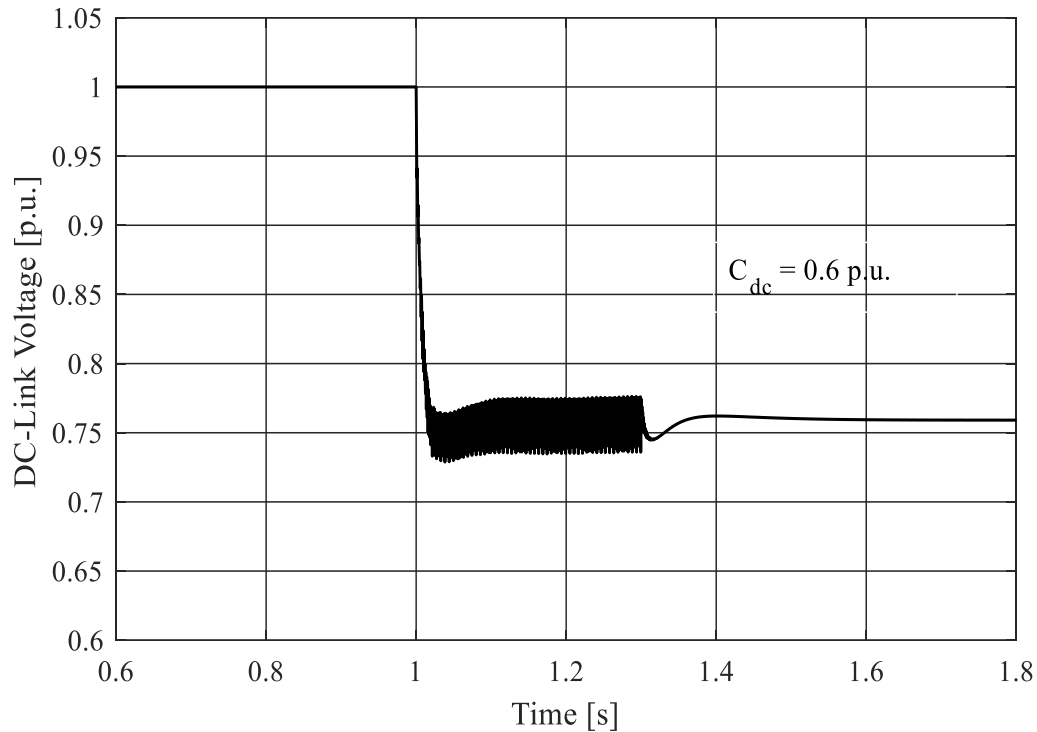


Figure 4.8: Influence of added active compensation loop at  $t = 1.3$ s. under CCR operation.

Figure 4.9 shows the compensated response at different dc-link voltage levels under all PV operation regions and different dc-link capacitance values. The system operates in the CVR, MPP, and CCR at  $t = 0 - 3$  s,  $t = 3 - 4$  s, and  $t = 4 - 7$  s, respectively.

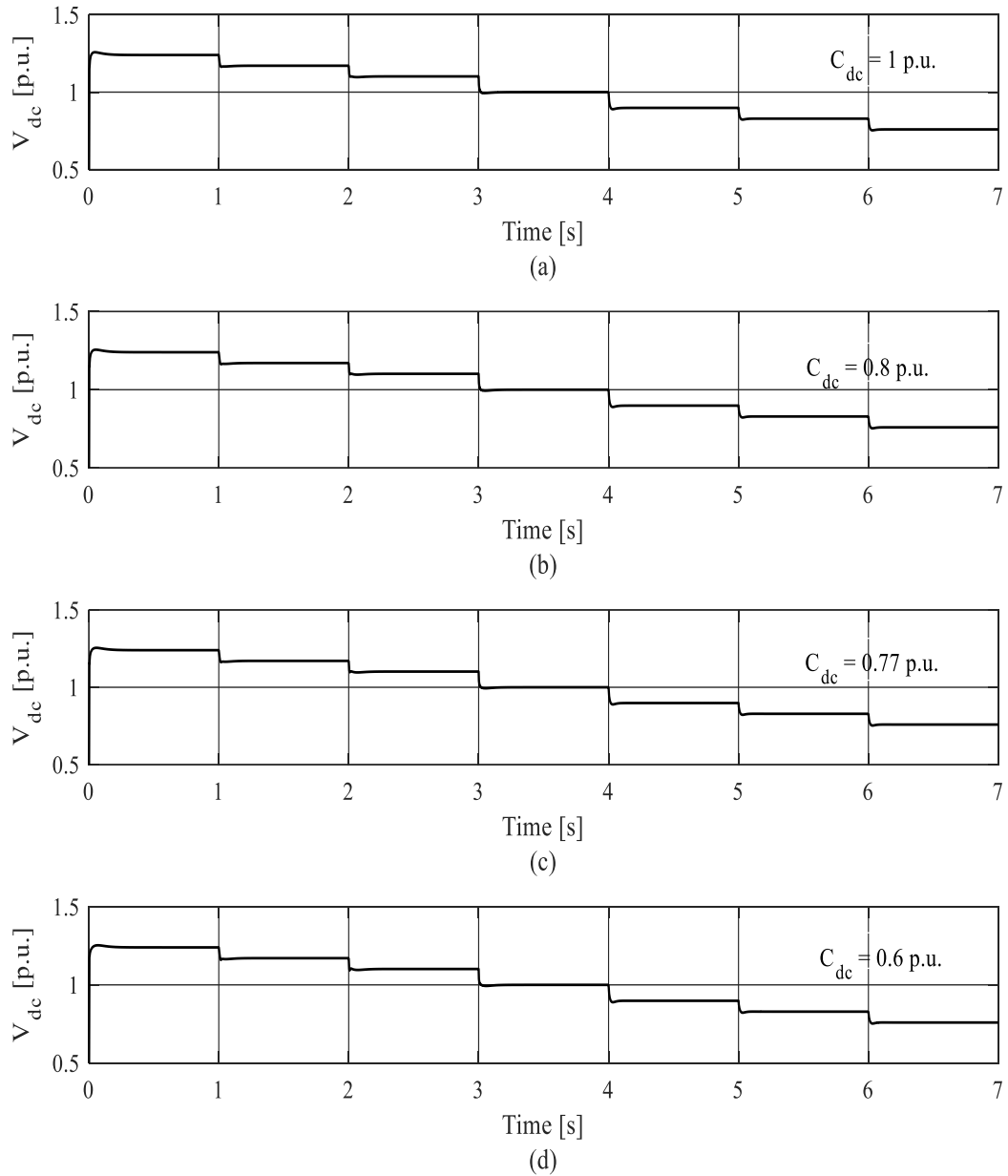


Figure 4.9: Uncompensated system response at different voltage levels and dc-link capacitance values.

#### 4.4.3 Influence of the DC-Link Cable

Figure 4.10 shows the dc-link voltage response of the uncompensated and compensated systems with no cables on the dc-side. It is clearly shown that the source of instabilities is not due to the

resonance at the dc-side, and they occur due to interactions between the dc-link capacitance and PV dynamic impedance.

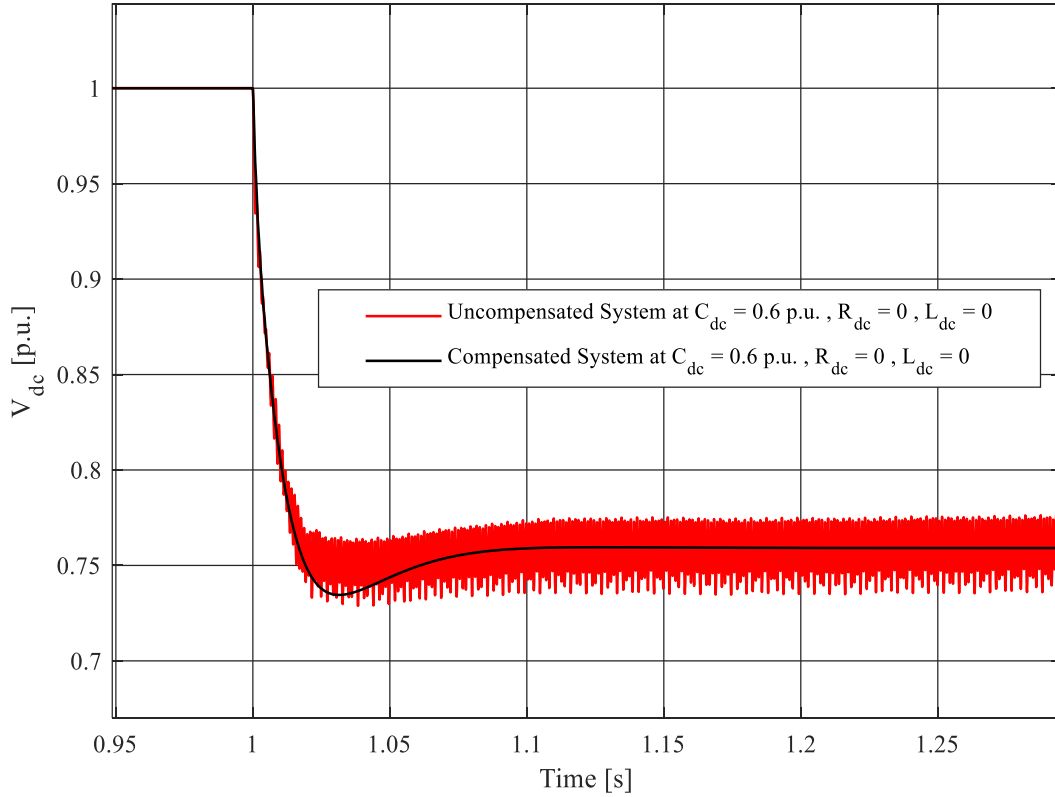


Figure 4.10: Compensated and uncompensated dc-link voltage responses at  $C_{dc} = 1$  p.u. due to dc cable influence.

#### 4.4.4 Operation Under Fault Conditions

Due to the increased penetration levels of renewable resources, the fault ride-through capability is incorporated to guarantee a stable grid operation during grid fault conditions.

Figure 4.11 investigates the low voltage ride-through capability of the compensated and uncompensated systems where the active compensator is applied under the CCR at  $t = 1$  s for the compensated system. The PCC is subjected to a single-line to ground fault for five cycles at  $t = 1.5$  s. Clearly, the system stability is preserved with the proposed compensator.

Figure 4.12 shows the compensated dc-link voltage response under different dc-link capacitance values. The system operates in the CCR and is subjected to a single-line to ground fault for five cycles at  $t = 4.5$  s.

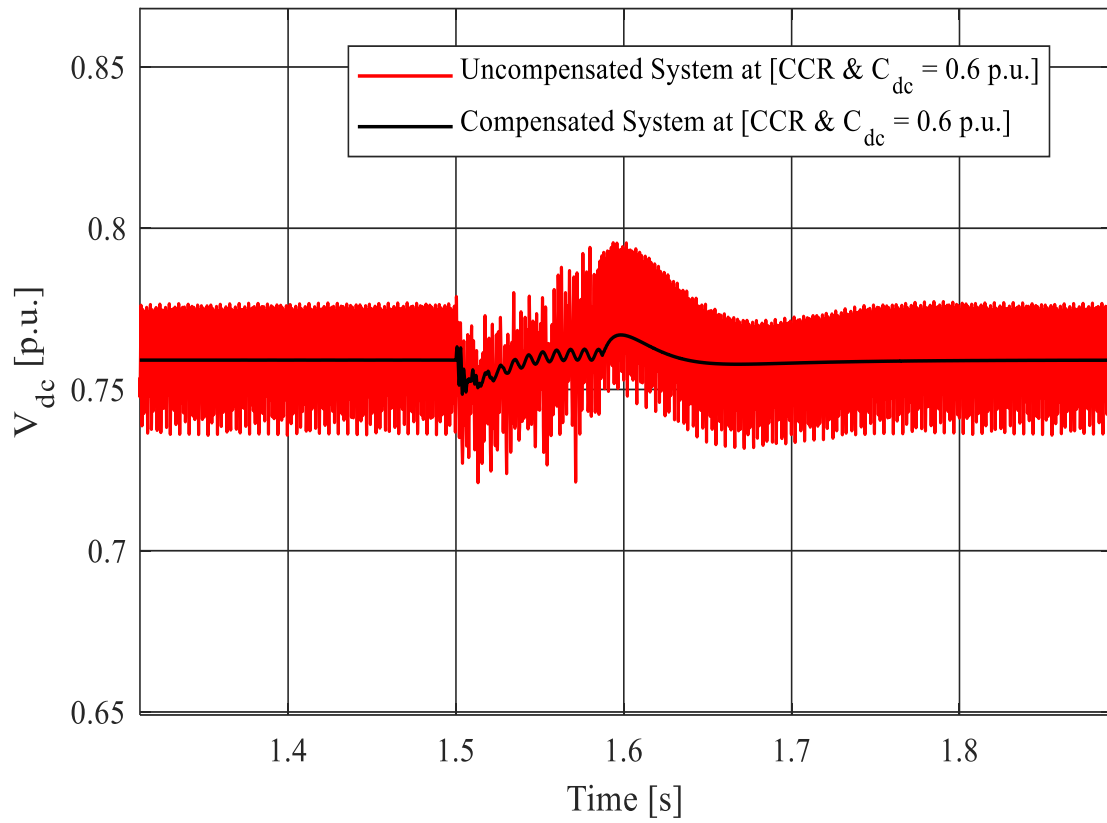


Figure 4.11: Compensated and uncompensated dc-link voltage response to a single-phase ground fault at  $t=1.5$ s for 5 cycles.

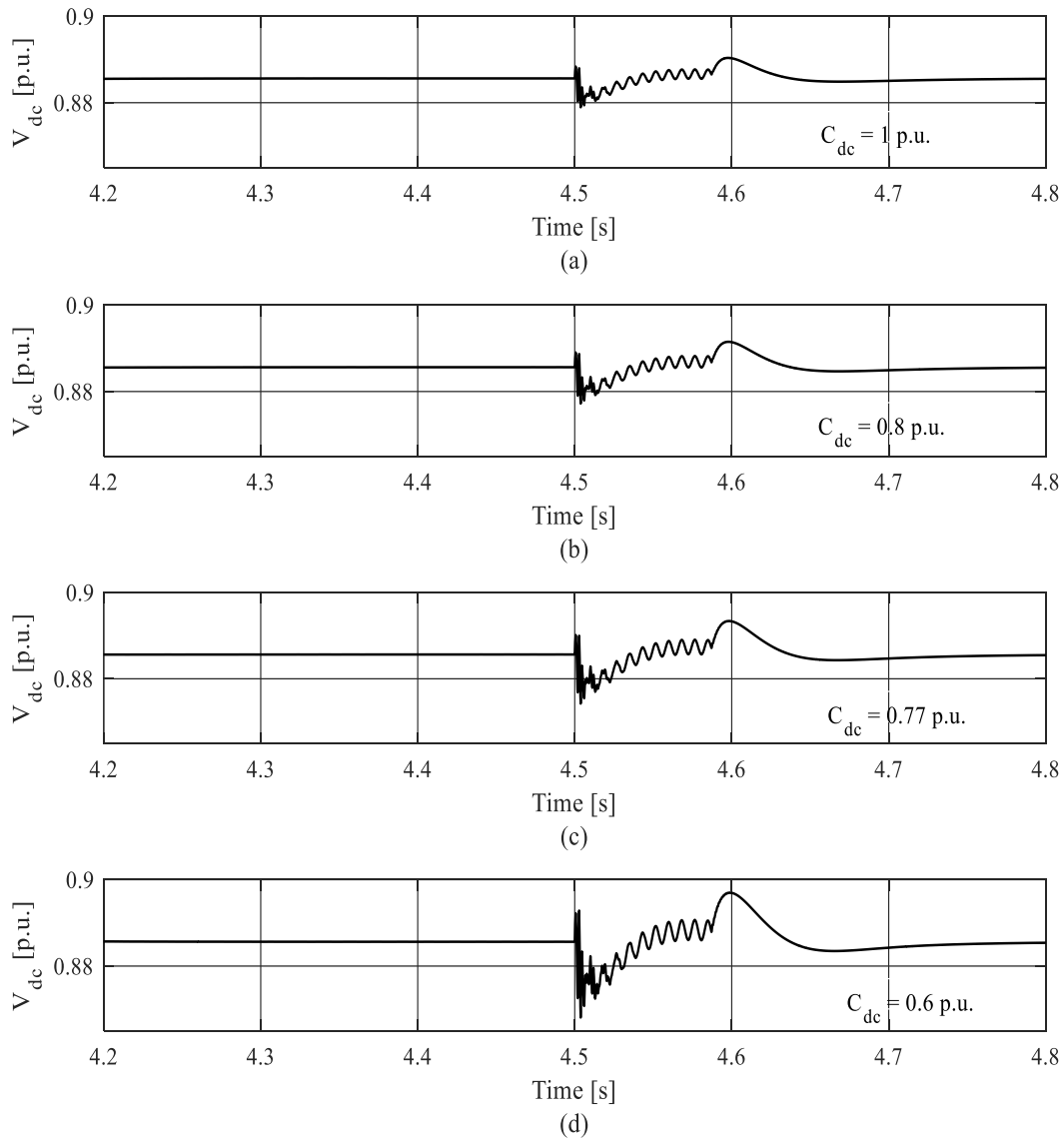


Figure 4.12: Compensated dc-link voltage response to a single-phase ground fault at  $t=4.5$ s for 5 cycles.

#### 4.4.5 Uncertainties in DC-Link Capacitance

As shown in Figure 4.13, the dc-link capacitance could vary by  $\pm 10\%$  to  $\pm 20\%$  from the nominal value due to aging, temperature, internal faults, etc. Due to parameter uncertainties, the system stability should be studied to ensure robust operating at different operating points and with reduced capacitance.

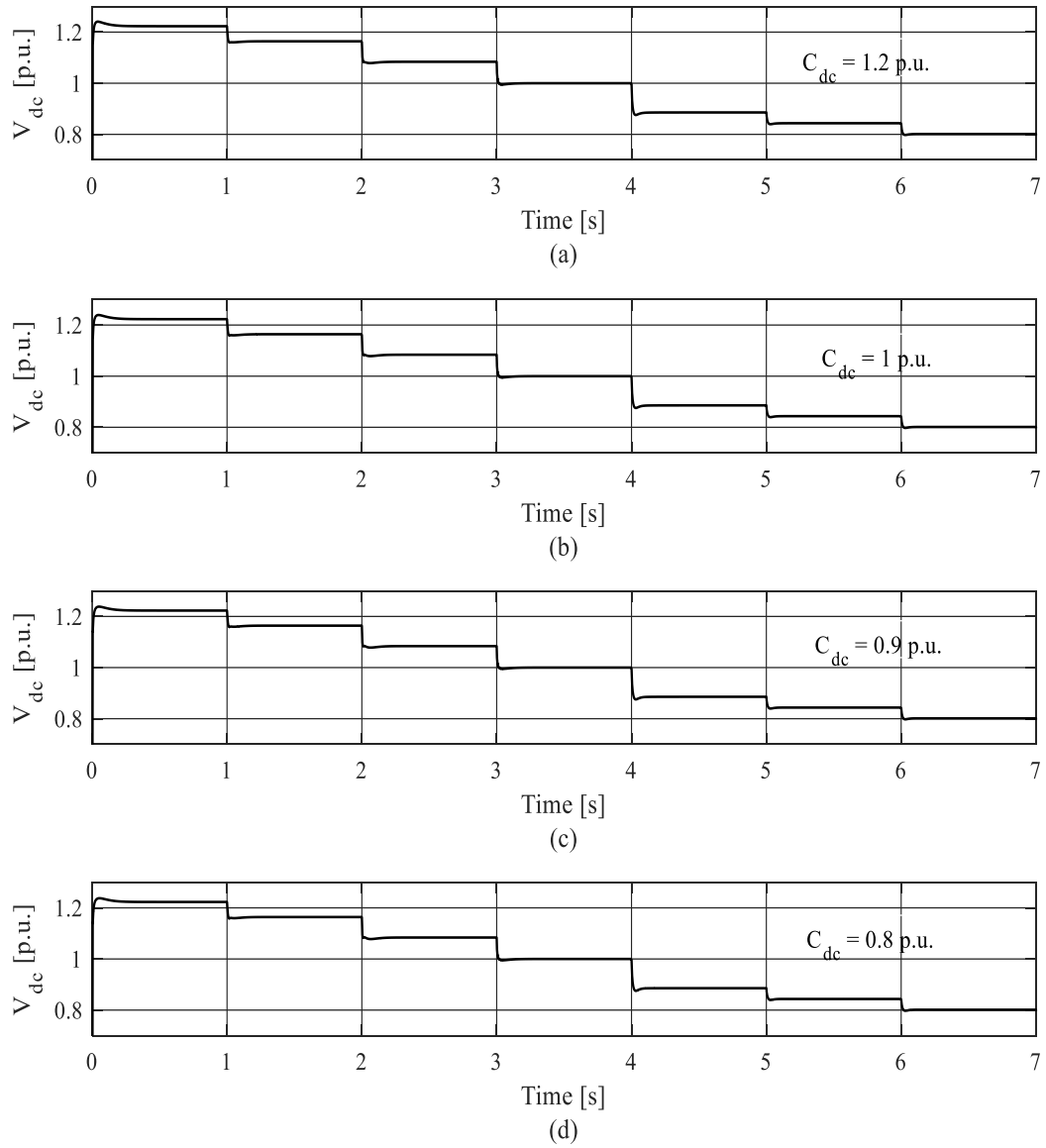


Figure 4.13: Uncompensated system for  $\pm 20\%$  dc-link capacitance values due to aging.

#### 4.4.6 Sensitivity Results

The influence of the proposed compensator on the dynamic and steady-state performance of the grid-connected VSC is investigated in this subsection. A unit step has been applied to the dc-link voltage at  $t = 1$  s, and the corresponding compensated versus uncompensated responses are

shown in Figure 4.14. It is clear that both responses have the same steady-state performance and share a similar rise time. Further, the ac-filter resonance is enhanced in the compensated system.

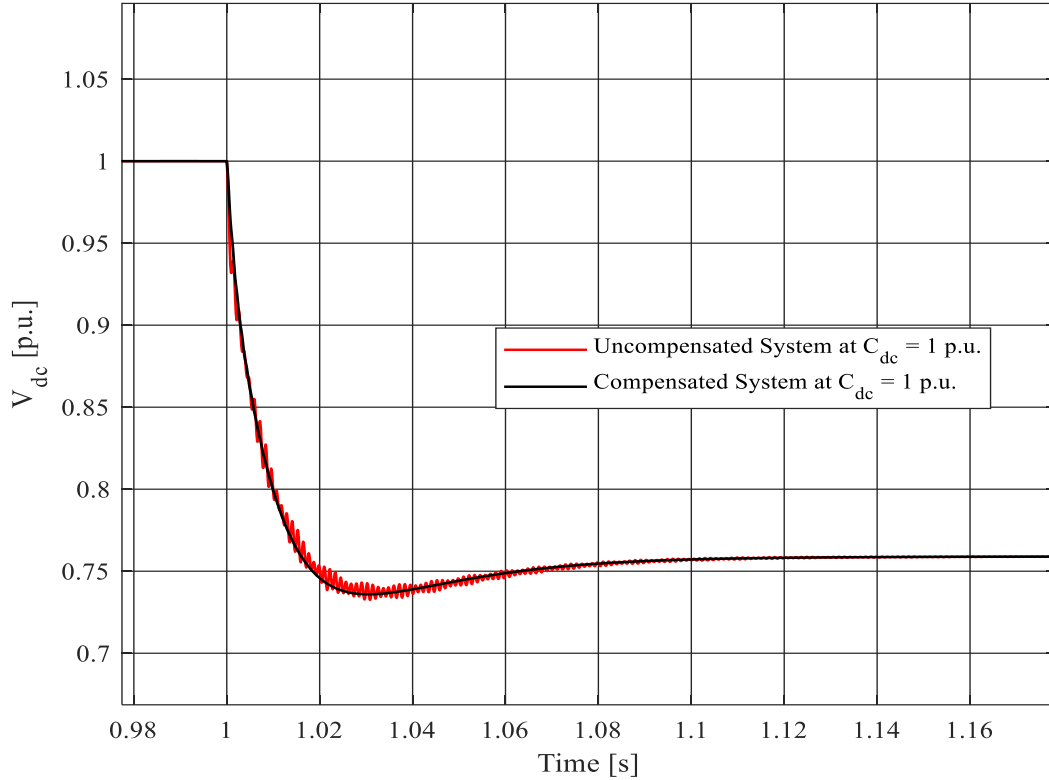


Figure 4.14: Compensated and uncompensated dc-link voltage responses at  $C_{dc} = 1$  p.u.

## 4.5 Conclusion

This chapter has shown that a reduced dc-link capacitance affects the dynamic stability of the overall system due to interactions with the dynamic resistance of the PV array. As a result, a new simple compensator is proposed to stabilize the system with a reduced dc-link capacitance. Small-signal stability analysis of the overall system is performed under different operating conditions. The proposed compensators have the following advantages: 1) it is simple yet effective and can be easily designed using linear analysis tools, 2) it does not affect the steady-state operation of the VSC grid-connected PV system, 3) it improves the damping performance of the dc-link voltage and provides a robust and stable performance at different operating conditions of the PV system, and 4) it facilitates successful low voltage ride-through at different operating conditions.

# Chapter 5

## Conclusions and Future Work

### 5.1 Conclusions

This thesis has addressed the integration of PV-VSCs systems to the utility grid using a reduced dc-link capacitance. First, the controllers' parameters have been accurately designed to preserve the system stability under a wide variation range of operating points. Then, small-signal analysis tools have been utilized to derive the equivalent incremental impedance models of the PV array and the interfacing VSC with reduced dc-link capacitance. Moreover, a new, simple, and active compensation method has been proposed to enhance the system performance by mitigating the dynamic instabilities. The compensated system is robustly damped and stabilized under different operating conditions. Time-domain nonlinear simulations are presented to validate the analytical results at different operating conditions. Furthermore, the large-signal LVRT performance has been investigated for both compensated and uncompensated systems. The compensated system reflects better damping following fault incidents.

The proposed compensator features the following advantages: 1) it is linear and so can be designed easily using linear analysis tools such as root locus and Bode plots. 2) it is a low order compensator, and so it should not overload digital controllers once implemented. 3) no extra voltage or current sensors are needed for implementation. 4) it does not affect the steady-state performance.

## 5.2 Future Work

In continuation of this work, the following research directions are suggested for future studies.

- 1) Investigating the dynamic stability of the proposed system under different partial shading cases. Also, studying the partial shading effect on the PV dynamic impedance and the overall system stability under different operating conditions.
- 2) Extending the PV circuit model to include other different types of the PV model (such as two- and three-diode models). Also, considering other components in the PV circuit model (such as resistance and inductance of the internal lines, diffusion capacitance, and dynamic impedance of the bypass and blocking diodes in the partial shading cases).
- 3) Deriving an accurate formula to calculate the minimum dc-link capacitance, which is required to stabilize the system performance under all operating conditions.
- 4) Investigating the dynamic interference between grid-connected VSC system and hybrid DG units.

## Bibliography

- [1] International Renewable Energy Agency. (2019, March). Renewable Capacity Statistics [Online]. Available: [https://www.irena.org/-/media/Files/IRENA/Agency/Publication/2019/Mar/RE\\_capacity\\_highlights\\_2019.pdf](https://www.irena.org/-/media/Files/IRENA/Agency/Publication/2019/Mar/RE_capacity_highlights_2019.pdf).
- [2] B. Karanayil, V. G. Agelidis, and J. Pou, “Performance evaluation of three-phase grid-connected photovoltaic inverters using electrolytic or polypropylene film capacitors,” *IEEE Trans. Sustain. Energy*, vol. 5, no. 4, pp. 1297–1306, Oct. 2014.
- [3] F. Blaabjerg, Z. Chen, and S. B. Kjaer, “Power electronics as efficient interface in dispersed power generation systems,” *IEEE Trans. Power Electron.*, vol. 19, no. 5, pp. 1184–1194, Sep. 2004.
- [4] A. Yazdani *et al.*, “Modeling guidelines and a benchmark for power system simulation studies of three-phase single-stage photovoltaic systems,” *IEEE Trans. Power Deliv.*, vol. 26, no. 2, pp. 1247–1264, Apr. 2011.
- [5] H. Wang and F. Blaabjerg, “Reliability of capacitors for DC-link applications in power electronic converters—An overview,” in *IEEE Trans. Ind. Appl.*, vol. 50, no. 5, pp. 3569–3578, Sep. 2014.
- [6] Y. Shi, R. Li, Y. Xue, and H. Li, “High-frequency-link-based grid-tied PV system with small DC-link capacitor and low-frequency ripple-free maximum power point tracking,” *IEEE Trans. Power Electron.*, vol. 31, no. 1, pp. 328–339, Jan. 2016.
- [7] N. Roux and F. Richardeau, “Stability of DC link with reduced energy storage for regenerative synchronous drive—Analytical approach,” in *Proc. Eur. Conf. Power Electron. Appl.*, 2007, pp. 1–10.
- [8] A. Yazdani and R. Iravani, *Voltage-sourced converters in power systems: modeling, control, and applications*, New Jersey: John Wiley & Sons, 2010.
- [9] J. R. Espinoza, G. Joós, M. Pérez, and T. L. A. Morán, “Stability issues in three-phase PWM current/voltage source rectifiers in the regeneration mode,” in *IEEE Proc. Symp. Ind. Electron.*, 2000, vol. 2, pp. 453–458.
- [10] J. M. Espí and J. Castelló, “Wind turbine generation system with optimized DC-link design and control,” *IEEE Trans. Ind. Electron.*, vol. 60, no. 3, pp. 919–929, Mar. 2013.
- [11] T. Messo, J. Jokipii, J. Puukko, and T. Suntio, “Determining the value of DC-link capacitance to ensure stable operation of a three-phase photovoltaic inverter,” *IEEE Trans. Power Electron.*, vol. 29, no. 2, pp. 665–673, Feb. 2014.
- [12] J. M. Carrasco *et al.*, “Power-electronic systems for the grid integration of renewable energy sources: A survey,” *IEEE Trans. Ind. Electron.*, vol. 53, no. 4, pp. 1002–1016, Aug. 2006.
- [13] L. Zhang, K. Sun, Y. Xing, L. Feng, and H. Ge, “A modular grid-connected photovoltaic generation

- system based on DC bus,” *IEEE Trans. Power Electron.*, vol. 26, no. 2, pp. 523–531, Feb. 2011.
- [14] B. Sahan, S. V. Araújo, C. Nöding, and P. Zacharias, “Comparative evaluation of three-phase current source inverters for grid interfacing of distributed and renewable energy systems,” *IEEE Trans. Power Electron.*, vol. 26, no. 8, pp. 2304–2318, Aug. 2011.
- [15] E. P. Wiechmann, P. Aqueveque, R. Burgos, and J. Rodriguez, “On the efficiency of voltage source and current source inverters for high-power drives,” *IEEE Trans. Ind. Electron.*, vol. 55, no. 4, pp. 1771–1782, Apr. 2008.
- [16] A. Kavimandan and S. P. Das, “Control and protection strategy for a three-phase single-stage boost type grid-connected current source inverter for PV applications,” in *Proc. IEEE Ind. Tech. Int. Conf.*, 2013, pp. 1722–1727.
- [17] International Energy Agency. (2019, October). “Renewables 2019 – Analysis and forecast to 2024.” [Online]. Available: <https://www.iea.org/reports/renewables-2019>.
- [18] *IEEE Recommended Criteria for Terrestrial Photovoltaic Power Systems, ANSI/IEEE Std. 928-1986*.
- [19] F. Katiraei and J. R. Agüero, “Solar PV integration challenges,” *IEEE Power Energy Mag.*, vol. 9, no. 3, pp. 62–71, May/Jun. 2011.
- [20] S. Mishra, D. Ramasubramanian, and P. C. Sekhar, “A seamless control methodology for a grid connected and isolated PV-diesel microgrid,” *IEEE Trans. Power Syst.*, vol. 28, no. 4, pp. 4393–4404, Nov. 2013.
- [21] Y. Wang, “THIN-FILM TRENCH CAPACITORS FOR SILICON AND ORGANIC PACKAGES,” M.Sc. thesis, School of Materials Science and Engineering, Georgia Institute of Technology, Atlanta, Georgia, United States, 2011.
- [22] J. Ho, T. R. Jow, and S. Boggs, “Historical introduction to capacitor technology,” *IEEE Electr. Insul. Mag.*, vol. 26, no. 1, pp. 20–25, Jan./Feb. 2010.
- [23] R. U. A. Shaikh, A. Saeed, and R. Kumar, “Review on present and future integration techniques for capacitors in motor drives,” in *2018 International Conference on Computing, Mathematics and Engineering Technologies (iCoMET)*, 2018, pp. 1–8.
- [24] M. S. Bilgin, G. Poyrazoglu, M. Aktem, and E. Er, “Comparison of DC-link capacitor types under various grid conditions,” in *Proceedings - 2019 IEEE 13th International Conference on Compatibility, Power Electronics and Power Engineering (CPE-POWERENG)*, 2019.
- [25] F. Deng *et al.*, “Capacitor ESR and C Monitoring in Modular Multilevel Converters,” *IEEE Trans. Power Electron.*, vol. 35, no. 4, pp. 4063–4075, Apr. 2020.
- [26] M. L. Gasperi, “Life prediction modeling of bus capacitors in AC variable-frequency drives,” *IEEE Trans. Ind. Appl.*, vol. 41, no. 6, pp. 1430–1435, Nov./Dec. 2005.

- [27] H. Soliman, H. Wang, and F. Blaabjerg, “A Review of the Condition Monitoring of Capacitors in Power Electronic Converters,” *IEEE Trans. Ind. Appl.*, vol. 52, no. 6, pp. 4976–4989, Nov. 2016.
- [28] H. Wang, P. Davari, H. Wang, D. Kumar, F. Zare, and F. Blaabjerg, “Lifetime Estimation of DC-Link Capacitors in Adjustable Speed Drives under Grid Voltage Unbalances,” in *IEEE Trans. Power Electron.*, vol. 34, no. 5, pp. 4064–4078, May 2019.
- [29] N. Agarwal, M. W. Ahmad, and S. Anand, “Quasi-Online Technique for Health Monitoring of Capacitor in Single-Phase Solar Inverter,” *IEEE Trans. Power Electron.*, vol. 33, no. 6, pp. 5283–5291, Jun. 2018.
- [30] T. Mannen and H. Fujita, “A DC capacitor voltage control method for active power filters using modified reference including the theoretically derived voltage ripple,” *IEEE Trans. Ind. Appl.*, vol. 52, no. 5, pp. 4179–4187, Sep./Oct. 2016.
- [31] G. M. Soares, J. M. Alonso, and H. A. C. Braga, “Investigation of the Active Ripple Compensation Technique to Reduce Bulk Capacitance in Offline Flyback-Based LED Drivers,” *IEEE Trans. Power Electron.*, vol. 33, no. 6, pp. 5206–5214, Jun. 2018.
- [32] A. Mutovkin, V. Yuhimenko, M. Mellincovsky, S. Schacham, and A. Kuperman, “Control of Direct Voltage Regulated Active DC-Link Capacitance Reduction Circuits to Allow Plug-and-Play Operation,” *IEEE Trans. Ind. Electron.*, vol. 66, no. 8, pp. 6527–6537, Aug. 2019.
- [33] H. Wang, H. Wang, G. Zhu, and F. Blaabjerg, “An Overview of Capacitive DC-Links-Topology Derivation and Scalability Analysis,” *IEEE Trans. Power Electron.*, vol. 35, no. 2, pp. 1805–1829, Feb. 2020.
- [34] H. V. Nguyen and D. C. Lee, “Reducing the dc-link capacitance: A bridgeless PFC boost rectifier that reduces the second-order power ripple at the dc output,” *IEEE Ind. Appl. Mag.*, vol. 24, no. 2, pp. 2–13, Mar. 2018.
- [35] J. H. R. Enslin and P. J. M. Heskes, “Harmonic interaction between a large number of distributed power inverters and the distribution network,” in *Proc. PESC’03 Conf.*, 2003, vol. 4, pp. 1742–1747.
- [36] X. Wang, F. Blaabjerg, and W. Wu, “Modeling and analysis of harmonic stability in an AC power-electronics-based power system,” *IEEE Trans. Power Electron.*, vol. 29, no. 12, pp. 6421–6432, Dec. 2014.
- [37] M. Liserre, R. Teodorescu, and F. Blaabjerg, “Stability of photovoltaic and wind turbine grid-connected inverters for a large set of grid impedance values,” *IEEE Trans. Power Electron.*, vol. 21, no. 1, pp. 263–272, Jan. 2006.
- [38] E. Figueres, G. Garcerá, J. Sandia, F. González-Espín, and J. C. Rubio, “Sensitivity study of the dynamics of three-phase photovoltaic inverters with an LCL grid filter,” *IEEE Trans. Ind. Electron.*,

- vol. 56, no. 3, pp. 706–717, Mar. 2009.
- [39] M. Hanif, V. Khadkikar, W. Xiao, and J. L. Kirtley, “Two degrees of freedom active damping technique for LCL filter-based grid connected PV Systems,” *IEEE Trans. Ind. Electron.*, vol. 61, no. 6, pp. 2795–2803, Jun. 2014.
- [40] Y. Huang, X. Yuan, J. Hu, and P. Zhou, “Modeling of VSC Connected to Weak Grid for Stability Analysis of DC-Link Voltage Control,” *IEEE J. Emerg. Sel. Topics Power Electron.*, vol. 3, no. 4, pp. 1193–1204, Dec. 2015.
- [41] H. Yuan, X. Yuan, and J. Hu, “Modeling of Grid-Connected VSCs for Power System Small-Signal Stability Analysis in DC-Link Voltage Control Timescale,” *IEEE Trans. Power Syst.*, vol. 32, no. 5, pp. 3981–3991, Sep. 2017.
- [42] P. Zhou, X. Yuan, J. Hu, and Y. Huang, “Stability of DC-link voltage as affected by phase locked loop in VSC when attached to weak grid,” in *Proc. IEEE PES Gen. Meeting*, 2014, pp. 1–5.
- [43] D. Dong, J. Li, D. Boroyevich, P. Mattavelli, I. Cvetkovic, and Y. Xue, “Frequency behavior and its stability of grid-interface converter in distributed generation systems,” in *Proc. IEEE Appl. Power Electron. Conf. Expo.*, Feb. 2012, pp. 1887–1893.
- [44] V. Diedrichs, A. Beekmann, and S. Adloff, “Loss of (Angle) stability of wind power plants—The underestimated phenomenon in case of very low short circuit ratio,” in *Proc. 10th Int. Workshop Large-Scale Integr. Wind Power Power Syst. Transmiss. Netw. Offshore Wind Power Plants*, Aarhus, Denmark, Oct. 25–26, 2011, pp. 393–423.
- [45] Y. Huang and D. Wang, “Effect of Control-Loops Interactions on Power Stability Limits of VSC Integrated to AC System,” *IEEE Trans. Power Deliv.*, vol. 33, no. 1, pp. 301–310, Feb. 2018.
- [46] M. Salo and H. Tuusa, “A vector controlled current-source PWM rectifier with a novel current damping method,” *IEEE Trans. Power Electron.*, vol. 15, no. 3, pp. 464–470, May 2000.
- [47] F. Liu, B. Wu, N. R. Zargari, and M. Pande, “An active damping method using inductor-current feedback control for high-power PWM current-source rectifier,” *IEEE Trans. Power Electron.*, vol. 26, no. 9, pp. 2580–2587, Sep. 2011.
- [48] J. C. Wiseman and B. Wu, “Active damping control of a high-power PWM current-source rectifier for line-current THD reduction,” *IEEE Trans. Ind. Electron.*, vol. 52, no. 3, pp. 758–764, Jun. 2005.
- [49] P. P. Dash and M. Kazerani, “Harmonic elimination in a multilevel Current-Source Inverter-based grid-connected photovoltaic system,” in *Proc. IEEE Ind. Electron. Soc. Conf.*, 2012, pp. 1001–1006.
- [50] M. A. Mahmud, H. R. Pota, and M. J. Hossain, “Dynamic stability of three-phase grid-connected photovoltaic system using zero dynamic design approach,” *IEEE J. Photovoltaics*, vol. 2, no. 4, pp. 564–571, Oct. 2012.
- [51] A. Yazdani and P. P. Dash, “A control methodology and characterization of dynamics for a

- photovoltaic (PV) system interfaced with a distribution network,” *IEEE Trans. Power Deliv.*, vol. 24, no. 3, pp. 1538–1551, Jul. 2009.
- [52] P. P. Dash and M. Kazerani, “Dynamic modeling and performance analysis of a grid-connected current-source inverter-based photovoltaic system,” *IEEE Trans. Sustain. Energy*, vol. 2, no. 4, pp. 443–450, Oct. 2011.
- [53] X. Feng, J. Liu, and F. C. Lee, “Impedance specifications for stable DC distributed power systems,” *IEEE Trans. Power Electron.*, vol. 17, no. 2, pp. 157–162, Mar. 2002.
- [54] J. Sun, “Impedance-based stability criterion for grid-connected inverters,” *IEEE Trans. Power Electron.*, vol. 26, no. 11, pp. 3075–3078, Nov. 2011.
- [55] J. M. Zhang, X. G. Xie, D. Z. Jiao, and Z. Qian, “Stability problems and input impedance improvement for cascaded power electronic systems,” in *Proc. IEEE Appl. Power Electron. Conf.*, 2004, pp. 1018–1024.
- [56] V. Konoval and R. Prytula, “Power system participation factors for real and complex eigenvalues cases,” *Pozn. Univ. Technol. Acad. Journals Electr. Eng.*, no. 90, pp. 369–381, Jan. 2017.
- [57] A. Radwan, “Modeling, analysis and stabilization of converter-dominated power distribution grids,” M.Sc. thesis, Dept. Electr. Comput. Eng., Univ. Alberta, Edmonton, AB, Canada, 2012.
- [58] I. J. Pérez-Arriaga, G. C. Verghese, and F. C. Schweppe, “Selective modal analysis with applications to electric power systems, part I: Heuristic introduction,” *IEEE Trans. Power Appar. Syst.*, vol. PAS-101, no. 9, pp. 3117–3125, Sep. 1982.
- [59] W. A. Hashlamoun, M. A. Hassouneh, and E. H. Abed, “New results on modal participation factors: Revealing a previously unknown dichotomy,” *IEEE Trans. Autom. Control*, vol. 54, no. 7, pp. 1439–1449, Jul. 2009.
- [60] A. A. A. Radwan and Y. A. R. I. Mohamed, “Grid-Connected Wind-Solar Cogeneration Using Back-to-Back Voltage-Source Converters,” *IEEE Trans. Sustain. Energy*, vol. 11, no. 1, pp. 315–325, Jan. 2020.
- [61] *PV-UDI90MF5*, Mitsubishi, San Francisco, CA, USA, 2007.
- [62] *ABB Solar Inverters, “PVS980,”* ABB, Zurich, Switzerland, 2018.
- [63] J. C. Wang *et al.*, “A novel method for the determination of dynamic resistance for photovoltaic modules,” *Energy*, vol. 36, no. 10, pp. 5968–5974, Oct. 2011.
- [64] L. Harnefors, M. Bongiorno, and S. Lundberg, “Input-admittance calculation and shaping for controlled voltage-source converters,” *IEEE Trans. Ind. Electron.*, vol. 54, no. 6, pp. 3323–3334, Dec. 2007.

# APPENDICES

## Appendix A.3

### A.3.1 Simulation System Parameters

The VSC grid-connected system parameters are:

*Utility-Grid:*  $v_g = 12.47 \text{ KV}$  ,  $\omega^o = 2\pi(60) \text{ rad/s}$  ,  $SCR = 20$  ,  $X/R = 10$ .

*Step-Up Transformer:*  $N = (0.48 \text{ KV}/12.47 \text{ KV})$  ,  $L_p = 122.23 \mu\text{H}$  ,  $R_p = 4.608 \text{ m}\Omega$  ,  $L_s = 27.499 \text{ mH}$  ,  $R_s = 1.0367 \Omega$ .

*AC-Filter and VSC Controllers:*  $P = 1.5 \text{ MW}$  ,  $f_{sw} = 51 * (60 \text{ Hz})$  ,  $L_f = 100 \mu\text{H}$  ,  $R_f = 2 \text{ m}\Omega$  ,  $r_{on} = 1 \text{ m}\Omega$  ,  $C_f = 369 \mu\text{F}$  ,  $k_p^{pll} = 1.8014e2 \text{ V}^{-1}\text{s}^{-1}$  ,  $k_i^{pll} = 3.1969e3 \text{ V}^{-1}\text{s}^{-2}$  ,  $k_p^i = 0.1923 \Omega$  ,  $k_i^i = 3.8453 \Omega\text{s}^{-1}$  ,  $k_p^{vac} = 0.4807 \Omega^{-1}$  ,  $k_i^{vac} = 9.2415 \Omega^{-1}\text{s}^{-1}$  ,  $k_p^{vac} = 71.8162 \text{ VarV}^{-1}$  ,  $k_i^{vac} = 1.9947e6 \text{ VarV}^{-1}\text{s}^{-1}$ .

*DC-Link:*  $C_{dc} = 5000 \mu\text{F}$ .

*DC-Cable:*  $L_{dc} = 0.34 \mu\text{H}$  ,  $R_{dc} = 0.125 \text{ m}\Omega$ .

The PV module parameters of a model “Mitsubishi Electric PV-UD190MF5” are:

Table A.3.1: Solar module parameters.

<b>Parameters</b>	<b>Description</b>	<b>Values</b>
$I_{irr}^*$	<i>PV module nominal illumination</i>	$1 \text{ KW}/\text{m}^2$
$T^*$	<i>PV module nominal temperature</i>	$298 \text{ Kelvin}$
$R_s$	<i>Series resistance of a PV module</i>	$0.32376 \Omega$
$R_{sh}$	<i>Shunt resistance of a PV module</i>	$236.4479 \Omega$
$n_s$	<i>Number of series-connected cells in a PV module</i>	$50$
$I_{ph}$	<i>PV module Light generated current</i>	$8.2413 \text{ A}$
$I_{sc}$	<i>PV module short circuit current</i>	$8.23 \text{ A}$
$V_{oc}$	<i>PV module open circuit voltage</i>	$30.8 \text{ V}$

$I_{max}$	<i>PV module maximum current</i>	7.71 A
$V_{max}$	<i>PV module maximum voltage</i>	24.7 V
$P_{max}$	<i>PV module maximum power</i>	190.437 W
$I_{rs}^*$	<i>PV module reference reverse saturation current</i>	$7.6985E - 11$ A
$k$	<i>Boltzmann constant</i>	$1.3806E - 23$ Joules/Kelvin
$q$	<i>Electron charge</i>	$1.6022E - 19$ Coulomb
$V_T$	<i>Thermal voltage (KT/q)</i>	
$A$	<i>Ideality factor</i>	0.94466
$E_g$	<i>Bandgap energy for silicon</i>	1.1 eV
$\alpha_i$	<i>Short-circuit current temperature coefficient</i>	0.038202 %/°C
$\alpha_v$	<i>Open-circuit voltage temperature coefficient</i>	-0.32571 %/°C

### A.3.2 Linearized State-Space Equations

Using the same symbols of Figure 3.1 and Figure 3.7, the linearization of the non-linear equations in section 3.2 and section 3.3 is given as follows:

**Equ (3.14)** Linearized Equation of the VSC AC-Filter

$$\begin{bmatrix} \Delta i_d^g \\ \Delta i_q^g \end{bmatrix} = \overbrace{\begin{bmatrix} -R_f & \omega^o \\ L_f & -R_f \end{bmatrix}}^{A_1} \begin{bmatrix} \Delta i_d^g \\ \Delta i_q^g \end{bmatrix} + \overbrace{\begin{bmatrix} 1 & 0 \\ 0 & 1 \end{bmatrix}}^{B_1} \begin{bmatrix} \Delta v_{id}^g \\ \Delta v_{iq}^g \end{bmatrix} + \overbrace{\begin{bmatrix} -1 & 0 \\ 0 & -1 \end{bmatrix}}^{-B_1} \begin{bmatrix} \Delta v_d^g \\ \Delta v_q^g \end{bmatrix} + \overbrace{\begin{bmatrix} i_q^o \\ -i_d^o \end{bmatrix}}^{C_1} [\Delta \omega^g]$$

**Equ (3.15)** Linearized Equation of Step-Up Transformer and Grid Impedance

$$\begin{bmatrix} \Delta i_{gd}^g \\ \Delta i_{gq}^g \end{bmatrix} = \overbrace{\begin{bmatrix} -R_T & \omega^o \\ L_T & -R_T \end{bmatrix}}^{A_2} \begin{bmatrix} \Delta i_{gd}^g \\ \Delta i_{gq}^g \end{bmatrix} + \frac{1}{N} \overbrace{\begin{bmatrix} 1 & 0 \\ 0 & 1 \end{bmatrix}}^{B_2} \begin{bmatrix} \Delta v_d^g \\ \Delta v_q^g \end{bmatrix} + \overbrace{\begin{bmatrix} -1 & 0 \\ 0 & -1 \end{bmatrix}}^{-B_2} \begin{bmatrix} \Delta v_{gd}^g \\ \Delta v_{gq}^g \end{bmatrix} + \overbrace{\begin{bmatrix} i_{gq}^o \\ -i_{gd}^o \end{bmatrix}}^{C_2} [\Delta \omega^g]$$

**Equ (3.16)** Linearized Equation of the Capacitor at the Point of Common Coupling

$$\begin{bmatrix} \Delta \dot{v}_d^g \\ \Delta \dot{v}_q^g \end{bmatrix} = \overbrace{\begin{bmatrix} 0 & \omega^o \\ -\omega^o & 0 \end{bmatrix}}^{A_3} \begin{bmatrix} \Delta v_d^g \\ \Delta v_q^g \end{bmatrix} + \overbrace{\begin{bmatrix} \frac{1}{C_f} & 0 \\ 0 & \frac{1}{C_f} \end{bmatrix}}^{B_3} \begin{bmatrix} \Delta i_d^g \\ \Delta i_q^g \end{bmatrix} + \frac{1}{N} \overbrace{\begin{bmatrix} -1 & 0 \\ 0 & -1 \end{bmatrix}}^{-B_3} \begin{bmatrix} \Delta i_{gd}^g \\ \Delta i_{gq}^g \end{bmatrix} + \overbrace{\begin{bmatrix} v_q^o \\ -v_d^o \end{bmatrix}}^{C_3} [\Delta \omega^g]$$

**Equ (3.30)** Linearized Equations of the VSC Current Controller

$$\begin{bmatrix} \Delta v_{id}^c \\ \Delta v_{iq}^c \end{bmatrix} = \overbrace{\begin{bmatrix} 0 & -\omega^o L_f \\ \omega^o L_f & 0 \end{bmatrix}}^{A_4} \begin{bmatrix} \Delta i_d^c \\ \Delta i_q^c \end{bmatrix} + \begin{bmatrix} \Delta \varphi_d^i \\ \Delta \varphi_q^i \end{bmatrix} + \begin{bmatrix} \Delta v_d^c \\ \Delta v_q^c \end{bmatrix} + \underbrace{\begin{bmatrix} k_p^i & 0 \\ 0 & k_p^i \end{bmatrix}}_{B_4} \begin{bmatrix} \Delta i_d^* \\ \Delta i_q^* \end{bmatrix} + \underbrace{\begin{bmatrix} -k_p^i & 0 \\ 0 & -k_p^i \end{bmatrix}}^{-B_4} \begin{bmatrix} \Delta i_d^c \\ \Delta i_q^c \end{bmatrix} \\ + \underbrace{\begin{bmatrix} -L_f i_q^o \\ L_f i_d^o \end{bmatrix}}_{C_4} [\Delta \omega^c]$$

$$\begin{bmatrix} \Delta \dot{\varphi}_d^i \\ \Delta \dot{\varphi}_q^i \end{bmatrix} = \overbrace{\begin{bmatrix} k_i^i & 0 \\ 0 & k_i^i \end{bmatrix}}^{A_5} \begin{bmatrix} \Delta i_d^* \\ \Delta i_q^* \end{bmatrix} + \overbrace{\begin{bmatrix} -k_i^i & 0 \\ 0 & -k_i^i \end{bmatrix}}^{-A_5} \begin{bmatrix} \Delta i_d^c \\ \Delta i_q^c \end{bmatrix}$$

**Equ (3.25) and Equ (3.26)** Linearized Equations of the Phase-Locked Loop

$$\begin{bmatrix} \Delta \dot{\varepsilon} \\ \Delta \dot{\varphi}_\varepsilon^{pll} \end{bmatrix} = \overbrace{\begin{bmatrix} 0 & 1 \\ 0 & 0 \end{bmatrix}}^{A_6} \begin{bmatrix} \Delta \varepsilon \\ \Delta \varphi_\varepsilon^{pll} \end{bmatrix} + \overbrace{\begin{bmatrix} 0 & \frac{k_p^{pll}}{v_d^o} \\ 0 & \frac{k_i^{pll}}{v_d^o} \end{bmatrix}}^{B_6} \begin{bmatrix} \Delta v_d^c \\ \Delta v_q^c \end{bmatrix} \\ \Delta \omega = \overbrace{\begin{bmatrix} 0 & 1 \end{bmatrix}}^{C_6} \begin{bmatrix} \Delta \varepsilon \\ \Delta \varphi_\varepsilon^{pll} \end{bmatrix} + \overbrace{\begin{bmatrix} 0 & \frac{k_p^{pll}}{v_d^o} \end{bmatrix}}^{D_6} \begin{bmatrix} \Delta v_d^c \\ \Delta v_q^c \end{bmatrix}$$

**Equ (3.27a), Equ(3.27b), and Equ(3.27c)** Linearized Equations of the Reference-Frame Transformation where synchronization angle is very small ( $\varepsilon \ll 1$ )

$$\begin{bmatrix} \Delta v_d^c \\ \Delta v_q^c \end{bmatrix} = \begin{bmatrix} \Delta v_d^g \\ \Delta v_q^g \end{bmatrix} + \overbrace{\begin{bmatrix} v_q^o & 0 \\ -v_d^o & 0 \end{bmatrix}}^{A_7} \begin{bmatrix} \Delta \varepsilon \\ \Delta \varphi_\varepsilon^{pll} \end{bmatrix} \\ \begin{bmatrix} \Delta i_d^c \\ \Delta i_q^c \end{bmatrix} = \begin{bmatrix} \Delta i_d^g \\ \Delta i_q^g \end{bmatrix} + \overbrace{\begin{bmatrix} i_q^o & 0 \\ -i_d^o & 0 \end{bmatrix}}^{B_7} \begin{bmatrix} \Delta \varepsilon \\ \Delta \varphi_\varepsilon^{pll} \end{bmatrix}$$

$$\begin{bmatrix} \Delta v_{id}^g \\ \Delta v_{iq}^g \end{bmatrix} = \begin{bmatrix} \Delta v_{id}^c \\ \Delta v_{iq}^c \end{bmatrix} + \overbrace{\begin{bmatrix} -v_{iq}^o & 0 \\ v_{id}^o & 0 \end{bmatrix}}^{C_7} \begin{bmatrix} \Delta \varepsilon \\ \Delta \varphi_\varepsilon^{pll} \end{bmatrix}$$

**Equ (3.38)** Linearized Equation of Integrator Term of the AC-Voltage Controller

$$\Delta \dot{\varphi}_v^{ac} = \overbrace{\begin{bmatrix} -k_i^{vac} & 0 \end{bmatrix}}^{A_8} \begin{bmatrix} \Delta v_d^c \\ \Delta v_q^c \end{bmatrix} + \overbrace{\begin{bmatrix} k_i^{vac} \end{bmatrix}}^{B_8} \Delta v_d^*$$

**Equ (3.19a) and Equ (3.33)** DC-Link Dynamic Linearized Equation of the Accurate System

$$\begin{aligned} \begin{bmatrix} \Delta \dot{V}_{dc}^2 \\ \Delta \dot{\varphi}_v^{dc} \end{bmatrix} &= \overbrace{\begin{bmatrix} I_{pv}^o & 0 \\ C_{dc} \sqrt{V_{dc}^2{}^o} & -k_i^{vdc} \end{bmatrix}}^{A_9} \begin{bmatrix} \Delta V_{dc}^2 \\ \Delta \varphi_v^{dc} \end{bmatrix} + \overbrace{\begin{bmatrix} 0 & 0 \\ k_i^{vdc} & 0 \end{bmatrix}}^{B_9} \begin{bmatrix} \Delta V_{dc}^2{}^* \\ \Delta P_{pv} \end{bmatrix} + \overbrace{\begin{bmatrix} -3v_{id}^o & -3v_{iq}^o \\ C_{dc} & C_{dc} \\ 0 & 0 \end{bmatrix}}^{C_9} \begin{bmatrix} \Delta i_d^g \\ \Delta i_q^g \end{bmatrix} \\ &+ \underbrace{\begin{bmatrix} -3i_d^o & -3i_q^o \\ C_{dc} & C_{dc} \\ 0 & 0 \end{bmatrix}}_{D_9} \begin{bmatrix} \Delta v_{id}^g \\ \Delta v_{iq}^g \end{bmatrix} + \underbrace{\begin{bmatrix} \left( \frac{2\sqrt{V_{dc}^2{}^o}}{C_{dc}} \right) \\ 0 \end{bmatrix}}_{E_9} \Delta I_{pv} \end{aligned}$$

**Equ (3.19b) and Equ (3.33)** DC-Link Dynamic Linearized Equation of the Accurate System

$$\begin{aligned} \begin{bmatrix} \Delta \dot{V}_{dc}^2 \\ \Delta \dot{\varphi}_v^{dc} \end{bmatrix} &= \overbrace{\begin{bmatrix} I_{pv}^o & 0 \\ C_{dc} \sqrt{V_{dc}^2{}^o} & -k_i^{vdc} \end{bmatrix}}^{A_9} \begin{bmatrix} \Delta V_{dc}^2 \\ \Delta \varphi_v^{dc} \end{bmatrix} + \overbrace{\begin{bmatrix} 0 & 0 \\ k_i^{vdc} & 0 \end{bmatrix}}^{B_9} \begin{bmatrix} \Delta V_{dc}^2{}^* \\ \Delta P_{pv} \end{bmatrix} \\ &+ \overbrace{\begin{bmatrix} -3v_d^o - 6R_f i_d^o & -3v_q^o - 6R_f i_q^o \\ C_{dc} & C_{dc} \\ 0 & 0 \end{bmatrix}}^{C_9} \begin{bmatrix} \Delta i_d^g \\ \Delta i_q^g \end{bmatrix} + \underbrace{\begin{bmatrix} -3i_d^o & -3i_q^o \\ C_{dc} & C_{dc} \\ 0 & 0 \end{bmatrix}}_{D_9} \begin{bmatrix} \Delta v_d^g \\ \Delta v_q^g \end{bmatrix} \\ &+ \underbrace{\begin{bmatrix} \left( \frac{2\sqrt{V_{dc}^2{}^o}}{C_{dc}} \right) \\ 0 \end{bmatrix}}_{E_9} \Delta I_{pv} + \overbrace{\begin{bmatrix} -3L_f i_d^o & -3L_f i_q^o \\ C_{dc} & C_{dc} \\ 0 & 0 \end{bmatrix}}^{F_9} \begin{bmatrix} \Delta i_d^g \\ \Delta i_q^g \end{bmatrix} \end{aligned}$$

**Equ (3.19c) and Equ (3.33)** DC-Link Dynamic Linearized Equation of the Approximated System

$$\begin{aligned} \begin{bmatrix} \Delta \dot{V}_{dc}^2 \\ \Delta \dot{\varphi}_v^{dc} \end{bmatrix} &= \overbrace{\begin{bmatrix} I_{pv}^o & 0 \\ C_{dc} \sqrt{V_{dc}^{2o}} & 0 \\ -k_i^{vdc} & 0 \end{bmatrix}}^{A_9} \begin{bmatrix} \Delta V_{dc}^2 \\ \Delta \varphi_v^{dc} \end{bmatrix} + \overbrace{\begin{bmatrix} 0 & 0 \\ k_i^{vdc} & 0 \end{bmatrix}}^{B_9} \begin{bmatrix} \Delta V_{dc}^{2*} \\ \Delta P_{pv} \end{bmatrix} + \overbrace{\begin{bmatrix} -3v_d^o & -3v_q^o \\ C_{dc} & C_{dc} \\ 0 & 0 \end{bmatrix}}^{C_9} \begin{bmatrix} \Delta i_d^g \\ \Delta i_q^g \end{bmatrix} \\ &+ \underbrace{\begin{bmatrix} -3i_d^o & -3i_q^o \\ C_{dc} & C_{dc} \\ 0 & 0 \end{bmatrix}}_{D_9} \begin{bmatrix} \Delta v_d^g \\ \Delta v_q^g \end{bmatrix} + \underbrace{\begin{bmatrix} \left( \frac{2\sqrt{V_{dc}^{2o}}}{C_{dc}} \right) \\ 0 \end{bmatrix}}_{E_9} [\Delta I_{pv}] \end{aligned}$$

**Equ (3.33) and Equ (3.38)** Linearized Equation of the D-Q Axes Reference Currents

$$\begin{aligned} \begin{bmatrix} \Delta i_d^* \\ \Delta i_q^* \end{bmatrix} &= \overbrace{\begin{bmatrix} \left( k_p^{vdc} + \frac{\eta I_{pv}^o}{2\sqrt{V_{dc}^{2o}}} \right) & \\ \frac{-1}{1.5v_d^o} & \frac{-1}{1.5v_d^o} \\ 0 & 0 \end{bmatrix}}^{A_{10}} \begin{bmatrix} \Delta V_{dc}^2 \\ \Delta \varphi_v^{dc} \end{bmatrix} + \overbrace{\begin{bmatrix} -k_p^{vdc} & 0 \\ 1.5v_d^o & 0 \\ 0 & 0 \end{bmatrix}}^{B_{10}} \begin{bmatrix} \Delta V_{dc}^{2*} \\ \Delta P_{pv} \end{bmatrix} + \overbrace{\begin{bmatrix} 0 \\ -2 \\ 3v_d^o \end{bmatrix}}^{C_{10}} [\Delta \varphi_v^{ac}] \\ &+ \underbrace{\begin{bmatrix} 0 & 0 \\ \frac{2k_p^{vac}}{3v_d^o} & 0 \end{bmatrix}}_{D_{10}} \begin{bmatrix} \Delta v_d^c \\ \Delta v_q^c \end{bmatrix} + \underbrace{\begin{bmatrix} 0 \\ -2k_p^{vac} \\ 3v_d^o \end{bmatrix}}_{E_{10}} [\Delta v_d^*] + \underbrace{\begin{bmatrix} \left( \frac{\eta \sqrt{V_{dc}^{2o}}}{1.5v_d^o} \right) \\ 0 \end{bmatrix}}_{F_{10}} [\Delta I_{pv}] \end{aligned}$$

**Equ (3.33)** DC-Cable Linearized Equation

$$\begin{aligned} \Delta \dot{I}_{pv} &= \overbrace{\begin{bmatrix} 1 & \\ -\frac{1}{2L_{dc} \sqrt{V_{dc}^{2o}}} & 0 \end{bmatrix}}^{A_{11}} \begin{bmatrix} \Delta V_{dc}^2 \\ \Delta \varphi_v^{dc} \end{bmatrix} + \overbrace{\begin{bmatrix} -R_{dc} & P_{pv}^o \\ L_{dc} & L_{dc} (I_{pv}^o)^2 \end{bmatrix}}^{B_{11}} [\Delta I_{pv}] \\ &+ \underbrace{\begin{bmatrix} 0 & \\ 0 & \left( \frac{1}{L_{dc} I_{pv}^o} \right) \end{bmatrix}}_{C_{11}} \begin{bmatrix} \Delta V_{dc}^{2*} \\ \Delta P_{pv} \end{bmatrix} \end{aligned}$$

Define the following zeros and identity matrices:

$$I = \begin{bmatrix} 1 & 0 \\ 0 & 1 \end{bmatrix} \quad Z = \begin{bmatrix} 0 & 0 \\ 0 & 0 \end{bmatrix} \quad Z_v = [0 \quad 0] \quad Z_v^T = \begin{bmatrix} 0 \\ 0 \end{bmatrix}$$

### A.3.3 Small-Signal State-Space Model

Define the following 14 states and five inputs in the d-q frame

$$\Delta x = [\Delta i_d^g \ \Delta i_q^g \ \Delta i_{gd}^g \ \Delta i_{gq}^g \ \Delta v_d^g \ \Delta v_q^g \ \Delta \varphi_d^i \ \Delta \varphi_q^i \ \Delta \varepsilon \ \Delta \varphi_\varepsilon^{pll} \ \varphi_v^{ac} \ \Delta V_{dc}^2 \ \Delta \varphi_v^{dc} \ \Delta I_{pv}]^T$$

$$\Delta u = [\Delta V_{dc}^{2*} \ \Delta P_{pv} \ \Delta v_d^* \ \Delta v_{gd}^g \ \Delta v_{gq}^g]^T$$

#### Approximated Model

The state-space model of the approximated system is given as follows:

$$A11 = \begin{bmatrix} A1 + B1(A4 - B4) & Z & -B1 + C1D6 + B1 + B1C4D6 + B1B4D10 \\ Z & A2 & (1/N)B2 + C2D6 \\ B3 & -(1/N)B3 & A3 + C3D6 \end{bmatrix}$$

$$A21 = \begin{bmatrix} -A5 & Z & A5D10 \\ Z & Z & B6 \end{bmatrix}$$

$$A31 = \begin{bmatrix} Z_v & Z_v & A8 \\ C9 + D9(A4 - B4) & Z & D9(I + C4D6 + B4D10) \\ Z_v & Z_v & Z_v \end{bmatrix}$$

$$A12 = \begin{bmatrix} B1 & (C1 + B1C4)(C6 + D6A7) + B1(C7 + A4B7 + A7 + B4(D10A7 - B7)) \\ Z & C2(C6 + D6A7) \\ Z & C3(C6 + D6A7) \end{bmatrix}$$

$$A22 = \begin{bmatrix} Z & -A5B7 + A5D10A7 \\ Z & A6 + B6A7 \end{bmatrix}$$

$$A32 = \begin{bmatrix} Z_v & A8A7 \\ D9 & D9(C7 + A4B7 + A7 - B4B7 + C4C6 + C4D6A7 + B4D10A7) \\ Z_v & Z_v \end{bmatrix}$$

$$A13 = \begin{bmatrix} B1B4C10 & B1B4A10 & B1B4F10 \\ Z_v^T & Z & Z_v^T \\ Z_v^T & Z & Z_v^T \end{bmatrix}$$

$$A23 = \begin{bmatrix} A5C10 & A5A10 & A5F10 \\ Z_v^T & Z & Z_v^T \end{bmatrix}$$

$$A33 = \begin{bmatrix} Z_v Z_v^T & Z_v & Z_v Z_v^T \\ D9B4C10 & A9 + D9B4A10 & E9 + D9B4F10 \\ Z_v Z_v^T & A11 & B11 \end{bmatrix}$$

$$A = \begin{bmatrix} A11 & A12 & A13 \\ A21 & A22 & A23 \\ A31 & A32 & A33 \end{bmatrix}$$

$$B = \begin{bmatrix} B1B4B10 & B1B4E10 & Z \\ Z & Z_v^T & -B2 \\ Z & Z_v^T & Z \\ A5B10 & A5E10 & Z \\ Z & Z_v^T & Z \\ Z_v & B8 & Z_v \\ B9 + D9B4B10 & D9B4E10 & Z \\ C11 & Z_v Z_v^T & Z_v \end{bmatrix}$$

### Accurate Model

The state-space model of the accurate system is given as follows:

$$A11 = \begin{bmatrix} A1 + B1(A4 - B4) & Z & -B1 + C1D6 + B1 + B1C4D6 + B1B4D10 \\ Z & A2 & (1/N)B2 + C2D6 \\ B3 & -(1/N)B3 & A3 + C3D6 \end{bmatrix}$$

$$A21 = \begin{bmatrix} -A5 & Z & A5D10 \\ Z & Z & B6 \end{bmatrix}$$

$$A31 = \begin{bmatrix} Z_v & Z_v & A8 \\ C9 + F9(A1 + B1(A4 - B4)) & Z & D9 + F9(C1D6 + B1 + B1C4D6 + B1B4D10) \\ Z_v & Z_v & Z_v \end{bmatrix}$$

$$A12 = \begin{bmatrix} B1 & (C1 + B1C4)(C6 + D6A7) + B1(C7 + A4B7 + A7 + B4(D10A7 - B7)) \\ Z & C2(C6 + D6A7) \\ Z & C3(C6 + D6A7) \end{bmatrix}$$

$$A22 = \begin{bmatrix} Z & -A5B7 + A5D10A7 \\ Z & A6 + B6A7 \end{bmatrix}$$

$$A32 = \begin{bmatrix} Z_v & A8A7 \\ F9B1 & F9(C1 + B1C4)(C6 + D6A7) + F9B1(C7 + A4B7 + A7 + B4(D10A7 - B7)) \\ Z_v & Z_v \end{bmatrix}$$

$$A13 = \begin{bmatrix} B1B4C10 & B1B4A10 & B1B4F10 \\ Z_v^T & Z & Z_v^T \\ Z_v^T & Z & Z_v^T \end{bmatrix}$$

$$A23 = \begin{bmatrix} A5C10 & A5A10 & A5F10 \\ Z_v^T & Z & Z_v^T \end{bmatrix}$$

$$A33 = \begin{bmatrix} Z_v Z_v^T & Z_v & Z_v Z_v^T \\ F9B1B4C10 & A9 + F9B1B4A10 & E9 + F9B1B4F10 \\ Z_v Z_v^T & A11 & B11 \end{bmatrix}$$

$$A = \begin{bmatrix} A11 & A12 & A13 \\ A21 & A22 & A23 \\ A31 & A32 & A33 \end{bmatrix}$$

$$B = \begin{bmatrix} B1B4B10 & B1B4E10 & Z \\ Z & Z_v^T & -B2 \\ Z & Z_v^T & Z \\ A5B10 & A5E10 & Z \\ Z & Z_v^T & Z \\ Z_v & B8 & Z_v \\ B9 + F9B1B4B10 & F9B1B4E10 & Z \\ C11 & Z_v Z_v^T & Z_v \end{bmatrix}$$

## Appendix A.4

### A.4.1 Eigenvalues and Impedance Models of the Uncompensated System

#### Eigenvalues Analysis

Apply the same Linearized Equations in A.3.3 with modification on the input vector as follows:  
**Equ (3.19a) and Equ (3.33)** DC-Link Dynamic Linearized Equation of the Accurate System

$$\begin{bmatrix} \Delta \dot{V}_{dc}^2 \\ \Delta \dot{\phi}_v^{dc} \end{bmatrix} = \overbrace{\begin{bmatrix} \frac{I_{pv}^o}{C_{dc} \sqrt{V_{dc}^{2o}}} & 0 \\ -k_i^{vdc} & 0 \end{bmatrix}}^{A_9} \begin{bmatrix} \Delta V_{dc}^2 \\ \Delta \phi_v^{dc} \end{bmatrix} + \overbrace{\begin{bmatrix} 0 & 0 \\ k_i^{vdc} & 0 \end{bmatrix}}^{B_9} \begin{bmatrix} \Delta V_{dc}^{2*} \\ \Delta r_d \end{bmatrix} + \overbrace{\begin{bmatrix} \frac{-3v_{id}^o}{C_{dc}} & \frac{-3v_{iq}^o}{C_{dc}} \\ 0 & 0 \end{bmatrix}}^{C_9} \begin{bmatrix} \Delta i_d^g \\ \Delta i_q^g \end{bmatrix} \\ + \overbrace{\begin{bmatrix} \frac{-3i_d^o}{C_{dc}} & \frac{-3i_q^o}{C_{dc}} \\ 0 & 0 \end{bmatrix}}^{D_9} \begin{bmatrix} \Delta v_{id}^g \\ \Delta v_{iq}^g \end{bmatrix} + \overbrace{\begin{bmatrix} \frac{2\sqrt{V_{dc}^{2o}}}{C_{dc}} \\ 0 \end{bmatrix}}^{E_9} [\Delta I_{pv}]$$

**Equ (3.33) and Equ (3.38)** Linearized Equation of the D-Q Axes Reference Currents

$$\begin{aligned}
\begin{bmatrix} \Delta i_d^* \\ \Delta i_q^* \end{bmatrix} &= \overbrace{\begin{bmatrix} \left( k_p^{vdc} + \frac{\eta I_{pv}^o}{2\sqrt{V_{dc}^{2o}}} \right) & \\ \frac{1.5v_d^o}{0} & \frac{-1}{1.5v_d^o} \end{bmatrix}}^{A_{10}} \begin{bmatrix} \Delta V_{dc}^2 \\ \Delta \varphi_v^{dc} \end{bmatrix} + \overbrace{\begin{bmatrix} -k_p^{vdc} & \\ 1.5v_d^o & 0 \\ 0 & 0 \end{bmatrix}}^{B_{10}} \begin{bmatrix} \Delta V_{dc}^2 \\ \Delta r_d \end{bmatrix} + \overbrace{\begin{bmatrix} 0 \\ -2 \\ 3v_d^o \end{bmatrix}}^{C_{10}} [\Delta \varphi_v^{ac}] \\
&+ \overbrace{\begin{bmatrix} 0 & 0 \\ 2k_p^{vac} & 0 \\ 3v_d^o & 0 \end{bmatrix}}^{D_{10}} \begin{bmatrix} \Delta v_d^c \\ \Delta v_q^c \end{bmatrix} + \overbrace{\begin{bmatrix} 0 \\ -2k_p^{vac} \\ 3v_d^o \end{bmatrix}}^{E_{10}} [\Delta v_d^*] + \overbrace{\begin{bmatrix} \left( \frac{\eta \sqrt{V_{dc}^{2o}}}{1.5v_d^o} \right) \\ 0 \end{bmatrix}}^{F_{10}} [\Delta I_{pv}]
\end{aligned}$$

**Equ (3.33)** DC-Cable Linearized Equation

$$\begin{aligned}
\Delta I_{pv} &= \overbrace{\begin{bmatrix} 1 \\ -\frac{1}{2L_{dc}\sqrt{V_{dc}^{2o}}} & 0 \end{bmatrix}}^{A_{11}} \begin{bmatrix} \Delta V_{dc}^2 \\ \Delta \varphi_v^{dc} \end{bmatrix} + \overbrace{\begin{bmatrix} (r_d - R_{dc}) \\ L_{dc} \end{bmatrix}}^{B_{11}} [\Delta I_{pv}] + \overbrace{\begin{bmatrix} 0 \\ \left( \frac{I_{pv}^o}{L_{dc}} \right) \end{bmatrix}}^{C_{11}} \begin{bmatrix} \Delta V_{dc}^2 \\ \Delta r_d \end{bmatrix}
\end{aligned}$$

Define the following 14 states and five inputs in the d-q frame

$$\begin{aligned}
\Delta x &= [\Delta i_d^g \ \Delta i_q^g \ \Delta i_{gd}^g \ \Delta i_{gq}^g \ \Delta v_d^g \ \Delta v_q^g \ \Delta \varphi_d^i \ \Delta \varphi_q^i \ \Delta \varepsilon \ \Delta \varphi_\varepsilon^{pll} \ \varphi_v^{ac} \ \Delta V_{dc}^2 \ \Delta \varphi_v^{dc} \ \Delta I_{pv}]^T \\
\Delta u &= [\Delta V_{dc}^2 \ \Delta r_d \ \Delta v_d^* \ \Delta v_{gd}^g \ \Delta v_{gq}^g]^T
\end{aligned}$$

The state-space model of the modified system is given as follows:

$$A_{11} = \begin{bmatrix} A1 + B1(A4 - B4) & Z & -B1 + C1D6 + B1 + B1C4D6 + B1B4D10 \\ Z & A2 & (1/N)B2 + C2D6 \\ B3 & -(1/N)B3 & A3 + C3D6 \end{bmatrix}$$

$$A_{21} = \begin{bmatrix} -A5 & Z & A5D10 \\ Z & Z & B6 \end{bmatrix}$$

$$A_{31} = \begin{bmatrix} Z_v & Z_v & A8 \\ C9 + D9(A4 - B4) & Z & D9(I + C4D6 + B4D10) \\ Z_v & Z_v & Z_v \end{bmatrix}$$

$$A_{12} = \begin{bmatrix} B1 & (C1 + B1C4)(C6 + D6A7) + B1(C7 + A4B7 + A7 + B4(D10A7 - B7)) \\ Z & C2(C6 + D6A7) \\ Z & C3(C6 + D6A7) \end{bmatrix}$$

$$A_{22} = \begin{bmatrix} Z & -A5B7 + A5D10A7 \\ Z & A6 + B6A7 \end{bmatrix}$$

$$A32 = \begin{bmatrix} Z_v & A8A7 \\ D9 & D9(C7 + A4B7 + A7 - B4B7 + C4C6 + C4D6A7 + B4D10A7) \\ Z_v & Z_v \end{bmatrix}$$

$$A13 = \begin{bmatrix} B1B4C10 & B1B4A10 & B1B4F10 \\ Z_v^T & Z & Z_v^T \\ Z_v^T & Z & Z_v^T \end{bmatrix}$$

$$A23 = \begin{bmatrix} A5C10 & A5A10 & A5F10 \\ Z_v^T & Z & Z_v^T \end{bmatrix}$$

$$A33 = \begin{bmatrix} Z_v Z_v^T & Z_v & Z_v Z_v^T \\ D9B4C10 & A9 + D9B4A10 & E9 + D9B4F10 \\ Z_v Z_v^T & A11 & B11 \end{bmatrix}$$

$$A = \begin{bmatrix} A11 & A12 & A13 \\ A21 & A22 & A23 \\ A31 & A32 & A33 \end{bmatrix}$$

### Impedance Analysis

Divide the previous state-space system that is used for the eigenvalue analysis of the uncompensated system in A.4.1 into two models.

- State-space model (1): Load Impedance ( $Z_l$ )

Apply the same Linearized Equations in A.3.3 with modification on the input vector as follows:

**Equ (3.19a) and Equ (3.33)** DC-Link Dynamic Linearized Equation of the Accurate System

$$\begin{bmatrix} \Delta \dot{V}_{dc}^2 \\ \Delta \dot{\phi}_v^{dc} \end{bmatrix} = \underbrace{\begin{bmatrix} \frac{I_{pv}^o}{C_{dc} \sqrt{V_{dc}^{2o}}} & 0 \\ C_{dc} \sqrt{V_{dc}^{2o}} & -k_i^{vdc} \end{bmatrix}}_{A_9} \begin{bmatrix} \Delta V_{dc}^2 \\ \Delta \phi_v^{dc} \end{bmatrix} + \underbrace{\begin{bmatrix} 0 & \frac{2\sqrt{V_{dc}^{2o}}}{C_{dc}} \\ k_i^{vdc} & 0 \end{bmatrix}}_{B_9} \begin{bmatrix} \Delta V_{dc}^{2*} \\ \Delta I_{pv} \end{bmatrix} + \underbrace{\begin{bmatrix} \frac{-3v_{id}^o}{C_{dc}} & \frac{-3v_{iq}^o}{C_{dc}} \\ 0 & 0 \end{bmatrix}}_{C_9} \begin{bmatrix} \Delta i_d^g \\ \Delta i_q^g \end{bmatrix} \\ + \underbrace{\begin{bmatrix} \frac{-3i_d^o}{C_{dc}} & \frac{-3i_q^o}{C_{dc}} \\ 0 & 0 \end{bmatrix}}_{D_9} \begin{bmatrix} \Delta v_{id}^g \\ \Delta v_{iq}^g \end{bmatrix}$$

**Equ (3.33) and Equ (3.38)** Linearized Equation of the D-Q Axes Reference Currents

$$\begin{aligned}
\begin{bmatrix} \Delta i_d^* \\ \Delta i_q^* \end{bmatrix} &= \begin{bmatrix} \overbrace{\left( k_p^{vdc} + \frac{\eta I_{pv}^o}{2\sqrt{V_{dc}^2{}^o}} \right)}^{A_{10}} & 0 \\ \frac{1}{1.5v_d^o} & \frac{-1}{1.5v_d^o} \\ 0 & 0 \end{bmatrix} \begin{bmatrix} \Delta V_{dc}^2 \\ \Delta \phi_v^{dc} \end{bmatrix} + \begin{bmatrix} \overbrace{\left( \frac{-k_p^{vdc}}{1.5v_d^o} \quad \frac{\eta\sqrt{V_{dc}^2{}^o}}{1.5v_d^o} \right)}^{B_{10}} \\ 0 & 0 \end{bmatrix} \begin{bmatrix} \Delta V_{dc}^2{}^* \\ \Delta i_{ext} \end{bmatrix} \\
&+ \begin{bmatrix} \overbrace{0}^{C_{10}} \\ \frac{-2}{3v_d^o} \end{bmatrix} \Delta \phi_v^{ac} + \underbrace{\begin{bmatrix} 0 & 0 \\ \frac{2k_p^{vac}}{3v_d^o} & 0 \end{bmatrix}}_{D_{10}} \begin{bmatrix} \Delta v_d^c \\ \Delta v_q^c \end{bmatrix} + \underbrace{\begin{bmatrix} 0 \\ \frac{-2k_p^{vac}}{3v_d^o} \end{bmatrix}}_{E_{10}} \Delta v_d^*
\end{aligned}$$

Define the following 13 states and 5 inputs in the d-q frame to find the transfer function

$$(TF = \frac{\Delta V_{dc}^2}{\Delta I_{pv}})$$

$$\Delta x = [\Delta i_d^g \quad \Delta i_q^g \quad \Delta i_{gd}^g \quad \Delta i_{gq}^g \quad \Delta v_d^g \quad \Delta v_q^g \quad \Delta \phi_d^i \quad \Delta \phi_q^i \quad \Delta \varepsilon \quad \Delta \phi_\varepsilon^{pll} \quad \phi_v^{ac} \quad \Delta V_{dc}^2 \quad \Delta \phi_v^{dc}]^T$$

$$\Delta u = [\Delta V_{dc}^2{}^* \quad \Delta I_{pv} \quad \Delta v_d^* \quad \Delta v_{gd}^g \quad \Delta v_{gq}^g]^T$$

$$A_{11} = \begin{bmatrix} A1 + B1(A4 - B4) & Z & -B1 + C1D6 + B1 + B1C4D6 + B1B4D10 \\ Z & A2 & (1/N)B2 + C2D6 \\ B3 & -(1/N)B3 & A3 + C3D6 \end{bmatrix}$$

$$A_{21} = \begin{bmatrix} -A5 & Z & A5D10 \\ Z & Z & B6 \end{bmatrix}$$

$$A_{31} = \begin{bmatrix} Z_v & Z_v & A8 \\ C9 + D9(A4 - B4) & Z & D9(I + C4D6 + B4D10) \end{bmatrix}$$

$$A_{12} = \begin{bmatrix} B1 & (C1 + B1C4)(C6 + D6A7) + B1(C7 + A4B7 + A7 + B4(D10A7 - B7)) \\ Z & C2(C6 + D6A7) \\ Z & C3(C6 + D6A7) \end{bmatrix}$$

$$A_{22} = \begin{bmatrix} Z & -A5B7 + A5D10A7 \\ Z & A6 + B6A7 \end{bmatrix}$$

$$A_{32} = \begin{bmatrix} Z_v & A8A7 \\ D9 & D9(C7 + A4B7 + A7 - B4B7 + C4C6 + C4D6A7 + B4D10A7) \end{bmatrix}$$

$$A_{13} = \begin{bmatrix} B1B4C10 & B1B4A10 \\ Z_v^T & Z \\ Z_v^T & Z \end{bmatrix}$$

$$A_{23} = \begin{bmatrix} A5C10 & A5A10 \\ Z_v^T & Z \end{bmatrix}$$

$$A_{33} = \begin{bmatrix} Z_v Z_v^T & Z_v \\ D9B4C10 & A9 + D9B4A10 \end{bmatrix}$$

$$A = \begin{bmatrix} A11 & A12 & A13 \\ A21 & A22 & A23 \\ A31 & A32 & A33 \end{bmatrix}$$

$$B = \begin{bmatrix} B1B4B10 & B1B4E10 & Z \\ Z & Z_v^T & -B2 \\ Z & Z_v^T & Z \\ A5B10 & A5E10 & Z \\ Z & Z_v^T & Z \\ Z_v & B8 & Z_v \\ B9 + D9B4B10 & D9B4E10 & Z \end{bmatrix}$$

Use ( $\Delta V_{dc}^2 \approx 2V_{dc}^o \Delta V_{dc}$ ), the Load Impedance of the uncompensated system is given as follows:

$$\Delta Z_l^{un} = \frac{\Delta V_{dc}}{\Delta I_{pv}} = \frac{1}{2V_{dc}^o} \overbrace{\Delta V_{dc}^2}^{TF} \Delta I_{pv}$$

- State-space model (2): Source Impedance ( $Z_s$ )

The state-space linearized equation of the dc-cable is implemented as follows:

**Equ (3.33)** DC-Cable Linearized Equation

$$[\Delta I_{pv}] = \left[ -\frac{1}{L_{dc}} \right] [\Delta V_{dc}] + \left[ \left( \frac{r_d - R_{dc}}{L_{dc}} \right) \right] [\Delta I_{pv}]$$

The Source Impedance is given as follows:

$$\Delta Z_s = \frac{\Delta V_{dc}}{\Delta I_{pv}} = (-L_{dc})s + (r_d - R_{dc})$$

#### A.4.2 Eigenvalues and Impedance Models of the Compensated System

##### Eigenvalues Analysis

Two more states are added in the compensated system, apply the same Linearized Equations in A.3.3 with modifications on the input and state vectors as follows:

**Equ (3.19a) and Equ (3.33)** DC-Link Dynamic Linearized Equation of the Accurate System

$$\begin{aligned}
\begin{bmatrix} \Delta \dot{V}_{dc}^2 \\ \Delta \dot{\phi}_v^{dc} \end{bmatrix} &= \overbrace{\begin{bmatrix} \frac{I_{pv}^o}{C_{dc} \sqrt{V_{dc}^2{}^o}} & 0 \\ -k_i^{vdc} & 0 \end{bmatrix}}^{A_9} \begin{bmatrix} \Delta V_{dc}^2 \\ \Delta \phi_v^{dc} \end{bmatrix} + \overbrace{\begin{bmatrix} 0 & 0 \\ k_i^{vdc} & 0 \end{bmatrix}}^{B_9} \begin{bmatrix} \Delta V_{dc}^{2*} \\ \Delta r_d \end{bmatrix} + \overbrace{\begin{bmatrix} -3v_{id}^o & -3v_{iq}^o \\ C_{dc} & C_{dc} \\ 0 & 0 \end{bmatrix}}^{C_9} \begin{bmatrix} \Delta i_d^g \\ \Delta i_q^g \end{bmatrix} \\
&+ \overbrace{\begin{bmatrix} -3i_d^o & -3i_q^o \\ C_{dc} & C_{dc} \\ 0 & 0 \end{bmatrix}}^{D_9} \begin{bmatrix} \Delta v_{id}^g \\ \Delta v_{iq}^g \end{bmatrix} + \overbrace{\begin{bmatrix} \frac{2\sqrt{V_{dc}^2{}^o}}{C_{dc}} \\ 0 \end{bmatrix}}^{E_9} [\Delta I_{pv}]
\end{aligned}$$

**Equ (3.38) and Equ (4.3)** Linearized Equation of the D-Q Axes Reference Currents

$$\begin{aligned}
\begin{bmatrix} \Delta i_d^* \\ \Delta i_q^* \end{bmatrix} &= \overbrace{\begin{bmatrix} \left( k_p^{vdc} + \frac{\eta I_{pv}^o}{2\sqrt{V_{dc}^2{}^o}} \right) & \\ \frac{-1}{1.5v_d^o} & \frac{-1}{1.5v_d^o} \\ 0 & 0 \end{bmatrix}}^{A_{10}} \begin{bmatrix} \Delta V_{dc}^2 \\ \Delta \phi_v^{dc} \end{bmatrix} + \overbrace{\begin{bmatrix} -k_p^{vdc} & 0 \\ 1.5v_d^o & 0 \\ 0 & 0 \end{bmatrix}}^{B_{10}} \begin{bmatrix} \Delta v_{dc}^{2*} \\ \Delta r_d \end{bmatrix} + \overbrace{\begin{bmatrix} 0 \\ -2 \\ 3v_d^o \end{bmatrix}}^{C_{10}} [\Delta \phi_v^{ac}] \\
&+ \overbrace{\begin{bmatrix} 0 & 0 \\ \frac{2k_p^{vac}}{3v_d^o} & 0 \end{bmatrix}}^{D_{10}} \begin{bmatrix} \Delta v_d^c \\ \Delta v_q^c \end{bmatrix} + \overbrace{\begin{bmatrix} 0 \\ -2k_p^{vac} \\ 3v_d^o \end{bmatrix}}^{E_{10}} [\Delta v_d^*] + \overbrace{\begin{bmatrix} \frac{\eta \sqrt{V_{dc}^2{}^o}}{1.5v_d^o} \\ 0 \end{bmatrix}}^{F_{10}} [\Delta I_{pv}] \\
&+ \overbrace{\begin{bmatrix} \alpha & 0 \\ 0 & 0 \end{bmatrix}}^{G_{10}} \begin{bmatrix} \Delta i_x \\ \Delta i_y \end{bmatrix}
\end{aligned}$$

**Equ (3.33)** DC-Cable Linearized Equation

$$\begin{aligned}
\Delta \dot{I}_{pv} &= \overbrace{\begin{bmatrix} 1 \\ -\frac{1}{2L_{dc} \sqrt{V_{dc}^2{}^o}} & 0 \end{bmatrix}}^{A_{11}} \begin{bmatrix} \Delta V_{dc}^2 \\ \Delta \phi_v^{dc} \end{bmatrix} + \overbrace{\left[ \frac{(r_d - R_{dc})}{L_{dc}} \right]}^{B_{11}} [\Delta I_{pv}] + \overbrace{\begin{bmatrix} 0 & \left( \frac{I_{pv}^o}{L_{dc}} \right) \end{bmatrix}}^{C_{11}} \begin{bmatrix} \Delta V_{dc}^{2*} \\ \Delta r_d \end{bmatrix}
\end{aligned}$$

**Equ (4.4)** Linearized Equation of the active compensator

$$\begin{bmatrix} \Delta i_x \\ \Delta i_y \end{bmatrix} = \overbrace{\begin{bmatrix} -1 & C_{dc} \\ R_{C_{dc}} C_{dc} & -\frac{1}{\tau} \\ 0 & -\frac{1}{\tau} \end{bmatrix}}^{A_{12}} \begin{bmatrix} \Delta i_x \\ \Delta i_y \end{bmatrix} + \overbrace{\begin{bmatrix} C_{dc} & 0 \\ 2\tau\sqrt{V_{dc}^2} & 1 \\ 2\tau\sqrt{V_{dc}^2} & 0 \end{bmatrix}}^{B_{12}} \begin{bmatrix} \Delta V_{dc}^2 \\ \Delta \varphi_v^{dc} \end{bmatrix}$$

Define the following 16 states and five inputs in the d-q frame

$$\Delta x = [\Delta i_d^g \ \Delta i_q^g \ \Delta i_{gd}^g \ \Delta i_{gq}^g \ \Delta v_d^g \ \Delta v_q^g \ \Delta \varphi_d^i \ \Delta \varphi_q^i \ \Delta \varepsilon \ \Delta \varphi_\varepsilon^{pll} \ \varphi_v^{ac} \ \Delta V_{dc}^2 \ \Delta \varphi_v^{dc} \ \Delta I_{pv} \ \Delta i_x \ \Delta i_y]^T$$

$$\Delta u = [\Delta V_{dc}^{2*} \ \Delta r_d \ \Delta v_d^* \ \Delta v_{gd}^g \ \Delta v_{gq}^g]^T$$

$$A_{11} = \begin{bmatrix} A1 + B1(A4 - B4) & Z & -B1 + C1D6 + B1 + B1C4D6 + B1B4D10 \\ Z & A2 & (1/N)B2 + C2D6 \\ B3 & -(1/N)B3 & A3 + C3D6 \end{bmatrix}$$

$$A_{21} = \begin{bmatrix} -A5 & Z & A5D10 \\ Z & Z & B6 \\ Z_v & Z_v & A8 \end{bmatrix}$$

$$A_{31} = \begin{bmatrix} C9 + D9(A4 - B4) & Z & D9(I + C4D6 + B4D10) \\ Z_v & Z_v & Z_v \\ Z & Z & Z \end{bmatrix}$$

$$A_{12} = \begin{bmatrix} B1 & (C1 + B1C4)(C6 + D6A7) + B1(C7 + A4B7 + A7 + B4(D10A7 - B7)) & B1B4C10 \\ Z & C2(C6 + D6A7) & Z_v^T \\ Z & C3(C6 + D6A7) & Z_v^T \end{bmatrix}$$

$$A_{22} = \begin{bmatrix} Z & -A5B7 + A5D10A7 & A5C10 \\ Z & A6 + B6A7 & Z_v^T \\ Z_v & A8A7 & Z_v Z_v^T \end{bmatrix}$$

$$A_{32} = \begin{bmatrix} D9 & D9(C7 + A4B7 + A7 + C4(C6 + D6A7) + B4(D10A7 - B7)) & D9B4C10 \\ Z_v & Z_v & Z_v Z_v^T \\ Z & Z & Z_v^T \end{bmatrix}$$

$$A_{13} = \begin{bmatrix} B1B4(A10 + G10B12) & B1B4F10 & B1B4G10A12 \\ Z & Z_v^T & Z \\ Z & Z_v^T & Z \end{bmatrix}$$

$$A_{23} = \begin{bmatrix} A5(A10 + G10B12) & A5F10 & A5G10A12 \\ Z & Z_v^T & Z \\ Z_v & Z_v Z_v^T & Z_v \end{bmatrix}$$

$$A_{33} = \begin{bmatrix} A9 + D9B4(A10 + G10B12) & E9 + D9B4F10 & D9B4G10A12 \\ A11 & B11 & Z_v \\ B12 & Z_v^T & A12 \end{bmatrix}$$

$$A = \begin{bmatrix} A11 & A12 & A13 \\ A21 & A22 & A23 \\ A31 & A32 & A33 \end{bmatrix}$$

### Impedance Analysis

Divide the previous state-space system that is used for the eigenvalue analysis of the compensated system in A.4.2 into two models.

- State-space model (1): Load Impedance ( $Z_l$ )

Apply the same Linearized Equations in A.3.3 with modifications on the state and input vectors as follows:

**Equ (3.19a) and Equ (3.33)** DC-Link Dynamic Linearized Equation of the Accurate System

$$\begin{bmatrix} \Delta \dot{V}_{dc}^2 \\ \Delta \dot{\phi}_v^{dc} \end{bmatrix} = \overbrace{\begin{bmatrix} \frac{I_{pv}^o}{C_{dc}\sqrt{V_{dc}^{2o}}} & 0 \\ C_{dc}\sqrt{V_{dc}^{2o}} & -k_i^{vdc} \end{bmatrix}}^{A_9} \begin{bmatrix} \Delta V_{dc}^2 \\ \Delta \phi_v^{dc} \end{bmatrix} + \overbrace{\begin{bmatrix} 0 & \frac{2\sqrt{V_{dc}^{2o}}}{C_{dc}} \\ k_i^{vdc} & 0 \end{bmatrix}}^{B_9} \begin{bmatrix} \Delta V_{dc}^{2*} \\ \Delta I_{pv} \end{bmatrix} + \overbrace{\begin{bmatrix} -3v_{id}^o & -3v_{iq}^o \\ C_{dc} & C_{dc} \\ 0 & 0 \end{bmatrix}}^{C_9} \begin{bmatrix} \Delta i_d^g \\ \Delta i_q^g \end{bmatrix} \\ + \underbrace{\begin{bmatrix} -3i_d^o & -3i_q^o \\ C_{dc} & C_{dc} \\ 0 & 0 \end{bmatrix}}_{D_9} \begin{bmatrix} \Delta v_{id}^g \\ \Delta v_{iq}^g \end{bmatrix}$$

**Equ (3.38) and Equ (4.3)** Linearized Equation of the D-Q Axes Reference Currents

$$\begin{bmatrix} \Delta i_d^* \\ \Delta i_q^* \end{bmatrix} = \overbrace{\begin{bmatrix} \left( k_p^{vdc} + \frac{\eta I_{pv}^o}{2\sqrt{V_{dc}^{2o}}} \right) & -1 \\ \frac{1.5v_d^o}{0} & \frac{1.5v_d^o}{0} \end{bmatrix}}^{A_{10}} \begin{bmatrix} \Delta V_{dc}^2 \\ \Delta \phi_v^{dc} \end{bmatrix} + \overbrace{\begin{bmatrix} -k_p^{vdc} & \eta\sqrt{V_{dc}^{2o}} \\ \frac{1.5v_d^o}{0} & \frac{1.5v_d^o}{0} \end{bmatrix}}^{B_{10}} \begin{bmatrix} \Delta V_{dc}^{2*} \\ \Delta I_{pv} \end{bmatrix} \\ + \overbrace{\begin{bmatrix} 0 \\ -2 \\ \frac{0}{3v_d^o} \end{bmatrix}}^{C_{10}} \Delta \phi_v^{ac} + \underbrace{\begin{bmatrix} 0 & 0 \\ \frac{2k_p^{vac}}{3v_d^o} & 0 \end{bmatrix}}_{D_{10}} \begin{bmatrix} \Delta v_d^c \\ \Delta v_q^c \end{bmatrix} + \underbrace{\begin{bmatrix} 0 \\ -2k_p^{vac} \\ \frac{0}{3v_d^o} \end{bmatrix}}_{E_{10}} \Delta v_d^* + \underbrace{\begin{bmatrix} \alpha & 0 \\ 0 & 0 \end{bmatrix}}_{F_{10}} \begin{bmatrix} \Delta i_x \\ \Delta i_y \end{bmatrix}$$

**Equ (4.4)** Linearized Equation of the active compensator

$$\begin{bmatrix} \Delta i_x \\ \Delta i_y \end{bmatrix} = \overbrace{\begin{bmatrix} 1 & -C_{dc} \\ -R_{C_{dc}} C_{dc} & \tau \\ 0 & -\frac{1}{\tau} \end{bmatrix}}^{A_{11}} \begin{bmatrix} \Delta i_x \\ \Delta i_y \end{bmatrix} + \overbrace{\begin{bmatrix} C_{dc} & 0 \\ 2\tau\sqrt{V_{dc}^2} & 0 \\ 1 & 0 \\ 2\tau\sqrt{V_{dc}^2} & 0 \end{bmatrix}}^{B_{11}} \begin{bmatrix} \Delta V_{dc}^2 \\ \Delta \phi_v^{dc} \end{bmatrix}$$

Define the following 15 states and 5 inputs in the d-q frame to find the transfer function

$$(TF = \frac{\Delta V_{dc}^2}{\Delta I_{pv}})$$

$$\Delta x = [\Delta i_d^g \ \Delta i_q^g \ \Delta i_{gd}^g \ \Delta i_{gq}^g \ \Delta v_d^g \ \Delta v_q^g \ \Delta \phi_d^i \ \Delta \phi_q^i \ \Delta \varepsilon \ \Delta \phi_\varepsilon^{pll} \ \phi_v^{ac} \ \Delta V_{dc}^2 \ \Delta \phi_v^{dc} \ \Delta i_x \ \Delta i_y]^T$$

$$\Delta u = [\Delta V_{dc}^2 \ \Delta I_{pv} \ \Delta v_d^* \ \Delta v_{gd}^g \ \Delta v_{gq}^g]^T$$

$$A_{11} = \begin{bmatrix} A1 + B1(A4 - B4) & Z & -B1 + C1D6 + B1 + B1C4D6 + B1B4D10 \\ Z & A2 & (1/N)B2 + C2D6 \\ B3 & -(1/N)B3 & A3 + C3D6 \end{bmatrix}$$

$$A_{21} = \begin{bmatrix} -A5 & Z & A5D10 \\ Z & Z & B6 \\ Z_v & Z_v & A8 \end{bmatrix}$$

$$A_{31} = \begin{bmatrix} C9 + D9(A4 - B4) & Z & D9(I + C4D6 + B4D10) \\ Z & Z & Z \end{bmatrix}$$

$$A_{12} = \begin{bmatrix} B1 & (C1 + B1C4)(C6 + D6A7) + B1(C7 + A4B7 + A7 + B4(D10A7 - B7)) & B1B4C10 \\ Z & C2(C6 + D6A7) & Z_v^T \\ Z & C3(C6 + D6A7) & Z_v^T \end{bmatrix}$$

$$A_{22} = \begin{bmatrix} Z & -A5B7 + A5D10A7 & A5C10 \\ Z & A6 + B6A7 & Z_v^T \\ Z_v & A8A7 & Z_v Z_v^T \end{bmatrix}$$

$$A_{32} = \begin{bmatrix} D9 & D9(C7 + A4B7 + A7 + C4(C6 + D6A7) + B4(D10A7 - B7)) & D9B4C10 \\ Z & Z & Z_v^T \end{bmatrix}$$

$$A_{13} = \begin{bmatrix} B1B4(A10 + F10B11) & B1B4F10A11 \\ Z & Z \\ Z & Z \end{bmatrix}$$

$$A_{23} = \begin{bmatrix} A5(A10 + F10B11) & A5F10A11 \\ Z & Z \\ Z_v & Z_v \end{bmatrix}$$

$$A_{33} = \begin{bmatrix} A9 + D9B4(A10 + F10B11) & D9B4F10A11 \\ B11 & A11 \end{bmatrix}$$

$$A = \begin{bmatrix} A11 & A12 & A13 \\ A21 & A22 & A23 \\ A31 & A32 & A33 \end{bmatrix}$$

$$B = \begin{bmatrix} B1B4B10 & B1B4E10 & Z \\ Z & Z_v^T & -B2 \\ Z & Z_v^T & Z \\ A5B10 & A5E10 & Z \\ Z & Z_v^T & Z \\ Z_v & B8 & Z_v \\ B9 + D9B4B10 & D9B4E10 & Z \\ Z & Z_v^T & Z \end{bmatrix}$$

Use ( $\Delta V_{dc}^2 \approx 2V_{dc}^o \Delta V_{dc}$ ), the Load Impedance of the compensated system is given as follows:

$$\Delta Z_l^{comp} = \frac{\Delta V_{dc}}{\Delta I_{pv}} = \frac{1}{2V_{dc}^o} \overbrace{\Delta V_{dc}^2}^{TF} \Delta I_{pv}$$

- State-space model (2): Source Impedance ( $Z_s$ )

The state-space linearized equation of the dc-cable is implemented as follows:

**Equ (3.33)** DC-Cable Linearized Equation

$$[\Delta I_{pv}] = \left[ -\frac{1}{L_{dc}} \right] [\Delta V_{dc}] + \left[ \left( \frac{r_d - R_{dc}}{L_{dc}} \right) \right] [\Delta I_{pv}]$$

The Source Impedance is given as follows:

$$\Delta Z_s = \frac{\Delta V_{dc}}{\Delta I_{pv}} = (-L_{dc})s + (r_d - R_{dc})$$